ANL-07/18

Argonne NATIONAL LABORATORY

Radioactive Isotope Production for Medical Applications Using Kharkov Electron Driven Subcritical Assembly Facility

Nuclear Engineering Division

About Argonne National Laboratory

Argonne is a U.S. Department of Energy laboratory managed by UChicago Argonne, LLC under contract DE-AC02-06CH11357. The Laboratory's main facility is outside Chicago, at 9700 South Cass Avenue, Argonne, Illinois 60439. For information about Argonne, see www.anl.gov.

Availability of This Report

This report is available, at no cost, at http://www.osti.gov/bridge. It is also available on paper to the U.S. Department of Energy and its contractors, for a processing fee, from:

U.S. Department of Energy
Office of Scientific and Technical Information
P.O. Box 62
Oak Ridge, TN 37831-0062
phone (865) 576-8401
fax (865) 576-5728
reports@adonis.osti.gov

ANL-07/18

Radioactive Isotope Production for Medical Applications Using Kharkov Electron Driven Subcritical Assembly Facility

by
A. Talamo and Y. Gohar
Nuclear Engineering Division, Argonne National Laboratory

April 2007

work sponsored by the
Office of Global Nuclear Material Threat Reduction
U.S. Department of Energy
Under Contract W-31-109-Eng-38

Radioactive Isotope Production for Medical Applications Using Kharkov Electron Driven Subcritical Assembly Facility

Table of Contents

Page

Abstract 1

I. Introduction 2

II. KHARKOV Facility Description 2

III. Applications of Radioactive Isotopes in Medicine 3

IV. Radioactive Medical Isotopes Production 4

V. Specific Activities of Radioactive Isotopes Without Self Shielding 5

VI. Specific Activities of Radioactive Isotopes With Self-Shielding 9

VII. Sample Size Analyses 10

VIII. Conclusions 11

REFERENCES 12

Radioactive Isotope Production for Medical Applications Using Kharkov Electron Driven Subcritical Assembly Facility

List of Figures

Figure No. Page

Figure 1. ^{235}U Photo-fission and Photo-neutron Production Cross Sections (Handbook on Photonuclear Data for Applications: Cross Sections and Spectra, IAEA, March 2000) 22

Figure 2. ^{238}U Photo-fission and Photo-neutron Production Cross Sections (Handbook on Photonuclear Data for Applications: Cross Sections and Spectra, IAEA, March 2000) 22

Figure 3. Horizontal section of the subcritical assembly, light blue=graphite, yellow=water, green=natural uranium, purple=aluminum, pink=enriched uranium, white=vacuum 23

Figure 4. Vertical section the subcritical assembly, light blue=graphite, yellow=water, green=natural uranium, purple=aluminum, pink=enriched uranium, white=vacuum 23

Figure 5. Target vertical section, light blue=graphite, yellow=water, green=natural uranium, purple=aluminum, pink=enriched uranium, white=vacuum 24

Figure 6. Target and fuel zone horizontal section, light blue=graphite, yellow=water, green=natural uranium, purple=aluminum, pink=enriched uranium, white=vacuum 24

Figure 7. Fuel horizontal section, Light blue=graphite, yellow=water, green=natural uranium, purple=aluminum, pink=enriched uranium, white=vacuum 25

Figure 8. Fuel vertical section, top fuel handling, light blue=graphite, yellow=water, green=natural uranium, purple=aluminum, pink=enriched uranium, white=vacuum 25

Figure 9. Fuel vertical section, bottom fuel handling, light blue=graphite, yellow=water, green=natural uranium, purple=aluminum, pink=enriched uranium, white=vacuum 26

Figure 10. Graphite reflector horizontal cross section, light blue=graphite, yellow=water, green=natural uranium, purple=aluminum, pink=enriched uranium, white=vacuum 26
Figure 11. Horizontal section of the target water channels between 0 and 33.0355 cm, light blue=graphite, yellow=water, green=natural uranium, purple=aluminum, pink=enriched uranium, white=vacuum 27
Figure 12. Horizontal section of the target water channels between 33.0355 and 44.1595 cm, light blue=graphite, yellow=water, green=natural uranium, purple=aluminum, pink=enriched uranium, white=vacuum 27
Figure 13. Horizontal section of the water target channels between 44.1595 and 50 cm. light blue=graphite, yellow=water, green=natural uranium, purple=aluminum, pink=enriched uranium, white=vacuum 28
Figure 14. Horizontal cross section of the water target channels between 50 and 68.005 cm, light blue=graphite; yellow=water; green=natural uranium; purple=aluminum; pink=enriched uranium; white=vacuum 28
Figure 15. Horizontal cross section of the water target channels between 68.005 and 68.405 cm, Light blue=graphite, yellow=water, green=natural uranium, purple=aluminum, pink=enriched uranium, white=vacuum 29
Figure 16. Horizontal cross section of the water target channels between 68.405 and 79.795 cm (target uranium disk), Light blue=graphite, yellow=water, green=natural uranium, purple=aluminum, pink=enriched uranium, white=vacuum 29
Figure 17. Horizontal section of the water target channels between 68.405 and 79.795 cm (target water layer), Light blue=graphite; yellow=water; green=natural uranium; purple=aluminum; pink=enriched uranium; white=vacuum 30
Figure 18. Horizontal cross section of the water target channels between 79.795 and 79.995 cm (target zone changes), light blue=graphite, yellow=water, green=natural uranium, purple=aluminum, pink=enriched uranium, white=vacuum 30

Figure 19. Horizontal cross section of the water target channels between 79.995 and 100 cm, light blue=graphite, yellow=water, green=natural uranium, purple=aluminum, pink=enriched uranium, white=vacuum 31
Figure 20. Horizontal cross section of the water target channels between 100 cm and 105.3637 cm, light blue=graphite, yellow=water, green=natural uranium, purple=aluminum, pink=enriched uranium, white=vacuum 31
Figure 21. Horizontal cross section of the water target channels between 105.3637 and 109.5355 cm, light blue=graphite, yellow=water, green=natural uranium, purple=aluminum, pink=enriched uranium, white=vacuum 32
Figure 22. Horizontal cross section of the water target channels between 109.5355 and 150 cm, light blue=graphite, yellow=water, green=natural uranium, purple=aluminum, pink=enriched uranium, white=vacuum 32
Figure 23. Irradiation locations, red circles, for the medical isotope production, light blue=graphite, yellow=water, green=natural uranium, purple=aluminum, pink=enriched uranium, white=vacuum 33
Figure 24. Vertical cross section at x=3.8 cm showing the irradiation locations next to the target, red color, light blue=graphite, yellow=water, green=natural uranium, purple=aluminum, pink=enriched uranium, white=vacuum 33
Figure 25. Vertical cross section zoom in at x=3.8 cm showing the irradiation locations next to the target, red color, light blue=graphite, yellow=water, green=natural uranium, purple=aluminum, pink=enriched uranium, white=vacuum 34
Figure 26. Vertical cross section at y=2.19 cm showing the irradiation locations used for the self shielding calculations of the medical isotope production next to the target, red color, light blue=graphite, yellow=water, green=natural uranium, purple=aluminum, pink=enriched uranium, white=vacuum 34
Figure 27. (n,γ) macroscopic cross section of the parent nuclides with σ_γ>10 b in the thermal energy range using natural elemental composition, ^{6}Li reaction is (n,t), ^{235}U fission reaction used 20% abundance, and ^{59}Co and ^{187}Re reactions are also given 35

Figure 28. (n,γ) macroscopic cross section of the parent nuclides with $\sigma_{\gamma} \in$ [1-10] b in the thermal energy range using natural elemental composition, the capture cross section of ^{176}Lu is multiplied by the ^{177m}Lu fission yield 35
Figure 29. (n,γ) macroscopic cross section of the parent nuclides with σ_{γ}<1 b in the thermal energy range using natural elemental composition, (n,p) reaction is given for ^{67}Zn, ^{98}Mo, and ^{128}Te reactions are also given 36
Figure 30. (n,γ) macroscopic cross section of the parent nuclides with σ_{γ}>10 b in the fast energy range using natural elemental composition, ^{235}U fission reaction used 20% abundance 36
Figure 31. (n,γ) macroscopic cross section of the parent nuclides with $\sigma_{\gamma} \in$ [1-10] b in the fast energy range using natural elemental composition, the capture cross section of ^{176}Lu is multiplied by the ^{177m}Lu fission yield 37
Figure 32. (n,γ) macroscopic cross section of the parent isotopes with σ_{γ}<1 b in the fast energy range using natural elemental composition 37
Figure 33. (n,γ) microscopic cross section of the radioactive parent isotopes in the thermal energy range 38
Figure 34. (n,γ) microscopic cross section of the parent isotopes that do not exist in nature 38
Figure 35. Macroscopic partial neutron cross section of the parent nuclides using natural elemental composition, cross section of ^{99}Tc is microscopic [b] 39
Figure 36. Macroscopic photonuclear cross section of the parent nuclides using natural elemental composition 39
Figure 37. Neutron spectrum in the four locations 40
Figure 38. Photon spectrum in the first location 40
Figure 39. ^{111}Ag activity as a function of the irradiation time 41
Figure 40. ^{82}Br activity as a function of the irradiation time 41
Figure 41. ^{58}Co activity as a function of the irradiation time 42
Figure 42. ^{58}Co activity as a function of the irradiation time 42
Figure 43. ^{60}Co activity as a function of the irradiation time 43
Figure 44. ^{51}Cr activity as a function of the irradiation time 43
Figure 45. ^{64}Cu activity as a function of the irradiation time 44

Figure 46. ^{67}Cu activity as a function of the irradiation time 44
Figure 47. ^{165}Dy activity as a function of the irradiation time 45
Figure 48. ^{59}Fe activity as a function of the irradiation time 45
Figure 49. ^{159}Gd activity as a function of the irradiation time 46
Figure 50. ^{166}Ho activity as a function of the irradiation time 46
Figure 51. ^{125}I activity a as function of the irradiation time 47
Figure 52. ^{192}Ir activity as a function of the irradiation time 47
Figure 53. ^{194}Ir activity as a function of the irradiation time 48
Figure 54. ^{42}K activity as a function of the irradiation time 48
Figure 55. ^{177m}Lu activity as a function of the irradiation time 49
Figure 56. ^{99}Mo activity as a function of the irradiation time 49
Figure 57. ^{24}Na activity as a function of the irradiation time 50
Figure 58. ^{32}P activity as a function of the irradiation time 50
Figure 59. ^{32}P activity as a function of the irradiation time 51
Figure 60. ^{33}P activity as a function of the irradiation time 51
Figure 61. ^{103}Pd activity as a function of the irradiation time 52
Figure 62. ^{103}Pd activity as a function of the irradiation time 52
Figure 63. ^{186}Re activity as a function of the irradiation time 53
Figure 64. ^{188}Re activity as a function of the irradiation time 53
Figure 65. ^{35}S activity as a function of the irradiation time 54
Figure 66. ^{47}Sc activity as a function of the irradiation time 54
Figure 67. ^{153}Sm activity as a function of the irradiation time 55
Figure 68. ^{99m}Tc activity as a function of the irradiation time 55
Figure 69. ^{188}W activity as a function of the irradiation time 56
Figure 70. ^{133}Xe activity as a function of the irradiation time 56
Figure 71. ^{133}Xe activity as a function of the irradiation time 57
Figure 72. ^{133}Xe activity as a function of the irradiation time 57
Figure 73. ^{90}Y activity as a function of the irradiation time 58
Figure 74. ^{111}Ag activity as a function of the irradiation time 58
Figure 75. ^{77}As activity as a function of the irradiation time 59
Figure 76. ^{137}Cs activity as a function of the irradiation time 59

Figure 77. ^{129}I activity as a function of the irradiation time 60
Figure 78. ^{131}I activity as a function of the irradiation time 60
Figure 79. ^{99}Mo activity as a function of the irradiation time 61
Figure 80. ^{89}Sr activity as a function of the irradiation time 61
Figure 81. ^{90}Sr activity as a function of the irradiation time 62
Figure 82. ^{99m}Tc activity as a function of the irradiation time 62
Figure 83. ^{133}Xe activity as a function of the irradiation time 63
Figure 84. ^{74}As activity as a function of the irradiation time 63
Figure 85. ^{139}Cs activity as a function of the irradiation time 64
Figure 86. ^{57}Co activity as a function of the irradiation time 64
Figure 87. ^{64}Cu activity as a function of the irradiation time 65
Figure 88. ^{55}Fe activity as a function of the irradiation time 65
Figure 89. ^{99}Mo activity as a function of the irradiation time 66
Figure 90. ^{33}P activity as a function of the irradiation time 66
Figure 91. ^{88}Y activity as a function of the irradiation time 67
Figure 92. ^{89}Zr activity as a function of the irradiation time 67
Figure 93. ^{60}Co activity as a function of the irradiation time without and with self shielding, left and right subplots, respectively; ^{59}Co macroscopic capture cross section; ^{60}Co represents 100% of the parent material 68
Figure 94. ^{64}Cu activity as a function of the irradiation time without and with self shielding, left and right subplots, respectively; ^{63}Cu macroscopic capture cross section; ^{63}Cu and ^{65}Cu represent 69.17 and 30.83% of the parent material, respectively 68
Figure 95. ^{166}Ho activity as a function of the irradiation time without and with self shielding, left and right subplots, respectively; ^{165}Ho macroscopic capture cross section; ^{165}Ho represents 100% of the parent material 69
Figure 96. ^{192}Ir activity as a function of the irradiation time without and with self shielding, left and right subplots, respectively; ^{191}Ir macroscopic capture cross section; ^{191}Ir and ^{193}Ir represent 37.3 and 62.7% of the parent material, respectively 69

Figure 97. ^{194}Ir activity as a function of the irradiation time without and with self shielding, left and right subplots, respectively; ^{193}Ir macroscopic capture cross section; ^{191}Ir and ^{193}Ir represent 37.3 and 62.7% of the parent material, respectively 70
Figure 98. ^{177m}Lu activity as a function of the irradiation time without and with self shielding, left and right subplots, respectively; ^{175}Lu macroscopic capture cross section; ^{175}Lu represents 97.41% of the parent material 70
Figure 99. ^{186}Re activity as a function of the irradiation time without and with self shielding, left and right subplots, respectively; ^{185}Re macroscopic capture cross section; ^{185}Re and ^{187}Re represent 37.4 and 62.6% of the parent material, respectively 71
Figure 100. ^{188}Re activity as a function of the irradiation time without and with self shielding, left and right subplots, respectively; ^{187}Re macroscopic capture cross section; ^{185}Re and ^{187}Re represent 37.4 and 62.6% of the parent material, respectively 71
Figure 101. ^{153}Sm activity as a function of the irradiation time without and with self shielding, left and right subplots, respectively; ^{149}Sm and ^{152}Sm macroscopic capture cross section; ^{149}Sm and ^{152}Sm represent 21.4 and 42% of the parent material, respectively 72
Figure 102. ^{188}W activity as a function of the irradiation time without and with self shielding, left and right subplots, respectively; ^{187}W macroscopic capture cross section; ^{186}W represents 28.6% of the parent material 72
Figure 103. ^{59}Co capture rate as function of the sample height 73
Figure 104. ^{63}Cu capture rate as a function of the sample height 74
Figure 105. ^{165}Ho capture rate as a function of the sample height 75
Figure 106. ^{191}Ir capture rate as a function of the sample height 76
Figure 107. ^{193}Ir capture rate as a function of the sample height 77
Figure 108. ^{175}Lu capture rate as a function of the sample height 78
Figure 109. ^{185}Re capture rate as a function of the sample height 79
Figure 110. ^{187}Re capture rate as a function of the sample height 80
Figure 111. ^{152}Sm capture rate as a function of the sample height 81

Figure 112. ^{186}W capture rate as a function of the sample height 82
Figure 113. ^{59}Co capture rate as a function of the sample radius 83
Figure 114. ^{63}Cu capture rate as a function of the sample radius 84
Figure 115. ^{165}Ho capture rate as a function of the sample radius 85
Figure 116. ^{191}Ir capture rate as a function of the sample radius 86
Figure 117. ^{193}Ir capture rate as a function of the sample radius 87
Figure 118. ^{175}Lu capture rate as a function of the sample radius 88
Figure 119. ^{185}Re capture rate as a function of the sample radius 89
Figure 120. ^{187}Re capture rate as a function of the sample radius 90
Figure 121. ^{152}Sm capture rate as a function of the sample radius 91
Figure 122. ^{186}W capture rate as a function of the sample radius 92

Radioactive Isotope Production for Medical Applications Using Kharkov Electron Driven Subcritical Assembly Facility

List of Tables

Table No. Page

Table I. Geometrical data of the Kharkov electron driven subcritical facility 13
Table II. Material composition of the Kharkov electron driven subcritical facility..... 14
Table III. Medical isotopes decay modes and their applications 14
Table IV. Medical Isotopes produced by neutron and photonuclear reactions 16
Table V. Best location of the capsules..... 20

Radioactive Isotope Production for Medical Applications Using Kharkov Electron Driven Subcritical Assembly Facility

Abstract

Kharkov Institute of Physics and Technology (KIPT) of Ukraine has a plan to construct an accelerator driven subcritical assembly. The main functions of the sub-critical assembly are the medical isotope production, neutron thereby, and the support of the Ukraine nuclear industry. Reactor physics experiments and material research will be carried out using the capabilities of this facility. The United States of America and Ukraine have started collaboration activity for developing a conceptual design for this facility with low enrichment uranium (LEU) fuel. Different conceptual designs are being developed based on the facility mission and the engineering requirements including nuclear physics, neutronics, heat transfer, thermal hydraulics, structure, and material issues. Different fuel designs with LEU and reflector materials are considered in the design process. Safety, reliability, and environmental considerations are included in the facility conceptual design. The facility is configured to accommodate future design improvements and upgrades.

This report is a part of the Argonne National Laboratory Activity within this collaboration for developing and characterizing the subcritical assembly conceptual design. In this study, the medical isotope production function of the Kharkov facility is defined. First, a review was carried out to identify the medical isotopes and its medical use. Then a preliminary assessment was performed without including the self-shielding effect of the irradiated samples. Finally, more detailed investigation was carried out including the self-shielding effect, which defined the sample size and irradiation location for producing each medical isotope. In the first part, the reaction rates were calculated as the multiplication of the cross section with the unperturbed neutron flux of the facility. Over fifty isotopes were considered and all transmutation channels are used including (n,γ), (n,2n), (n,p), and (γ,n). In the second part, the parent isotopes with high reaction rate were explicitly modeled in the calculations. For the nuclides with a very high capture microscopic cross section, such as iridium, rhenium, and samarium, their specific activities are reduced by a factor of 30 when the self-shielding effect is included. Four irradiation locations were considered in the analyses to maximize the medical isotope production rate. The results show the self-shield effect reduces the specific activity values and changes the irradiation location for obtaining the maximum possible specific activity. The axial and radial distributions of the specific activity were used to define the irradiation sample size for producing each isotope.

Radioactive Isotope Production for Medical Applications Using Kharkov Electron Driven Subcritical Assembly Facility

I. Introduction

Argonne National Laboratory (ANL) of the United States of America and the National Science Center "Kharkov Institute of Physics and Technology" (KIPT) of Ukraine have been collaborating for developing a conceptual design of an electron driven subcritical assembly facility. The facility capability for producing radioactive medical isotopes has been evaluated in this study. The facility consists of an electron driven subcritical system with water coolant, graphite reflector, and low enriched uranium fuel.[1-3] The electron beam power is 100 kW and the electron energy is 200 MeV. The electrons interact with the natural uranium target and generate high energy photons known as Bremsstrahlung radiation.[4] The generated photons have a continuous energy spectrum. These high energy photons interact with the uranium target and some interactions generate neutrons through (γ,xn) and (γ,f) reactions.[5] The photonuclear cross-sections are small and the maximum values are around one barn. Furthermore, photonuclear reactions peaks in the energy range of 5 to 20 MeV and the giant resonance energy is at about 15 MeV as shown in Figures 1 and 2 for U-235 and U-238 isotopes, respectively. The photonuclear cross sections rapidly drop above 25 MeV.[6-8]

In the present report, the utilization of the Kharkov electron driven facility for producing medical isotopes is investigated. The medical isotopes are radioactive isotopes that are used for diagnostic and therapeutic purposes. The field of nuclear medicine is continuously expanding; one of every three hospitalized United States patients undergoes a nuclear medicine procedure. In 1990, about 180000 patients were treated by radiation therapies in the United States.[9] The use of electron driven facilities for producing medical isotopes reduces the production cost compared to the use of proton driven facilities or nuclear fission reactors. The electron mass is 1836 times lighter than proton and therefore it is easier to accelerate. In addition, the electron accelerator driven facility volume is extremely small relative to proton accelerator facilities or nuclear fission reactors. However, some medical isotopes require an incident proton reaction for their production,[10] see table 4-1 of reference 9.

II. KHARKOV Facility Description

The conceptual design of the Kharkov electron driven subcritical assembly facility has been carried out and optimized to maximize the neutron flux for the available electron beam power. The subcritical assembly utilizes low enriched uranium (LEU) fuel, which satisfies the IAEA recommendations for civilian use of nuclear technology. The U-235 enrichment is less than 20%. The facility has been simulated and analyzed using detailed three dimensional MCNPX[11] models. The plotting capability of the MCNPX computer code has been used to illustrate the subcritical assembly geometrical

details. Figures 3 and 4 show the horizontal and vertical cross sections of the subcritical assembly, respectively. The facility has a cylindrical geometry that can accommodate a subcritical assembly with a height and radius up to 70 and 80 cm, respectively. The current subcritical assembly has a carbon reflector and its height is 61.2 cm to match the current fuel design. The electron beam tube axis coincides with the subcritical assembly axis and its radius is 3.8 cm. The target is integrated with the beam tube and its height is 12 cm. Figures 5 and 6 show the target details. The target assembly consists of 11 natural uranium disks, which alternate with the water coolant layers. The current arrangement results in a maximum disk surface temperature of 80 ^{o}C when the average coolant velocity and inlet coolant pressure are 7 m/s and 4 bar, respectively. The fuel material is uranium oxide, with ~20% enrichment, mixed with aluminum. The fuel geometry consists of two concentric cylindrical shells inside a hexagonal shell and all shells have aluminum clad, as shown in figure 7. The top and bottom sections of the fuel assembly and the structure support sections have been homogenized in the model as cylinders that preserve the volume fractions of the real geometry as shown in Figures 8 and 9. Figure 10 shows a horizontal cross section of the hexagonal graphite blocks that acts as reflector around the fuel zone. In order to illustrate the geometrical details of the target zone, several horizontal cross sections are shown in Figures 11-22 at various heights. The target water coolant enters from the top through two semi-hexagonal channels as shown in Figure 22, flows between the uranium disks as shown in Figure 5, and leaves upward through another two semi-hexagonal channels as shown in Figure 22. Three inlet and three outlet semi-hexagonal coolant channels are under consideration to reduce the thermal stress in the uranium target disks. Table I and II report the geometrical details and material compositions of the subcritical assembly, respectively.

III. Applications of Radioactive Isotopes in Medicine

Medical isotopes are radioactive isotopes that are used for diagnostic and therapeutic applications in nuclear medicine. The decay mode of radioactive isotopes may be $\alpha, \beta, \varepsilon$ (electron capture), γ, or ι (iota, isomeric transition). The utilization of radioactive isotopes for medicine purposes is classified into three categories: diagnosis, radiotherapy and biochemical analyses.[9,12,13] In diagnosis analyses, the short-lived isotopes are linked to chemical compounds that are administrated to the patients by injection, inhalation, or ingestion to obtain a gamma ray emission. The radiation can be generated by either a direct γ decay mode or an indirect γ that comes from positron annihilation with an orbital electron generating two gamma rays propagating in opposite directions. The average dose for the patient is ~4.6 mSv while the natural background radiation level is ~2.4 mSv/y. In some areas of the world, background levels can reach as high as 150 mSv/y. A gamma or positron emission tomography (PET) camera using scintillation material interpolates the radiation source points and builds up an image of the patient organ characterizing its functionality. New software techniques construct three dimensional images from two dimensional images and provide diagnosis. ^{99m}Tc is used in about 80% of the nuclear medicine diagnosis procedures because of its ideal characteristics:

- Its half life is six hours, which is long enough to examine metabolic processes and short enough to minimize radiation dose to the patient,
- The emitted gamma ray energy is 140 keV, which escapes easily the human body for reaching the counting camera,
- It has versatile chemistry.

Other utilizations are the monitoring of the chemical compounds as diffused in the body and absorbed by various organs. The radioactive isotopes are attached to the pharmaceutical substance and their activity is counted before the substance is administered to the patient. After the administration, recounting the activity permits the examination of the blood flow in the brain or other organs such as liver, lungs, heart, and kidneys. The functionality of the different organs can be assessed after the radioactive isotopes are expelled from the body by the normal biological processes.

In therapy applications, the gamma or beta emitter is located near or inserted inside the tumor mass with the aim of destroying the over-multiplying cells. ^{60}Co was formerly used for external radiotherapy. Nowadays, brachytherapy (short-range) procedures have the benefit of giving a less overall radiation to the body. The most common radioisotopes utilized for radiotherapy are ^{131}I for thyroid cancer, ^{192}Ir for head and breast tumors, ^{89}Sr, ^{153}Sm and ^{186}Re for the relief of cancer induced pain, ^{32}S for the excess of red blood cells produced by the bone marrow (Polycythemia vera), and ^{90}Y for the non-Hodgkin's lymphoma. Iridium is produced in a wire form and the wire is introduced to the patient through a catheter that is removed after treatment.

In biochemical analysis applications, the radioisotopes are used to label molecules or biological samples in vitro, since it is very easy to detect the presence of some radioactive nuclide even if it exists in a very low concentration. The human genoma project took advantage of this kind of techniques.

Table III lists the major radioactive isotopes utilized in nuclear medicine[9,12,13] with their decay mode and their applications. The transmutation chains for producing the medicine isotopes of table III are summarized in Table IV including the decay half live of the daughters and the abundance, the cross section, and cumulative fission yield of the parents. In the present studies, we analyzed the possibility to produce ^{166}Ho, ^{194}Ir and ^{188}Re from the natural composition material rather than from ^{166}Dy, ^{194}Os and ^{188}W, respectively, as suggested in reference 9.

IV. Radioactive Medical Isotopes Production

A compilation of the medical isotopes and their characteristics is given in Table IV. The Kharkov electron driven subcritical facility is employed in the analyses for the production of these medical isotopes through different reactions as indicated by the color associated with each transmutation type in Table IV. The isotopes with a red color background have not been considered in this study because their macroscopic cross

section values are very small or unavailable. In all the analyses, natural materials have been used as parent materials. Four irradiation locations in the subcritical assembly have been considered, as shown in Figures 23-26. The first is close to the target, the second is at the center of an inner fuel assembly next to the target, the third is at the center of an outer fuel assembly, and the fourth is at the center of a reflector carbon block next to a fuel element. In order to reduce the standard deviation of the MCNPX analysis, the reaction rates in each of the four locations have been sampled in a symmetric pair of cylindrical volumes, as illustrated in Figures 23. In the first analysis, the neutron flux has been averaged over cylindrical volumes with a radius of 0.3 cm and a height of 30 cm. The midplane of the irradiation volumes lies at the center of the fuel active length. In the first analysis, the self shielding effect inside the irradiation volumes has not been considered. The average flux in the four locations has been used to calculate more than fifty different reaction rates by the tally multiplier option of MCNPX. This analysis aimed at selecting which isotopes can be easily produced in the facility and also the optimal location for its production. The second analysis focused on the strong absorber parents (Co, Cu, Ho, Ir, Lu, Re, Sm and W) since the self-shielding effect reduces their reaction rate and it also changes the relative performance of the four irradiation locations. In the second analysis, the sample materials were modeled inside the irradiation volumes and the sample height has been reduced to 5 cm. The analyses took advantage of the multi-node capability of MCNPX with MPI software and of the ENDF/B nuclear data library.

V. Specific Activities of Radioactive Isotopes Without Self Shielding

The macroscopic capture cross-section of the parent nuclides in the thermal energy region are shown in Figures 27-29. The parent nuclides are grouped in three ranges in Figures 27-29 according to their microscopic capture cross section values, > 10 b, in the range from 1 to 10 b, and < 1 b, respectively. Similar data are shown in Figure 30-32 for the fast energy range, where the macroscopic cross section values are much smaller. For the parents that do not naturally exist, the microscopic capture cross sections have been plotted in figures 33 and 34 for the thermal and fast energy ranges, respectively. The non-capture and photonuclear macroscopic cross sections of the natural parent nuclides are shown in Figures 35 and 36, respectively.

In the analyses, natural materials are used for the parent isotopes. The initial atomic density of the parent nuclide N_p^0 is given by equation 1, where d_{nat} is the natural density of the parent material, A is the Avogadro's number, f is the natural abundance of the parent nuclide in the parent material and W the atomic weight of the parent material.

$$N_p^0 = \frac{d_{nat} \cdot A \cdot f}{W} \qquad 1)$$

The atomic density N of the daughter nuclides (medical isotopes) has been calculated by solving the system of equation 2a, whose solution is reported in equation

2b, where λ is the decay constant of the daughter nuclide, N_p is the density of the parent nuclide, and $\sigma_p \Phi$ is the parent reaction rate. The latter parameter has been obtained by multiplying the reaction rate per source particle (electron), obtained from the MCNPX calculations, for the number of electrons per second from the 100 kW beam power with 200 MeV electrons. The MCNPX standard deviation is lower than 0.3% for all reaction rates, with the exception of the (n,2n) reaction rate. In all analyses, the daughter term ($\sigma\Phi$) has been neglected due to its low value relative to the decay constant (medical isotopes have short-life nuclides).

$$\begin{cases} \dfrac{dN}{dt} = -(\lambda + \sigma\Phi)N + \sigma_p N_p \Phi \\ \dfrac{dN_p}{dt} = -\sigma_p N_p \Phi \end{cases} \qquad 2a)$$

$$N(t) = \sigma_p \Phi N_p^0 \frac{e^{-\sigma_p \Phi t} - e^{-(\lambda+\sigma\Phi)t}}{\lambda + \sigma\Phi - \sigma_p \Phi} \qquad 2b)$$

When daughter nuclides are generated by a grandparent, with density N_{gp}, and a parent with density N_p, the atomic densities have been calculated using the equation set 3a of linear differential equations, whose general solution is given by formulas 3b. The solution presented in formulas 3b applies both to the case of a stable parent, by setting λ_p equal to zero, as in the case of ^{177m}Lu production (equation 4a), and to the case of a decaying parent, by setting N_p^0 equal zero, as in the case of ^{47}Sc and ^{188}W production (equations 4b and 4c). The ^{177m}Lu production assumes that 0.1% of the ^{176}Lu neutron captures trigger the nucleus excitation.

$$\begin{cases} \dfrac{dN}{dt} = -(\lambda + \sigma\Phi)N + \sigma_p N_p \Phi \\ \dfrac{dN_p}{dt} = -(\lambda_p + \sigma_p \Phi) \cdot N_p + \sigma_{gp} N_{gp} \Phi \\ \dfrac{dN_{gp}}{dt} = -\sigma_{gp} N_{gp} \Phi \end{cases} \qquad 3a)$$

$$\begin{cases} N = \sigma_p \Phi N_p^0 \dfrac{e^{-(\lambda_p+\sigma_p\Phi)t} - e^{-(\lambda+\sigma\Phi)t}}{\lambda + \sigma\Phi - \lambda_p - \sigma_p\Phi} + \dfrac{\sigma_p \Phi N_{gp}^0 \sigma_{gp} \Phi}{\lambda_p + \sigma_p \Phi - \sigma_{gp}\Phi} \left[\dfrac{e^{-\sigma_{gp}\Phi t} - e^{-(\lambda+\sigma\Phi)t}}{\lambda + \sigma\Phi - \sigma_{gp}\Phi} - \dfrac{e^{-(\lambda_p+\sigma_p\Phi)t} - e^{-(\lambda+\sigma\Phi)t}}{\lambda + \sigma\Phi - \lambda_p - \sigma_p\Phi} \right] \\ N_p = N_p^0 e^{-(\lambda_p+\sigma_p\Phi)t} + \sigma_{gp}\Phi N_{gp}^0 \dfrac{e^{-\sigma_{gp}\Phi t} - e^{-(\lambda_p+\sigma_p\Phi)t}}{\lambda_p + \sigma_p\Phi - \sigma_{gp}\Phi} \\ N_{gp} = N_{gp}^0 e^{-\sigma_{gp}\Phi t} \end{cases} \qquad 3b)$$

$$Lu_{177m} = 0.001 \cdot \sigma_{176}\Phi Lu^0_{176} \frac{e^{-0.001\cdot\sigma_{176}\Phi t} - e^{-\lambda_{177m}t}}{\lambda_{177m} - 0.001\cdot\sigma_{176}\Phi} +$$
$$+ \frac{0.001\cdot\sigma_{176}\Phi\sigma_{175}\Phi Lu^0_{175}}{(0.001\cdot\sigma_{176} - \sigma_{175})\Phi}\left[\frac{e^{-\sigma_{175}\Phi t} - e^{-\lambda_{177m}t}}{\lambda_{177m} - \sigma_{175}\Phi} - \frac{e^{-0.001\cdot\sigma_{176}\Phi t} - e^{-\lambda_{177m}t}}{\lambda_{177m} - 0.001\cdot\sigma_{176}\Phi}\right] \qquad 4a)$$

$$Sc_{47} = \frac{\sigma_{46}\Phi Sc^0_{45}\sigma_{45}\Phi}{\lambda_{46} + \sigma_{46}\Phi - \sigma_{45}\Phi}\left[\frac{e^{-\sigma_{45}\Phi t} - e^{-\lambda_{47}t}}{(\lambda_{47} - \sigma_{45}\Phi)} - \frac{e^{-(\lambda_{46}+\sigma_{46}\Phi)t} - e^{-\lambda_{47}t}}{\lambda_{47} - \lambda_{46} - \sigma_{46}\Phi}\right] \qquad 4b)$$

$$W_{188} = \frac{\sigma_{187}\Phi W^0_{186}\sigma_{186}\Phi}{\lambda_{187} + \sigma_{187}\Phi - \sigma_{186}\Phi}\left[\frac{e^{-\sigma_{186}\Phi t} - e^{-\lambda_{188}t}}{(\lambda_{188} - \sigma_{186}\Phi)} - \frac{e^{-(\lambda_{187}+\sigma_{187}\Phi)t} - e^{-\lambda_{188}t}}{\lambda_{188} - \lambda_{187} - \sigma_{187}\Phi}\right] \qquad 4c)$$

The production of ^{99m}Tc represents a special case, since the assumption of an instantaneously β decay of the parent ^{99}Mo is not applicable; consequently, the appropriate system of equations becomes:

$$\begin{cases} \dfrac{dTc_{99m}}{dt} = -(\lambda_{Tc99m} + \sigma_{Tc99m}\Phi)Tc_{99m} + \lambda_{Mo99}Mo_{99} \\ \dfrac{dMo_{99}}{dt} = -(\lambda_{Mo99} + \sigma_{Mo99}\Phi)Mo_{99} + \sigma_{Mo98}\Phi Mo_{98} \\ \dfrac{dMo_{98}}{dt} = -\sigma_{Mo98}\Phi Mo_{98} \end{cases} \qquad 5a)$$

Whose solution is:

$$Tc_{99m} = \frac{\lambda_{Mo99}\sigma_{Mo98}\Phi N^0_{Mo98}}{\lambda_{Mo99} + \sigma_{Mo99}\Phi - \sigma_{Mo98}\Phi}\left[\frac{e^{-\sigma_{Mo98}\Phi t} - e^{-(\lambda_{Tc99m}+\sigma_{Tc99m}\Phi)t}}{\lambda_{Tc99m} + \sigma_{Tc99m}\Phi - \sigma_{Mo98}\Phi} - \frac{e^{-(\lambda_{Mo99}+\sigma_{Mo99}\Phi)t} - e^{-(\lambda_{Tc99m}+\sigma_{Tc99m}\Phi)t}}{\lambda_{Tc99m} + \sigma_{Tc99m}\Phi - \lambda_{Mo99} - \sigma_{Mo99}\Phi}\right] \qquad 5b)$$

Once the atomic densities have been calculated by the previous formulas, the specific activity evaluation has been carried out by equation 6.

$$\text{specific activity} = \frac{\lambda N}{d_{nat}} \qquad 6)$$

The neutron spectrum in the four irradiation locations is shown in Figure 37. The irradiation location in the graphite reflector has the largest thermal neutron flux and the lowest fast neutron flux compared to the other three locations. The first irradiation location has a thermal neutron flux close to the value of the fourth location and the highest neutron flux in the slowing down region because of the water coolant of the target assembly. The second and third locations have the highest fast neutron flux and the lowest thermal neutron flux because they are located at the center of fuel assemblies away from large moderator zones.

The photon spectrum above 1 MeV is shown in Figure 38 for the first irradiation location where it has the highest value. In the MCNPX analyses, one MeV threshold energy has been set for photon transport to reduce the computation time since photonuclear cross sections have negligible values below this energy. The obtained photon spectrum has a smooth profile, as expected from the Bremsstrahlung effect, with exception of two peaks in the energy ranges of 2.2 to 2.3 and 7.7 to 7.8 MeV. These peaks are caused by the (n,γ) reaction with ^{1}H of the water and of ^{27}Al of the aluminum alloy, respectively. In the first case, the emitted photon has energy of 2.24 MeV, corresponding to the binding energy of the deuteron nucleus.

The calculated specific activities of the medical isotopes, for the four irradiation locations, are shown in Figures 39 through 73. After 15 irradiation days: ^{82}Br, ^{64}Cu, ^{165}Dy, ^{166}Ho, ^{192}Ir, ^{194}Ir, ^{186}Re, ^{188}Re and ^{153}Sm have a specific activity larger than 100 MBq/mg and they can be easily produced in the Kharkov facility. ^{60}Co, ^{51}Cr, ^{159}Gd, ^{24}Na, ^{32}P (via (n,γ)), and ^{90}Y have a specific activity between 10 and 100 MBq/mg. ^{111}Ag, ^{125}I, ^{42}K, ^{99}Mo, ^{32}P (via (n,p)), ^{99m}Tc and ^{133}Xe (via (n,γ)) have a specific activity between 1 and 10 MBq/mg. ^{58}Co, ^{67}Cu, ^{59}Fe, ^{177m}Lu, ^{33}P, ^{103}Pd, ^{35}S, ^{47}Sc, ^{188}W and ^{133}Xe (via (n,2n) and (n,p)) have a specific activity < 1 MBq/mg. ^{58}Co, ^{60}Co, ^{51}Cr, ^{59}Fe, ^{125}I, ^{192}Ir, ^{177m}Lu, ^{33}P, ^{35}S, ^{47}Sc, and ^{188}W require an irradiation time longer than 100 days to reach saturation. The obtained results define also the best location for generating each isotope, reported in Table V.

Figures 74-83 display the activities of the medical isotopes that are obtained as fission products of ^{235}U. In this case, the parent material is 20% enriched metallic uranium and the fourth irradiation location maximizes the fission reaction rate because of the large thermal fission cross section of the ^{235}U isotope. After 15 irradiation days: ^{89}Sr, ^{99m}Tc and ^{133}Xe have a specific activity higher than 10 MBq/mg. ^{111}Ag, ^{77}As, ^{137}Cs, ^{129}I and ^{90}Sr have a specific activity lower than 1 MBq/mg. ^{131}I, ^{99}Mo,. ^{137}Cs, ^{129}I, ^{89}Sr and ^{90}Sr require an irradiation time longer than 100 days to reach saturation.

In general, the results show that:

- Isotopes generated through large thermal cross sections are better produced in the fourth location (in the graphite reflector) because of the highest thermal neutron fraction.
- Isotopes generated through resonances in the slowing down energy range are better produced in the first location (in the target water channel) because of the highest epithermal neutron fraction.
- Isotopes generated through threshold cross sections, e.g. (n,2n) and (n,p), are better produced in the second location (inside the fuel assembly next to the target) because of the highest fast neutron fraction.

The specific activities of the medical isotopes generated through photonuclear reactions are shown in Figures 84 through 92 for the first irradiation location, which maximizes the photon flux due to its vicinity to the target assembly. The reaction rates

have been obtained by multiplying the EXFOR microscopic reaction cross sections and the MCNPX photon flux. After 15 irradiation days, all nuclides: ^{74}As, ^{139}Ce, ^{57}Co, ^{64}Cu, ^{55}Fe, ^{99}Mo, ^{33}P, ^{88}Y and ^{89}Zr have a specific activity below 1 MBq/mg. ^{139}Ce, ^{57}Co, ^{55}Fe, and ^{88}Y require an irradiation time longer than 100 days to reach saturation.

VI. Specific Activities of Radioactive Isotopes with Self-Shielding

In order to evaluate the self-shielding effect on the previous results for the strong absorbers parents (^{59}Co, ^{63}Cu, ^{165}Ho, ^{191}Ir, ^{193}Ir, ^{175}Lu, ^{185}Re, ^{187}Re, ^{152}Sm, and ^{187}W), the analyses have been repeated when the parent material samples fill the irradiations volumes. In this case, the sample heights were reduced from 30 to 5 cm to minimize the impact on the reactivity of the subcritical assembly. Samarium isotopes 147, 149, 150 and 152 were used to represent the natural samarium material since the other samarium isotopes (144, 148, and 154) are small and unavailable from ENDF/B nuclear data library. Therefore, the samarium natural density has been decreased down to 4.73 g/cm^3 in the MCNPX analyses. Figures 93 through 102 compare the specific activities without and with self-shielding and also show the corresponding macroscopic cross section of the parent nuclides. Few general observations emerge:

- At the fourth irradiation location, the self-shielding effect increases as the macroscopic cross section value of the parent nuclide for producing the radioactive isotope at 10^{-5} eV increases. In the thermal energy range, the microscopic cross sections exhibit the 1/v linear dependence, which explains this behavior.
- At first and fourth locations, the high resonances of the microscopic cross sections increase the self-shielding effect. However, this effect is observed more in the first irradiation location due to its high neutron flux in the slowing down energy range. Figure 37 shows that the thermal neutron flux is about the same at the first and fourth irradiation locations but the epithermal neutron flux of the first irradiation location is much larger than the fourth location.
- The irradiation of a natural material with multiple isotopes (copper, iridium, lutetium, rhenium, samarium and tungsten) enhances the self-shielding effect due to the resonances overlapping (for the first location) or the high value at the thermal energy (for the fourth location) of the microscopic cross sections. The effect is amplified at the first irradiation location because of its high neutron flux in the slowing down energy range.

At 10^{-5} eV neutron energy, the (n,γ) macroscopic cross sections of ^{63}Cu, ^{165}Ho and ^{59}Co are ~10, 100 and 200 cm^{-1}, respectively. These cross section values changes to ~1 cm^{-1} at neutron energies of 0.001, 0.1 and 0.1 eV, respectively. The calculated self-shielding factors for the specific activity of the daughter isotopes at the fourth irradiation location are 1.16, 3.8, and 3.3, respectively. The comparison between ^{165}Ho and ^{59}Co is simplified since their abundances are 100% in the natural elemental form. At the fourth irradiation location, the self-shielding factor for ^{60}Co is smaller than the corresponding value for ^{166}Ho although the thermal (n,γ) macroscopic cross section, at neutron

energies of 10^{-5} and 0.1 eV, is about double (Figures 93 and 95). The higher (n,γ) macroscopic cross section of ^{165}Ho, for neutron energy above 2 eV, than the corresponding macroscopic cross section of ^{59}Co, explains the obtained results. Because of the high resonances of the microscopic cross section in the slowing down energy range, the fourth irradiation location is the best for producing ^{166}Ho isotope, which is different result if the self-shielding effect is ignored.

For the production of ^{64}Cu, the resonances overlapping of ^{63}Cu and ^{65}Cu reduces the production of ^{64}Cu in the first location more than in the fourth one. The same effect is observed for the production of ^{192}Ir, ^{194}Ir, ^{185}Re, ^{187}Re and ^{188}W (that contributes only 28% to natural tungsten) isotopes. The analysis without self-shielding effect predicted the maximal production for these isotopes in the first irradiation location but the analyses with the self-shielding effect show the fourth irradiation location has the maximum production rate. The very high macroscopic cross section of the parent isotopes diminishes the specific activity of the daughters isotopes by a factor up to 30, in agreement with independent studies performed on the TRIGA Portuguese Nuclear Reactor.[14-15] The self-shielding analyses show that the first and fourth irradiation locations produces the same specific activities for ^{188}W and ^{194}Ir. Due to the high capture resonances between 1-1000 eV, compared to the thermal cross section value, of ^{175}Lu, the production of ^{177m}Lu isotope is maximized in the first irradiation location (Figure 98). For ^{153}Sm production, the self-shielding effect, enhanced by the presence of ^{149}Sm, which has a very high thermal capture cross section (Figure 101), reduces the specific activity by a factor of 30 (Figure 101); the first irradiation location has the highest production rate since ^{152}Sm neutron capture at the fourth irradiation location is shadowed by ^{149}Sm.

The self-shielding analyses reveal that all isotopes are better produced in the 4th location, with the exception of ^{153}Sm and ^{177m}Lu, which are better produced in the 1st location; however, the specific activity of the latter isotope is very small.

VII. Sample Size Analyses

In order to select an optimal sample size for each medical isotope, further investigations were performed to determine the axial and radial spatial distributions of the parent reaction rates. The axial profiles have been tallied over a very fine axial mesh that divided the sample into 200 disks with a constant height of 0.15 cm and a radius of 0.3 cm. The same approach has been repeated for the radial profiles; the sample has been divided into 30 concentric cylindrical shells with equal volume. Both the axial and radial profiles are shown in figures 103 to 122 for the different isotopes. The plotted reaction rate has been calculated by using equation 7.

$$(\text{Reaction Rate})_{V_i} = \frac{1}{V_i}\int_{V_i} d\vec{r}\int dE\int N_p\sigma_p\varphi(\vec{r},E,\vec{\Omega})d\vec{\Omega} = \Sigma_p\Phi \qquad (7)$$

$$V_1 = V_2 = V_3 = \ldots = V_i = V_{i+1} = \ldots \qquad 8)$$

The axial distributions in the fourth irradiation location show that the reaction rate variation (maximum to minimum) is less than 1.33 for all isotopes when the end points are excluded (Figures 103 through 107, 109, 110, and 112). In addition, the axial distribution has a cosine shape which follows the neutron flux distribution in the subcritical assembly. Therefore, a sample length of 30 cm or less can be used for producing the medical isotopes at the fourth irradiation location. At the first irradiation location, the reaction rate variation is less than 1.48 and the reaction distribution follows the axial flux distribution along the target zone when the end points are excluded. Again, a sample length of 30 cm can be used for generating the radioactive isotopes. In all of the axial distributions, the reaction rates in the first and last disk are higher than their neighbor points. The peak of the ^{175}Lu axial distribution between 5 and 7 cm (Figure 108) is caused by neutron thermalization from the water under the target; this peak is mitigated for the case of ^{152}Sm because thermal neutrons in samarium are mainly absorbed by ^{149}Sm.

All the radial distributions exhibit an exponential shape and the gradient is a function of the parent cross section as shown in Figures 113 through 122. The gradient is very large for the parent material with a very large cross section such as ^{193}Ir; consequently, the optimal sample diameter depends on the parent material cross section. For copper material, the radius of 0.3 is acceptable and thick wires can be used; for iridium wires, the diameter needs to be ~0.1 cm to avoid reducing the specific activity per unit volume. The plotted results can be used to select the wire diameter.

VIII. Conclusions

This study has shown the excellent capability of the Kharkov facility to produce isotopes for medical applications. After 15 irradiation days: ^{82}Br, ^{64}Cu, ^{165}Dy, ^{166}Ho, ^{192}Ir, ^{194}Ir, ^{186}Re, ^{188}Re, and ^{153}Sm have a specific activity larger than 100 MBq/mg and therefore they can be easily produced in the Kharkov facility. These parents have a large microscopic absorption cross section and an accurate evaluation of the specific activity requires the account of the self-shielding effect. The latter phenomenon can reduce the specific activity by a factor up to 30 and it also changes the irradiation location that maximizes the specific activity. Generally, the optimal irradiation location lies in reflector next to a fuel assembly, where the neutron flux has a thermal spectrum. At the fourth irradiation location, the axial distribution exhibits a cosine shape and the radial one an exponential attenuation. The optimal wire sample size can have a length up to 30 cm and a radius of 0.1 to 0.3 cm.

REFERENCES

[1] Y. GOHAR, J. BAILEY, H. BELCH, D. NABEREZHNEV, P. STRONS and I. BOLSHINSKY, "Accelerator-Driven Subcritical Assembly: Concept Development and Analyses." RERTR-2004 International Meeting on Reduced Enrichment for Research and Test Reactors, 2004.

[2] Y. GOHAR, I. BOLSHINSKY, D. NABEREZHNEV, J. DUO, H. BELCH and J. BAILEY, "Accelerator-Driven Subcritical Facility: Conceptual Design Development," Nuclear Instruments & Methods in Physics Research A 562, pp. 870-874, 2006.

[3] D. NABEREZHNEV, Y. GOHAR, J. BAILEY and H. BELCH, "Physics Analyses of an Accelerator-Driven Subcritical Assembly," Nuclear Instruments & Methods in Physics Research A 562, pp. 841-844, 2006.

[4] Y.M. ADO, K.A. BELOVINTSEV and S.N. STOLYAROV, "The Bremsstrahlung Spectrum of Electrons with an Energy of 260 MeV," Atomic Energy 12/3, pp. 193-197, 1962.

[5] C.D. BOWMAN, G.F. AUCHAMPAUGH and S.C. FULTZ, "Photodisintegration of ^{235}U," Physical Review 133/3b, pp. 676-683, 1964.

[6] M.B. CHADWICK, P.G. YOUNG, R.E. MACFARLANE, M.C. WHITE, and R.C. LITTLE, "Photonuclear Physics in Radiation Transport—I: Cross Sections and Spectra," Nuclear Science and Engineering 144, pp. 157-173, 2003.

[7] M.L. GIACRI-MAUBORGNE, D. RIDIKAS, M.B. CHADWICK, P.G. YOUNG, and W.B. WILSON, "Photonuclear Physics in Radiation Transport—III: Actinide Cross Sections and Spectra," Nuclear Science and Engineering 153, pp. 33-40, 2006.

[8] D. RIDIKAS, M.L. GIACRI, M.B. CHADWICK, J. C. DAVID, D. DORE´, X. LEDOUX, A. Van LAUWE AND W.B. WILSON, "Status of the photonuclear activation file: Reaction cross-sections, fission fragments and delayed neutrons," Nuclear Instruments & Methods in Physics Research A 562, pp. 710-713, 2006.

[9] S.J. ADELSTEIN, T.F. BUDINGER, R.E. COLEMAN, D. DANFORD, W.C. ECKELMAN, J.A. NOLEN, L.L. RIEDINGER, T.J. RUTH, L.S. SCHROEDER, M.J. WELCH, S.W. YATES, "Isotopes for Medicine and Life Science," National Academy Press, ISBN 0-309-05190-8, 1995.

[10] K.A.Van RIPER, S.G. MASHNIK and W.B. WILSON, "A computer study of radionuclide production in high power accelerators for medical and industrial applications," Nuclear Instruments & Methods in Physics Research A 463, pp. 576-585, 2001.

[11] J.S. HENDRICKS et al. MCNPX, VERSION 2.6.B. LA-UR-06-3248, 2006.

[12] S. MIRZADEH, C.W. ALEXANDER, T. Mc MANAMY and F.F. KNAPP, "Projected Medical Radioisotope Production Capabilities of the Advanced Neutron Source (ANS)," Oak Ridge National Laboratory, ORNL/TM-10210-S, 1994.

[13] http://www.uic.com.au/nip26.htm.

[14] M. NEVES, A. KLING and R.M. LAMBRECHT, "Radionuclide Production for Therapeutic Radiopharmaceuticals," Applied Radiation and Isotopes 57, pp. 657-664, 2002.

[15] M. Do CARMO LOPES and J. MOLINA AVILA, "Multiple Scattering Resonance Self Shielding Factors in Foils," Nuclear Instruments & Methods in Physics Research A 280, pp. 304-309, 1989.

Table I. Geometrical data of the Kharkov electron driven subcritical facility

Subcritical Assembly	
Height/Radius [cm]	200/80
Graphite Reflector Height [cm]	61.2042
Apothem of the Hexagonal Lattice of the Fuel and Reflector Zone [cm]	1.75
Height/Radius of the Vacuum Beam Pipe Channel [cm]	120.005/3.84145
Height/Thickness of the Aluminum Beam Pipe Tube [cm]	120.005/0.2
Target	
Height/Radius [cm]	11.99/3.84145
Height/Radius of the Water Layers [cm]	0.175/3.84145
Height/Radius of the 11 Natural Uranium Disks [cm]	0.3x5;0.4;0.5;0.6;0.9;1.2;2.8/3.77145
Thickness of the Top/Bottom Aluminum Disk [cm]	0.2/0.4
Thickness of the Aluminum Cladding (Natural Uranium Disks) [cm]	0.07
Water Channels	
Thickness of the Aluminum Water Channels [cm]	0.2
Height of the 6 Aluminum Half-Hexagonal Shells [cm] (starting at 33.0355 cm, see figure 10)	72.3282
Height of the 4 Aluminum Half-Hexagonal Shells [cm] (starting at 105.3637 cm, see figure 19)	44.6363
Height of the 2 Aluminum Sector-Cylindrical Shells [cm] (starting at 68.405 cm, see figures 14 and 15)	11.39
Height of the 4 Aluminum Plate [cm] (starting at 68.005 cm, see figure 13)	0.4
Fuel	
Internal/External Radii of the Inner Cylindrical Fuel Shell [cm]	0.399/0.501
Internal/External Radii of the Central Cylindrical Fuel Shell [cm]	0.996/1.098
Internal/External Apothems of the Outer Hexagonal Fuel Shell [cm]	1.422/1.524
Active/Total Height of the Fuel Zone [cm]	50/61.2042
Thickness of the Aluminum Cladding of the Fuel Shells [cm]	0.076
Height/Radius of the Aluminum Top Fuel Handling [cm]	4.1718/0.55
Height/Radius of the Aluminum Bottom Fuel Handling [cm]	11.124/0.7264
Reflector	
Height/Apothem of the Graphite Hexagonal Block [cm]	120.005/1.66
Thickness of the Water Interstitial Gap [cm]	0.18
Medical Isotopes Tallying Volume	
Sample Height (positioned in the middle of the fuel length) [cm]	30/5
Sample Radius [cm]	0.3

Table II. Material composition of the Kharkov electron driven subcritical facility

Fuel: UO_2-Al (ρ=4.70778 g/cm^3)	^{235}U (6.27); ^{238}U (24.76); ^{27}Al (68.97)
Cladding: Aluminum (ρ=2.7 g/cm^3)	^{27}Al (98.196); ^{28}Si (0.84278); ^{29}Si (4.2674E-2); ^{30}Si (2.8328E-2); C (7.5026E-1); ^{54}Fe (5.6551E-3); ^{56}Fe (8.8771E-2); ^{57}Fe (2.0501E-3); ^{58}Fe (2.7283E-4); ^{63}Cu (2.9406E-2); ^{67}Cu (1.3107E-2); ^{10}B (5.9672E-5); ^{11}B (2.4018E-4)
Coolant: Water (ρ=1.0019 g/cm^3)	^{1}H (66.67); ^{16}O (33.33)
Target: Natural Uranium (ρ=19.05 g/cm^3)	^{235}U (0.73); ^{238}U (99.27)
Graphite: Carbon (ρ=2.3 g/cm^3)	C (100)

Table III. Medical isotopes decay modes and their applications

Isotope	**Decay mode**	**Medical Applications**
^{111}Ag	β	Cancer therapy
^{74}As	ε(66%)β(34%)	Positron emitter
^{77}As	β	Cancer therapy
^{199}Au	β	Rheumatoid arthritis and cancer therapy
^{213}Bi	β(97.91%)α(2.09)	Targeted alpha therapy
^{77}Br	ε	Radioimmunotherapy
^{82}Br	β	Metabolism
^{14}C	β	Metabolism
^{47}Ca	β	Bone formation and cell function
^{109}Cd	ε	Metal alloys analysis and scrap sorting
^{139}Ce	ε	Gamma-ray calibration
^{141}Ce	β	Lung density and myocardial blood flow
^{252}Cf	α	Cervical cancer and gliomas
^{57}Co	ε	Calibration of imaging instruments; gastrointestinal absorption
^{58}Co	ε	Anemia diagnosis; gastrointestinal absorption
^{60}Co	β	External cancer therapy and surgical instruments sterilization
^{51}Cr	ε	Red blood cells labeling and gastro-intestinal protein loss
^{137}Cs	β	Cancer therapy
^{61}Cu	ε	Positron emitter
^{64}Cu	ε(61%) β(39%)	Genetic diseases from copper metabolism (Wilson's and Menkel's diseases) and positron emitter
^{67}Cu	β	Cancer therapy
^{165}Dy	β	Rheumatoid arthritis
^{169}Er	β	Alleviation of arthritis pain in synovial joints
^{253}Es	α	Labeling of antibodies for cancer therapy

^{55}Fe	ε	x-ray fluorescence
^{59}Fe	β	Metabolism in the spleen
^{255}Fm	α	Labeling of antibodies for cancer therapy
^{159}Gd	β	Cancer therapy
^{3}H	β	Tritiated water
^{166}Ho	β	Rheumatoid arthritis and cancer therapy
^{123}I	ε	Organs imaging (brain)
^{125}I	ε	Liver and brain cancers, veinthrombosis in leg and detection of tiny quantities of hormones
^{129}I	β	In vitro diagnosis
^{131}I	β	Thyroid cancer and renal blood flow
^{111}In	ε	Radioimmunotherapy
^{191m}Ir	ι	Cardiovascular angiography
^{192}Ir	ε(4.76%) β(95.24%)	Intravascular brachytherapy
^{194}Ir	β	Cancer therapy
^{42}K	β	Coronary blood flow
^{177}Lu	β	Organs Imaging
^{177m}Lu	ι(78.3%) β(21.7%)	Endocrine Cancers and labeling of antibodies for cancer therapy
^{24}Na	β	Electrolytes within the body
^{32}P	β	Genetics and polycythemia vera (excess of red blood cells)
^{33}P	β	Cancer therapy and genetics
^{103}Pd	ε	Prostate cancer
^{195m}Pt	ι	Pharmacokinetics of antitumor agents
^{186}Re	ε(6.9) β(93.1)	Bone cancer, rheumatoid arthritis and labeling of antibodies for cancer therapy
^{188}Re	β	Thyroid carcinoma, alleviation of pain in bone cancer and angioplasty balloon
^{97}Ru	ε	Hepatobiliary function and tumor localization
^{35}S	β	Genetics (nucleic acid labeling)
^{47}Sc	β	Cancer therapy
^{75}Se	ε	Protein studies (digestive enzymes)
^{145}Sm	ε	Ocular cancer
^{153}Sm	β	Alleviation of pain in bone cancer and labeling of antibodies for cancer therapy
^{85}Sr	ε	Bone formation
^{89}Sr	β	Alleviation of pain in bone and prostate cancers
^{179}Ta	ε	X-ray fluorescence
^{99m}Tc	ι (99.9963%) β (0.0037%)	Organs imaging
^{123m}Te	ι	Lung densities and cardiology
^{117m}Sn	ι	Alleviation of pain in bone cancer
^{133}Xe	β	Lung ventilation; cerebral blood flow
^{88}Y	ε	Radioimmunotherapy
^{90}Y	β	Labeling of antibodies for cancer therapy, cancer therapy and non-Hodgkin's lymphoma
^{169}Yb	ε	Cerebrospinal fluid in the brain
^{89}Zr	ε	Radioimmunotheraphy and positron emitter
^{166}Dy	β	Parent of ^{166}Ho
^{99}Mo	β	Parent of ^{99m}Tc
^{191}Os	β	Parent of ^{191m}Ir
^{194}Os	β	Parent of ^{194}Ir

^{90}Sr	β	Parent of ^{90}Y
^{188}W	β	Parent of ^{188}Re

Table IV. Medical Isotopes produced by neutron and photonuclear reactions

Isotope	Transmutation Chain	Decay Half Life of the Daughters	Abundance of the Parents [%]	Parent Cross Section [b]/ Cumulative Fission Yield [%]	Notes
^{111}Ag	^{110}Pd(n,γ)^{111}Pd(β)	23.4m – 7.45d	11.72	0.232	N
^{111}Ag	^{112}Cd(γ,n)	7.45d	24.13	0.043	IM
^{111}Ag	^{235}U(f)	7.45d	20	1.9E-2%	F
^{74}As	^{75}As(γ,n)	17.77d	100	0.019	I
^{77}As	^{76}Ge(n,γ)^{77}Ge(β)	11.3h – 38.83h	0	0.145	NA
^{77}As	^{75}As(n,γ)^{76}As(n,γ)	1.0778d – 38.83h	100 – 0	4.6 – 20.15	N
^{77}As	^{235}U(f)	38.83h	20	8.5E-3%	F
^{199}Au	^{198}Pt(n,γ)^{199}Pt(β)	30.8m – 3.139d	7.2	3.44	N
^{213}Bi	^{229}Th decay chain	45.59m	0		D
^{77}Br	^{78}Kr(γ,n)	57.036h	0.35		B
^{82}Br	^{81}Br(n,γ)	35.3h	49.31	2.7	N
^{82}Br	^{83}Kr(γ,n)	35.3h	11.5		B
^{14}C	^{12}C(n,γ)^{13}C(n,γ)	Stable – 5730y	98.9 – 1.1	3.44E-3 - 1.44E-3	N
^{14}C	^{14}N(n,p)	5730y	99.634	1.9	N
^{47}Ca	^{46}Ca(n,γ)	4.536d	0.004	0.746	NC
^{109}Cd	^{110}Cd(γ,n)	462.6d	12.49	0.043	IM
^{139}Ce	^{140}Ce(γ,n)	137.640d	88.48	0.074	I
^{141}Ce	^{140}Ce(n,γ)	32.501d	88.48	0.587	N
^{252}Cf	^{235}U(f)	2.645y	20		
^{57}Co	^{58}Ni(γ,p)	271.79d	68.077	0.046	I
^{58}Co	^{59}Co(n,2n)	70.86d	100.	0.01	I
^{58}Co	^{58}Ni(n,p)	70.86d	68.077	0.0012	H
^{60}Co	^{59}Co(n,γ)	5.2714y	100	38	N
^{51}Cr	^{50}Cr(n,γ)	27.7025d	4.345	16.3	N
^{137}Cs	^{136}Xe(n,γ)^{137}Xe(□)	3.818m – 30.07y	8.9	0.266	N
^{137}Cs	^{235}U(f)	30.07y	20	6.22%	F
^{64}Cu	^{63}Cu(n,γ)	12.7h	69.17	4.56	N
^{64}Cu	^{65}Cu(γ,n)	12.7h	30.83	0.018	I

^{67}Cu	^{67}Zn(n,p)	61.83h	4.1	0.0011	N
^{67}Cu	^{68}Zn(γ,p)	61.83h	18.8		B
^{165}Dy	^{164}Dy(n,γ)	2.334h	28.2	2673	N
^{166}Dy	^{164}Dy(n,γ)^{165}Dy(n,γ)	2.334h – 81.6h	28.2 – 0	2673 – 3188	N
^{169}Er	^{167}Er(n,γ)^{168}Er(n,γ)	9.4d	22.95 – 26.8	682 – 2.74	N
^{253}Es	^{235}U(f)	20.47d	20		
^{55}Fe	^{56}Fe(γ,n)	2.73y	91.72	5E-4	I
^{59}Fe	^{58}Fe(n,γ)	44.503d	0.28	1.31	N
^{255}Fm	^{235}U(f)	20.07h	20		
^{159}Gd	^{158}Gd(n,γ)	18.479h	24.84	2.55	N
^{3}H	^{6}Li(n,t)	12.33y	7.5	960	N
^{166}Ho	^{165}Ho(n,γ)	26.83h	100.	67.9	N
^{123}I	^{124}Xe(γ,p)	13.27h	0.1		B
^{125}I	^{124}Xe(n,γ)^{125}Xe(ε)	16.9h – 59.408d	0.1	168	N
^{129}I	^{128}Te(n,γ)^{129}Te(β)	69.6m – 1.57E7y	31.687	0.22	N
^{129}I	^{235}U(f)	1.57E7y	20	0.7%	F
^{131}I	^{130}Te(n,γ)^{131}Te(β)	25m – 8.02070d	33.799	0.3	N
^{131}I	^{235}U(f)	8.02070d	20	2.88%	F
^{111}In	^{112}Sn(γ,p)	2.8047d	0.97		B
^{191m}Ir	^{190}Os(n,γ)^{191}Os(β)	15.4d – 4.94s	26.4 – 0	13.1 –	NB
^{192}Ir	^{191}Ir(n,γ)	73.831d	37.3	954	N
^{194}Ir	^{193}Ir(n,γ)	19.28h	62.7	112	N
^{42}K	^{41}K(n,γ)	12.36h	6.73	1.46	N
^{177}Lu	^{176}Yb(n,γ)^{177}Yb(β)	1.911h–6.734d	12.7 – 0		B
^{177m}Lu	^{175}Lu(n,γ)^{176}Lu(n,γ)	3.78E10y -160.4d	97.41 – 2.59	23.07 – 2097	NE
^{99}Mo	^{98}Mo(n,γ)	65.94h	24.13	0.132	N
^{99}Mo	^{100}Mo(γ,n)	65.94h	9.63	0.0364	I
^{99}Mo	^{235}U(f)	65.94h	20	6.13%	F
^{24}Na	^{23}Na(n,γ)	14.9590h	100	0.53	N
^{191}Os	^{190}Os(n,γ)	15.4d	26.4	13.1	NL
^{194}Os	^{192}Os(n,γ)^{193}Os(n,γ)	30.11h –6y	41 – 0	2 – 38	N
^{32}P	^{31}P(n,γ)	14.262d	100	0.17	N
^{32}P	^{32}S(n,p)	14.262d	95.02	1.89E-5	H

^{32}P	$^{33}S(\gamma,p)$	14.262d	0.75		B
^{33}P	$^{33}S(n,p)$	25.34d	0.75	0.018	I
^{33}P	$^{34}S(\gamma,p)$	25.34d	4.21	9.2E-4	I
^{103}Pd	$^{102}Pd(n,\square)$	16.991d	1.02	3.44	N
^{103}Pd	$^{104}Pd(n,2n)$	16.991d	11.14	0.225	I
^{195m}Pt	$^{195}Pt(n,n')$	4.02d	33.8	0.277	I
^{186}Re	$^{185}Re(n,\gamma)$	3.7183d	37.4	112	N
^{188}Re	$^{187}Re(n,\gamma)$	17.005h	62.6	76.53	N
^{97}Ru	$^{98}Ru(\gamma,n)$	2.9d	1.88		B
^{35}S	$^{34}S(n,\gamma)$	87.32d	4.21	0.228	NO
^{35}S	$^{35}Cl(n,p)$	87.32d	75.77	0.489	NO
^{47}Sc	$^{45}Sc(n,\gamma)^{46}Sc(n,\gamma)$	83.79d – 3.3492d	100 – 0	27.72 – 7.11	N
^{47}Sc	$^{48}Ti(\gamma,p)$	3.3492d	73.8		B
^{75}Se	$^{74}Se(n,\gamma)$	119.779d	0.89	52.77	N
^{75}Se	$^{76}Se(n,2n)$	119.779d	9.36	0.058	I
^{145}Sm	$^{144}Sm(n,\gamma)$	340d	3.1	1.42	N
^{153}Sm	$^{152}Sm(n,\gamma)$	46.284h	26.7	210.3	N
^{117m}Sn	$^{117}Sn(n,n')$	13.60d	7.68	0.09	H
^{85}Sr	$^{84}Sr(n,\gamma)$	64.84d	0.56	0.83	N
^{89}Sr	$^{88}Sr(n,\gamma)$	50.53d	82.58	5.9E-3	N
^{89}Sr	$^{235}U(f)$	50.53d	20	4.69%	F
^{90}Sr	$^{88}Sr(n,\gamma)^{89}Sr(n,\gamma)$	50.53d – 28.78y	82.58 – 0	5.9E-3 – 0.429	N
^{90}Sr	$^{235}U(f)$	28.78y	20	5.73%	F
^{179}Ta	$^{180}W(\gamma,p)$	1.82y	0.13		B
^{99m}Tc	$^{235}U(f)$	6.01h	20	5.4%	F
^{99m}Tc	$^{235}U(f)^{99}Tc(n,n')$	211100y – 6.01h	20 – 0	6.13% – 0.261	HF
^{99m}Tc	$^{98}Mo(n,\gamma)^{99}Mo(\beta)$	65.94h – 6.01h	24.13 – 0	0.132	NG
^{123m}Te	$^{123}Te(n,n')$	119.7d	0.908	0.33	H
^{188}W	$^{186}W(n,\gamma)^{187}W(n,\gamma)$	23.72h – 69.4d	28.6 – 0	38.25 – 63.13	N
^{133}Xe	$^{132}Xe(n,\gamma)$	5.243d	26.9	0.458	N
^{133}Xe	$^{134}Xe(n,2n)$	5.243d	10.4	0.683	I
^{133}Xe	$^{133}Cs(n,p)$	5.243d	100	0.003	I
^{133}Xe	$^{235}U(f)$	5.243d	20	6.6%	F
^{88}Y	$^{89}Y(\gamma,n)$	106.65d	100	0.0013	I
^{90}Y	$^{89}Y(n,\gamma)$	64h	100	1.28	N

^{90}Y	^{235}U(f)^{90}Sr(β)	28.78y – 64h	20	5.73%	F
^{169}Yb	^{168}Yb(n,γ)	32.026d	0.13		B
^{89}Zr	^{90}Zr(γ,n)	78.41h	51.45	8.0E-4	I

Green, yellow and light-blue colors on the "Isotope" column indicate the isotopes studied in the present study by non-fission incident neutron reactions, photonuclear reactions, or fission reactions, respectively. Red color on the "Isotope" column indicates the isotope has not been covered in the present study. Colors on the "Transmutation Chain" column indicate the type of transmutation chain: yellow (β), blue (γ,n), brown (γ,p), gray (f), light-blue (n,p), red (n,t), green (n,2n) and magenta (n,n').

Notes of Table IV	
A	Production requires a 98% enrichment in ^{76}Ge.[5]
B	Nuclear data are not available.
C	Production requires ^{46}Caenrichment.[6]
D	^{229}Th can be produced from neutron transmutation of ^{228}Ra, which is present in natural thorium.
E	The neutron capture reaction leaves the ^{176}Lu target nucleus in the excited state (thermal yield of 0.1%).
F	Thermal cumulative fission yield from a nucleus of mass 235.
G	The beta decay leads to ^{99m}Tc.
H	Cross section evaluated at ~1–1.5 MeV.
I	Cross section evaluated at ~11 MeV.
L	The beta decay leads to ^{191m}Ir.
M	Cross section of natural cadmium.
N	Cross section evaluated at ~ 0.022 – 0.032 eV.
O	For production of ^{35}S, Cross section of ^{35}Cl(n,p) is twice the one of ^{34}S(n,γ) but the mass density of the parent is 1000 times less.

Table V. Best location of the capsules

Medical Isotope	Best Location
^{111}Ag	1
^{82}Br	1
^{58}Co	2
^{60}Co	4
^{51}Cr	4
^{64}Cu	4
^{67}Cu	2
^{165}Dy	4
^{59}Fe	4
^{159}Gd	1
^{166}Ho	1
^{125}I	1
^{192}Ir	1
^{194}Ir	1
^{42}K	4
^{177m}Lu	1
^{99}Mo	1
^{24}Na	4
^{32}P via (n,γ)	4
^{32}P via (n,p)	2
^{33}P	2
^{103}Pd via (n,γ)	1
^{103}Pd via (n,2n)	2
^{186}Re	1
^{188}Re	1
^{35}S	4
^{47}Sc	4
^{153}Sm	1
^{99m}Tc	1

^{188}W	1
^{133}Xe via (n,γ)	1
^{133}Xe via (n,2n)	2
^{133}Xe via (n,p)	2
^{90}Y	4

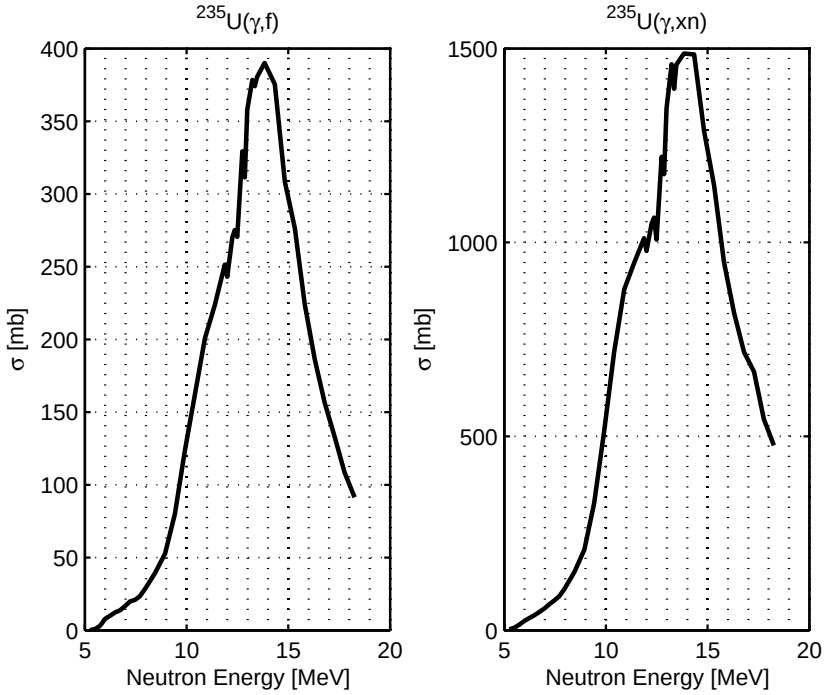

Figure 1. ^{235}U Photo-fission and Photo-neutron Production Cross Sections

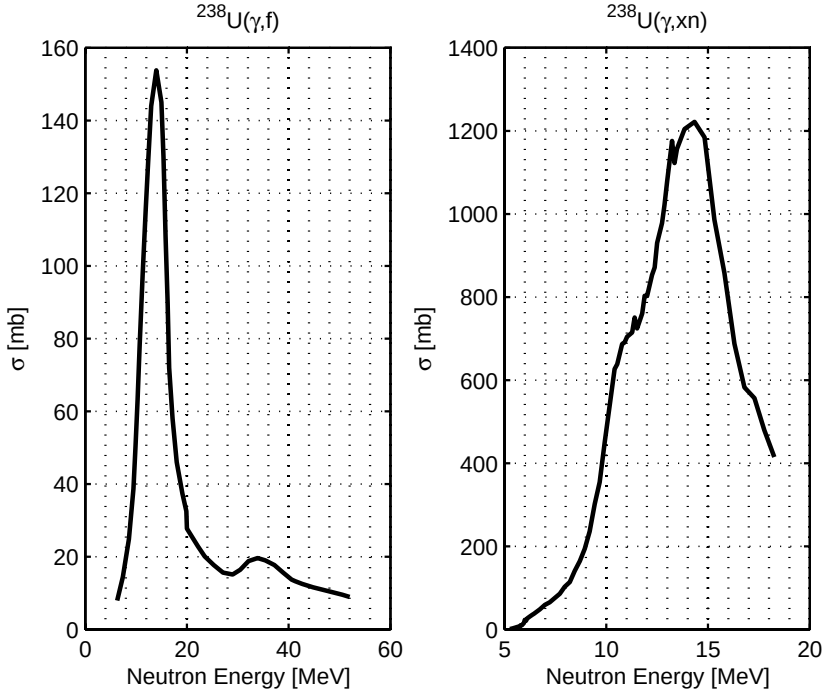

Figure 2. ^{238}U Photo-fission and Photo-neutron Production Cross Sections

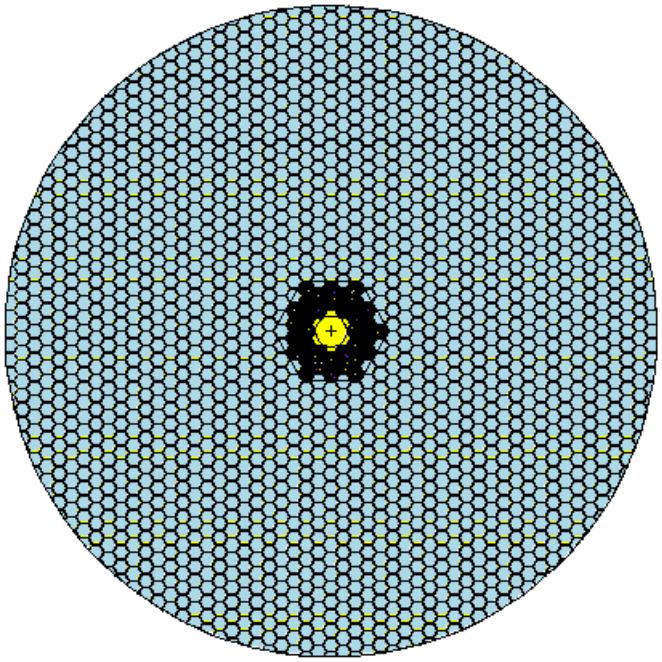

Figure 3. Horizontal section of the subcritical assembly, light blue=graphite, yellow=water, green=natural uranium, purple=aluminum, pink=enriched uranium, white=vacuum

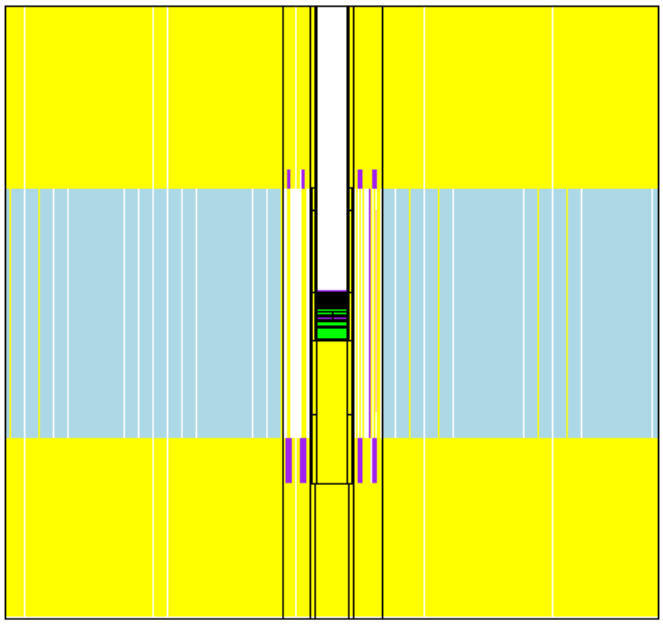

Figure 4. Vertical section the subcritical assembly, light blue=graphite, yellow=water, green=natural uranium, purple=aluminum, pink=enriched uranium, white=vacuum

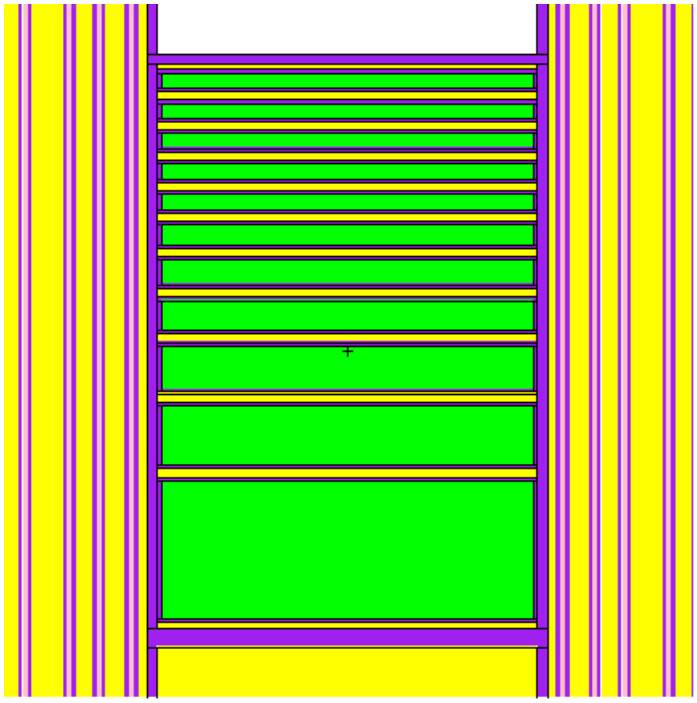

Figure 5. Target vertical section, light blue=graphite, yellow=water, green=natural uranium, purple=aluminum, pink=enriched uranium, white=vacuum

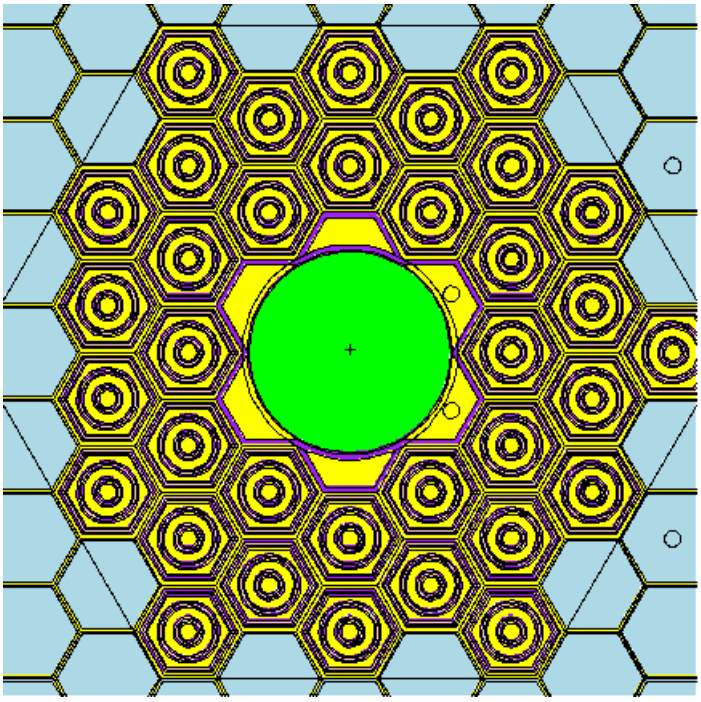

Figure 6. Target and fuel zone horizontal section, light blue=graphite, yellow=water, green=natural uranium, purple=aluminum, pink=enriched uranium, white=vacuum

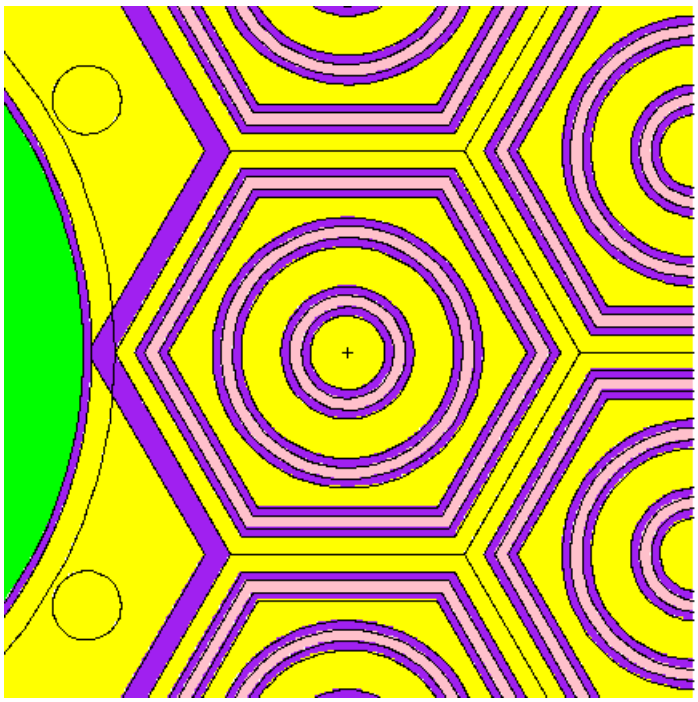

Figure 7. Fuel horizontal section, Light blue=graphite, yellow=water, green=natural uranium, purple=aluminum, pink=enriched uranium, white=vacuum

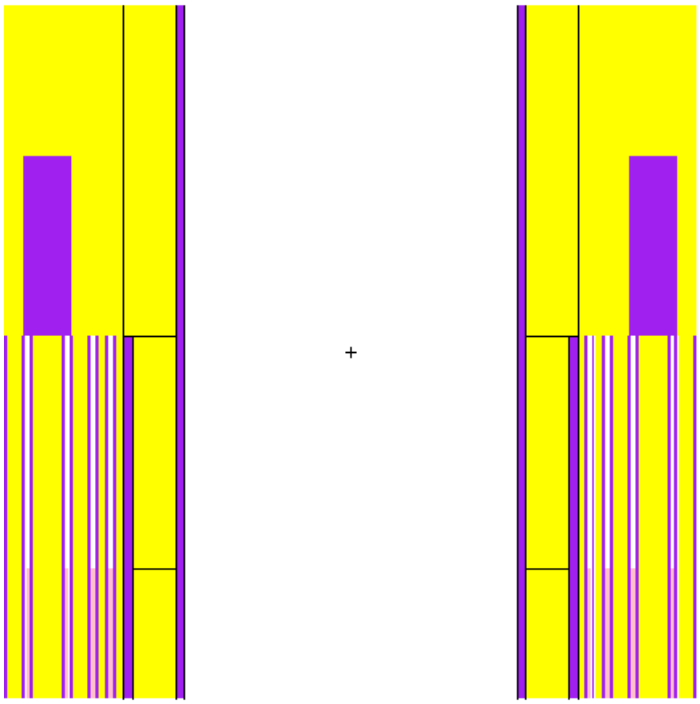

Figure 8. Fuel vertical section, top fuel handling, light blue=graphite, yellow=water, green=natural uranium, purple=aluminum, pink=enriched uranium, white=vacuum

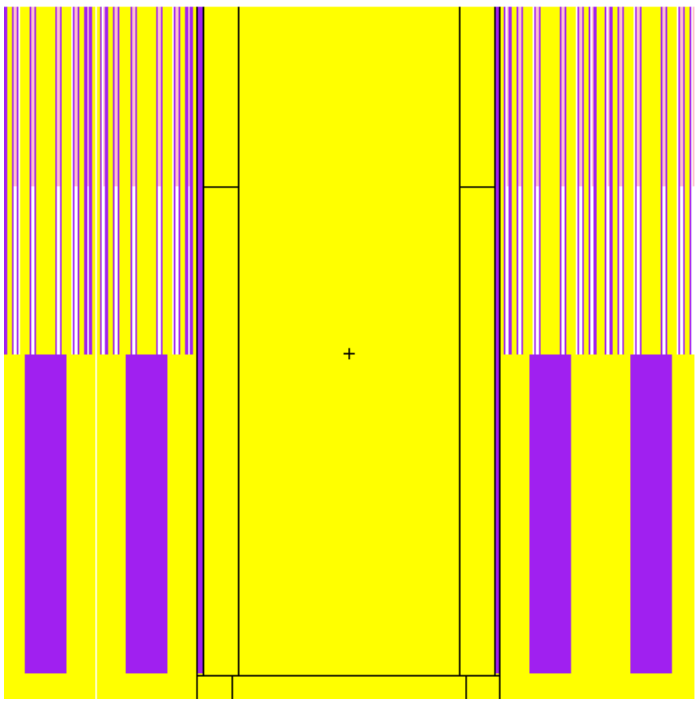

Figure 9. Fuel vertical section, bottom fuel handling, light blue=graphite, yellow=water, green=natural uranium, purple=aluminum, pink=enriched uranium, white=vacuum

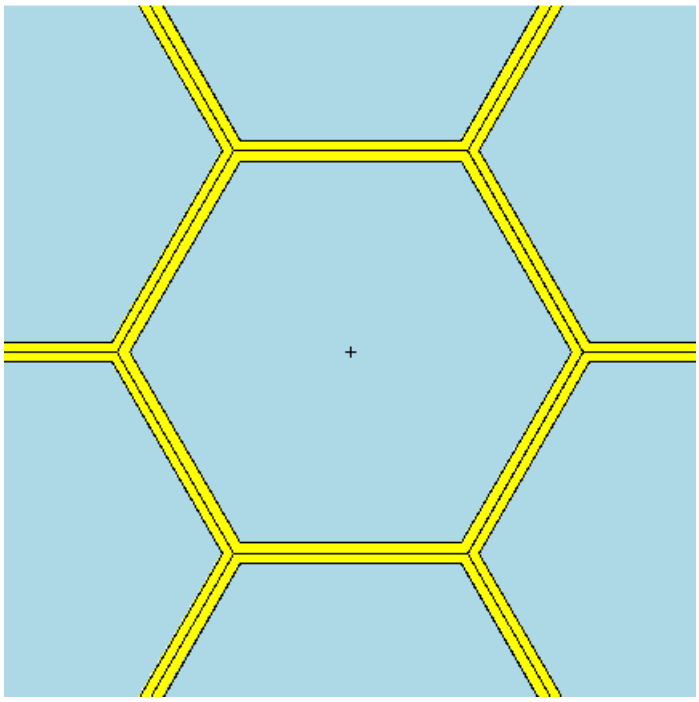

Figure 10. Graphite reflector horizontal cross section, light blue=graphite, yellow=water, green=natural uranium, purple=aluminum, pink=enriched uranium, white=vacuum

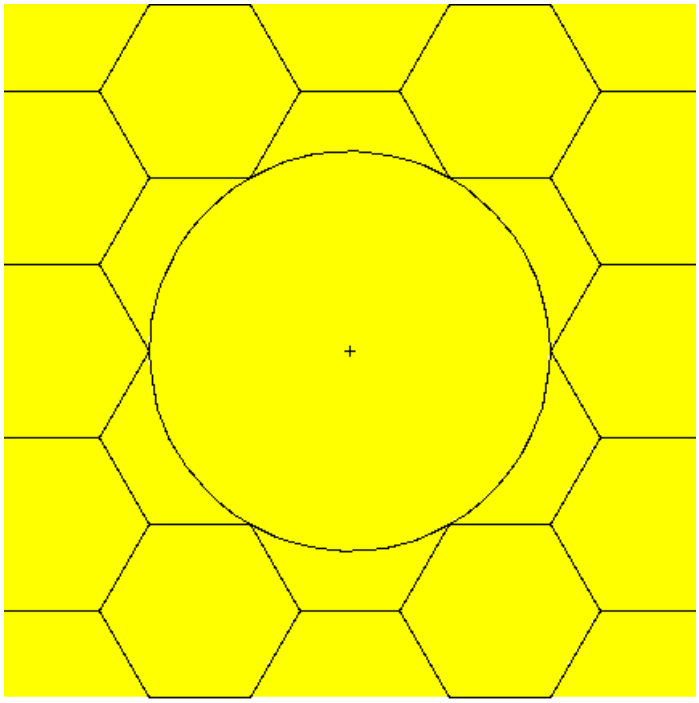

Figure 11. Horizontal section of the target water channels between 0 and 33.0355 cm, light blue=graphite, yellow=water, green=natural uranium, purple=aluminum, pink=enriched uranium, white=vacuum

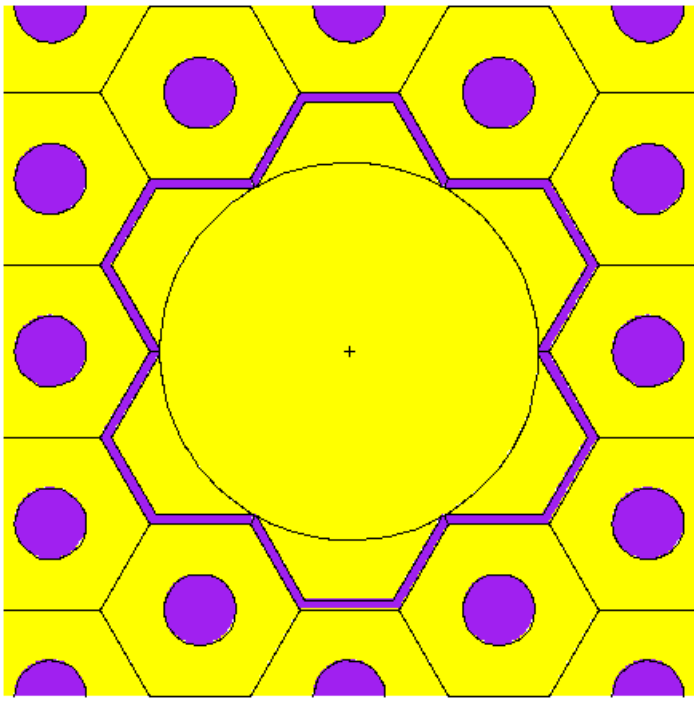

Figure 12. Horizontal section of the target water channels between 33.0355 and 44.1595 cm, light blue=graphite, yellow=water, green=natural uranium, purple=aluminum, pink=enriched uranium, white=vacuum

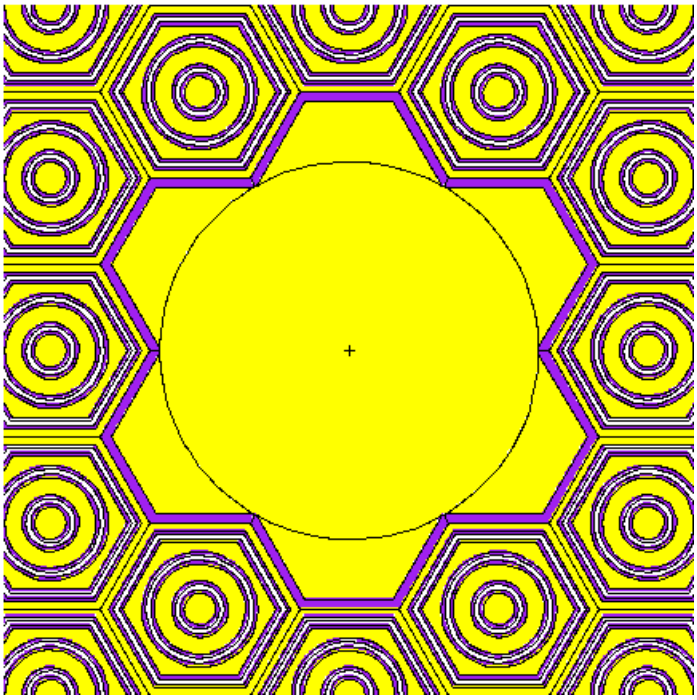

Figure 13. Horizontal section of the water target channels between 44.1595 and 50 cm. light blue=graphite, yellow=water, green=natural uranium, purple=aluminum, pink=enriched uranium, white=vacuum

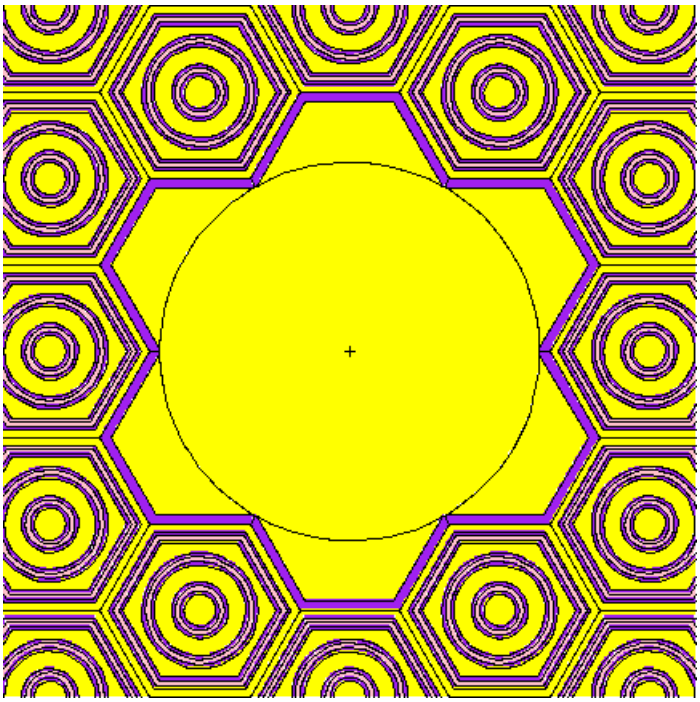

Figure 14. Horizontal cross section of the water target channels between 50 and 68.005 cm, light blue=graphite; yellow=water; green=natural uranium; purple=aluminum; pink=enriched uranium; white=vacuum

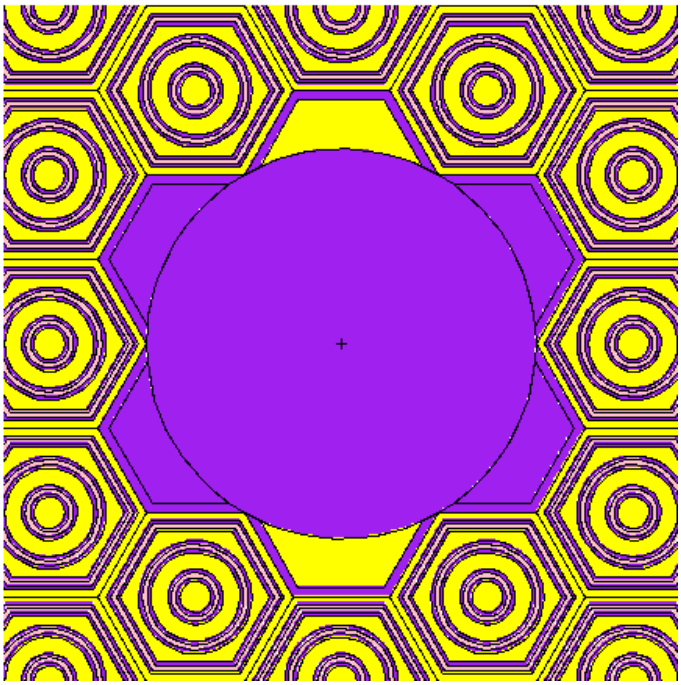

Figure 15. Horizontal cross section of the water target channels between 68.005 and 68.405 cm, Light blue=graphite, yellow=water, green=natural uranium, purple=aluminum, pink=enriched uranium, white=vacuum

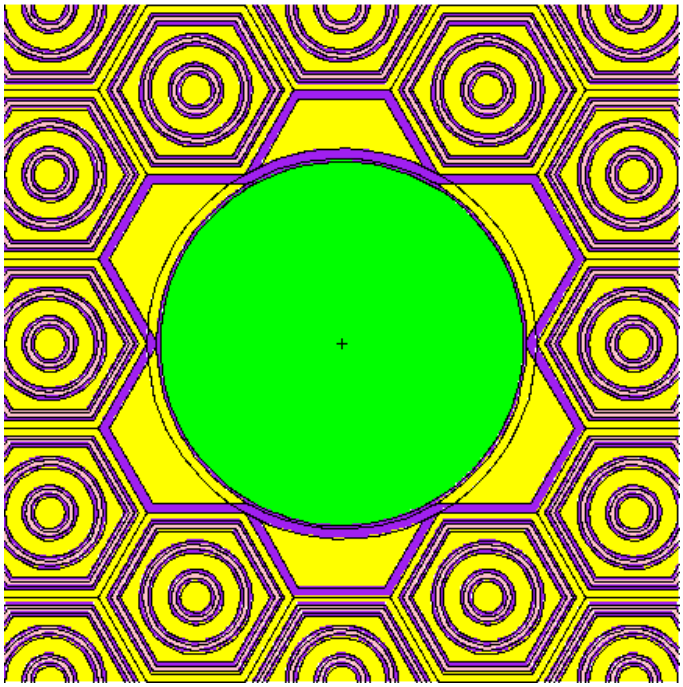

Figure 16. Horizontal cross section of the water target channels between 68.405 and 79.795 cm (target uranium disk), Light blue=graphite, yellow=water, green=natural uranium, purple=aluminum, pink=enriched uranium, white=vacuum

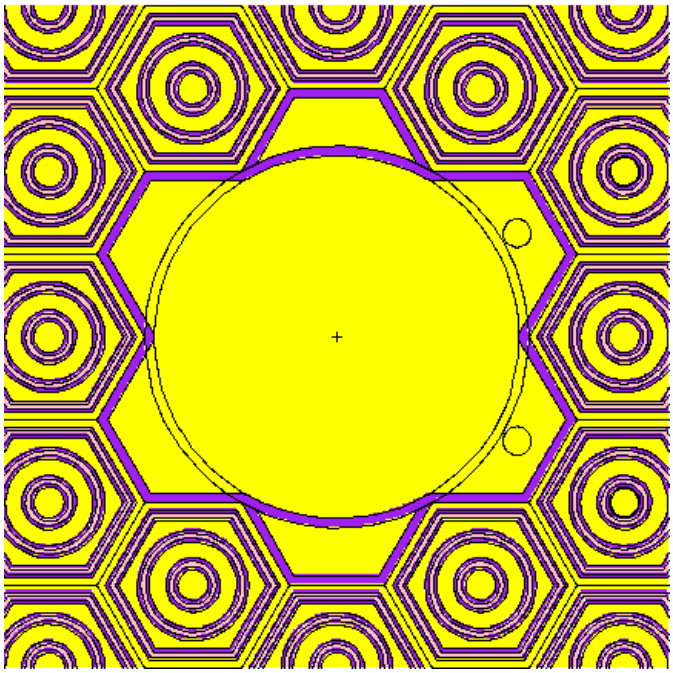

Figure 17. Horizontal section of the water target channels between 68.405 and 79.795 cm (target water layer), Light blue=graphite; yellow=water; green=natural uranium; purple=aluminum; pink=enriched uranium; white=vacuum

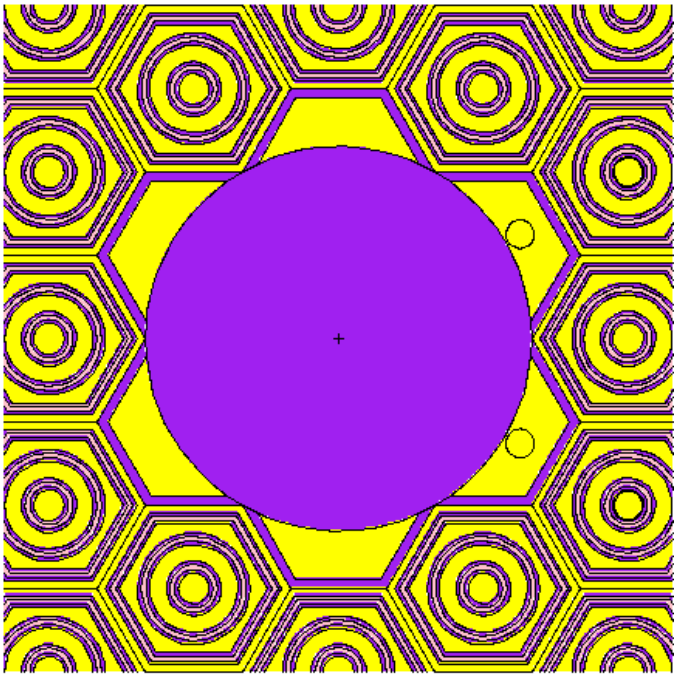

Figure 18. Horizontal cross section of the water target channels between 79.795 and 79.995 cm (target zone changes), light blue=graphite, yellow=water, green=natural uranium, purple=aluminum, pink=enriched uranium, white=vacuum

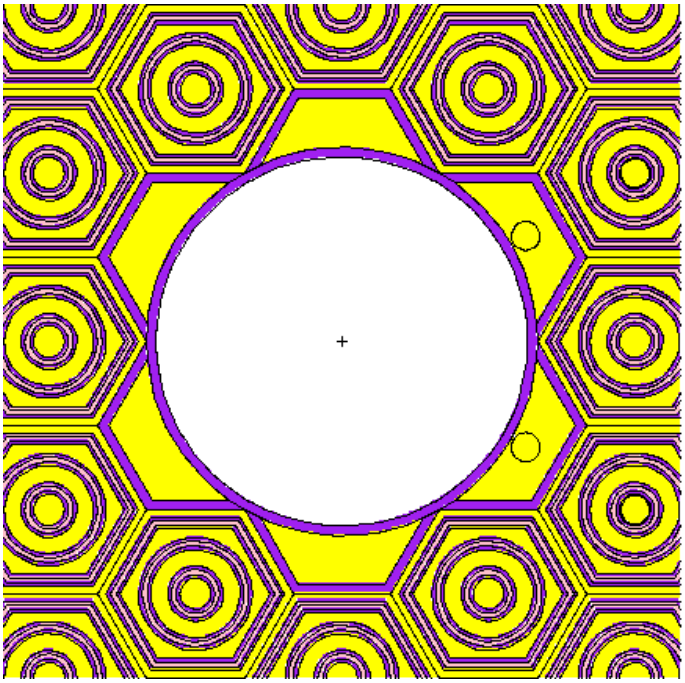

Figure 19. Horizontal cross section of the water target channels between 79.995 and 100 cm, light blue=graphite, yellow=water, green=natural uranium, purple=aluminum, pink=enriched uranium, white=vacuum

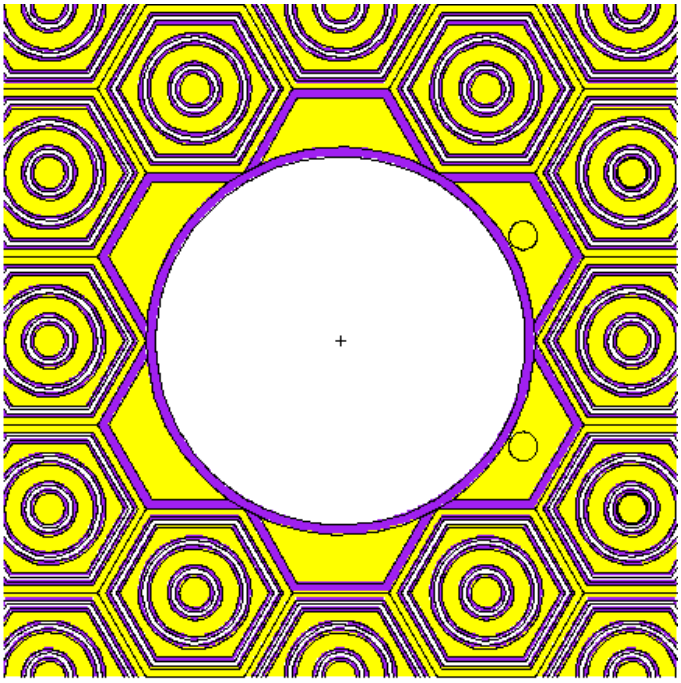

Figure 20. Horizontal cross section of the water target channels between 100 cm and 105.3637 cm, light blue=graphite, yellow=water, green=natural uranium, purple=aluminum, pink=enriched uranium, white=vacuum

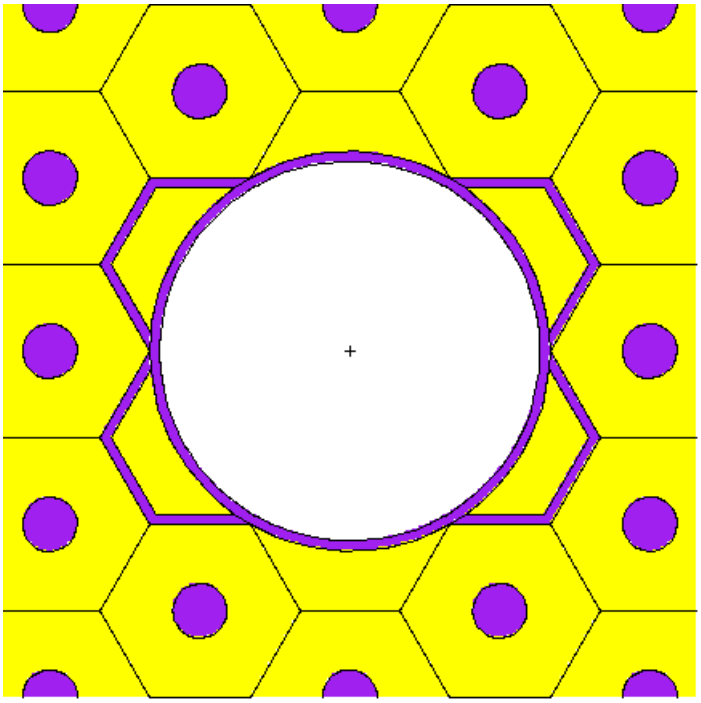

Figure 21. Horizontal cross section of the water target channels between 105.3637 and 109.5355 cm, light blue=graphite, yellow=water, green=natural uranium, purple=aluminum, pink=enriched uranium, white=vacuum

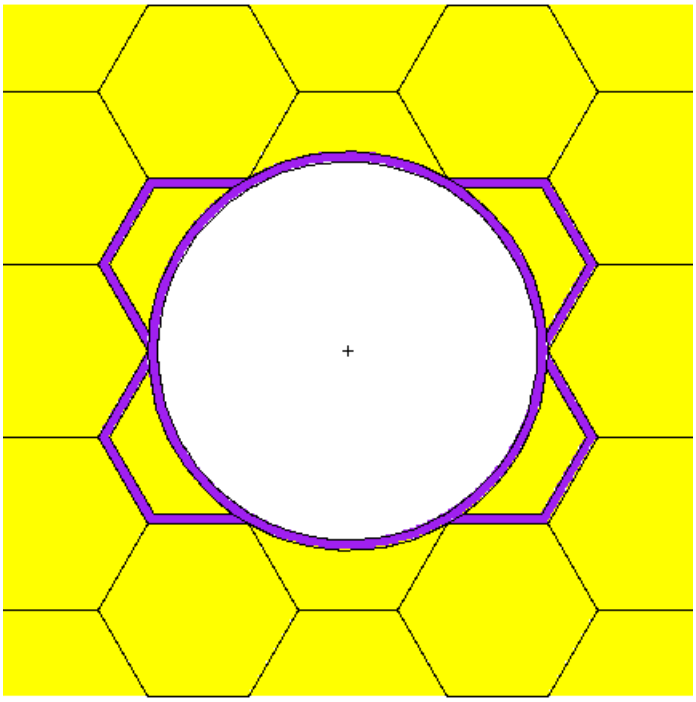

Figure 22. Horizontal cross section of the water target channels between 109.5355 and 150 cm, light blue=graphite, yellow=water, green=natural uranium, purple=aluminum, pink=enriched uranium, white=vacuum

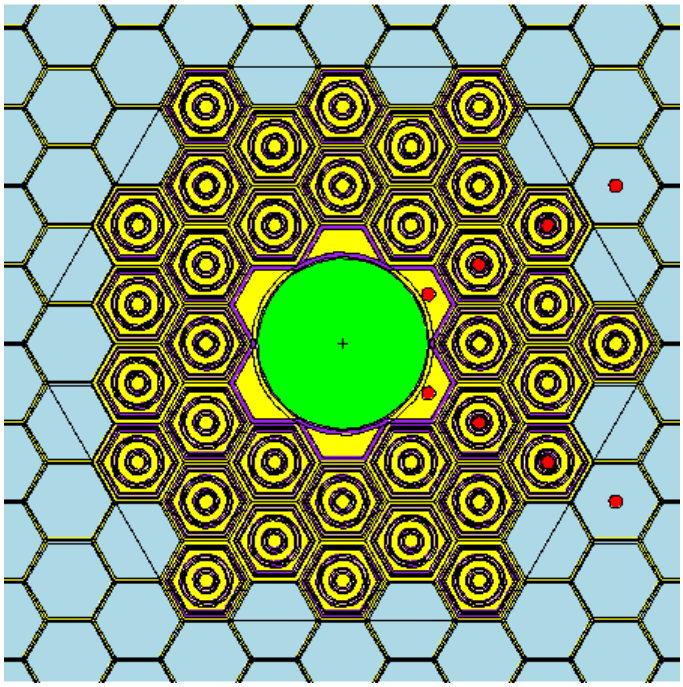

Figure 23. Irradiation locations, red circles, for the medical isotope production, light blue=graphite, yellow=water, green=natural uranium, purple=aluminum, pink=enriched uranium, white=vacuum

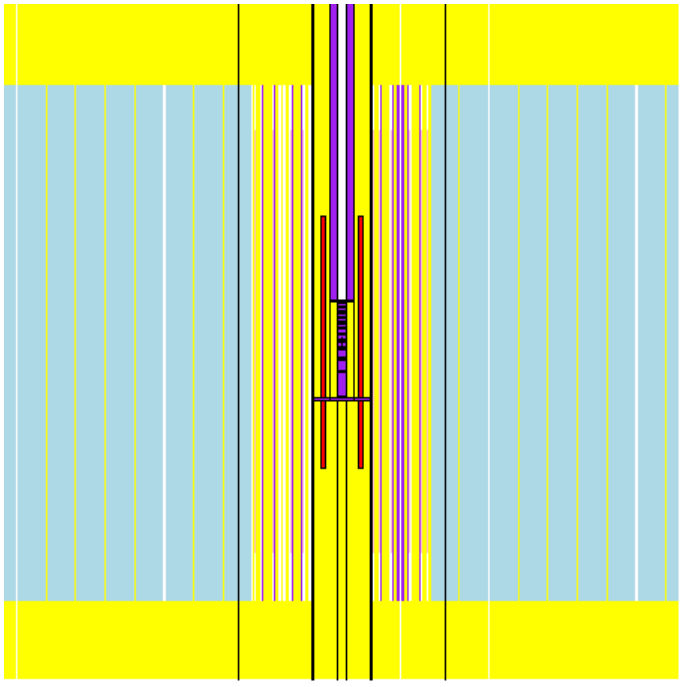

Figure 24. Vertical cross section at x=3.8 cm showing the irradiation locations next to the target, red color, light blue=graphite, yellow=water, green=natural uranium, purple=aluminum, pink=enriched uranium, white=vacuum

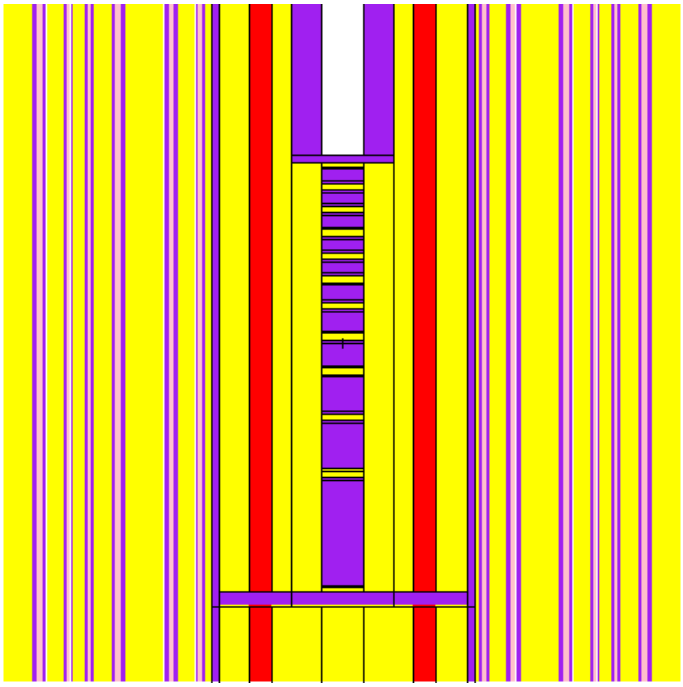

Figure 25. Vertical cross section zoom in at x=3.8 cm showing the irradiation locations next to the target, red color, light blue=graphite, yellow=water, green=natural uranium, purple=aluminum, pink=enriched uranium, white=vacuum

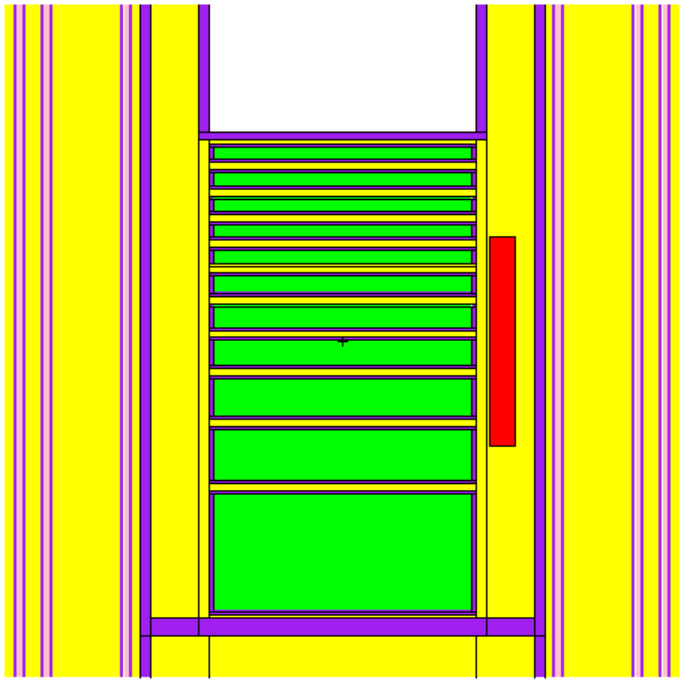

Figure 26. Vertical cross section at y=2.19 cm showing the irradiation locations used for the self shielding calculations of the medical isotope production next to the target, red color, light blue=graphite, yellow=water, green=natural uranium, purple=aluminum, pink=enriched uranium, white=vacuum

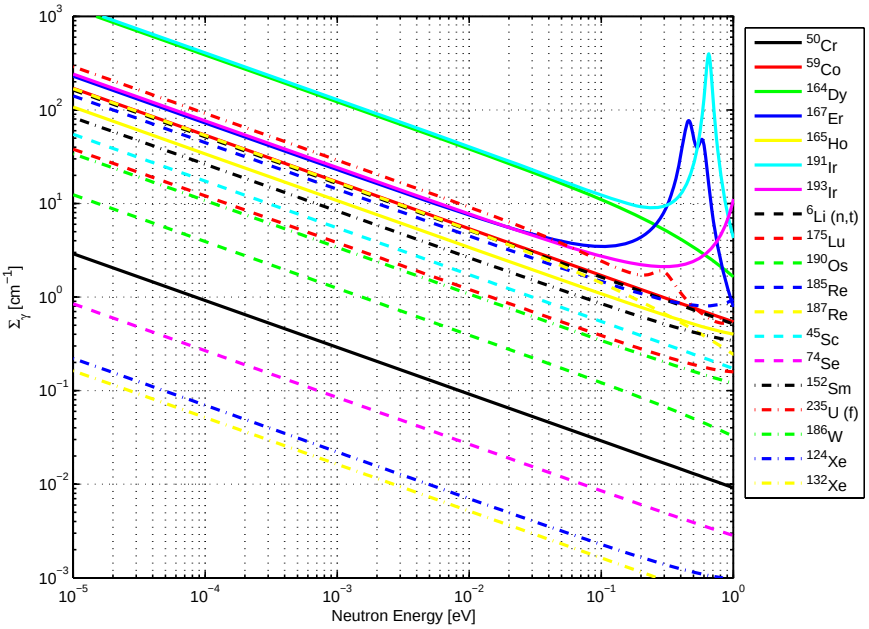

Figure 27. (n,γ) macroscopic cross section of the parent nuclides with σ_γ>10 b in the thermal energy range using natural elemental composition, ^{6}Li reaction is (n,t), ^{235}U fission reaction used 20% abundance, and ^{59}Co and ^{187}Re reactions are also given

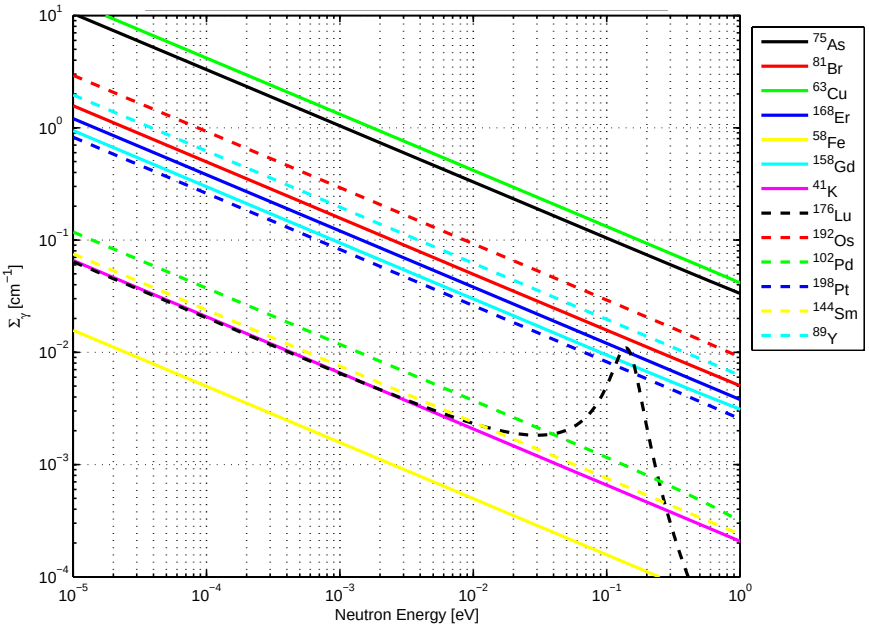

Figure 28. (n,γ) macroscopic cross section of the parent nuclides with $\sigma_{\gamma \in}$ [1-10] b in the thermal energy range using natural elemental composition, the capture cross section of ^{176}Lu is multiplied by the ^{177m}Lu production yield (about 0.001)

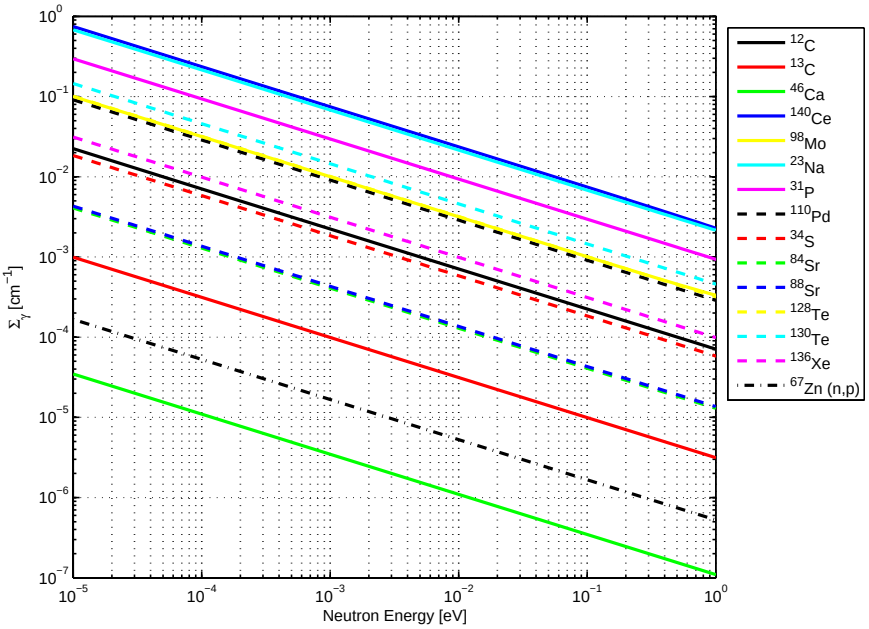

Figure 29. (n,γ) macroscopic cross section of the parent nuclides with σ_γ<1 b in the thermal energy range using natural elemental composition, (n,p) reaction is given for ^{67}Zn, ^{98}Mo, and ^{128}Te reactions are also given

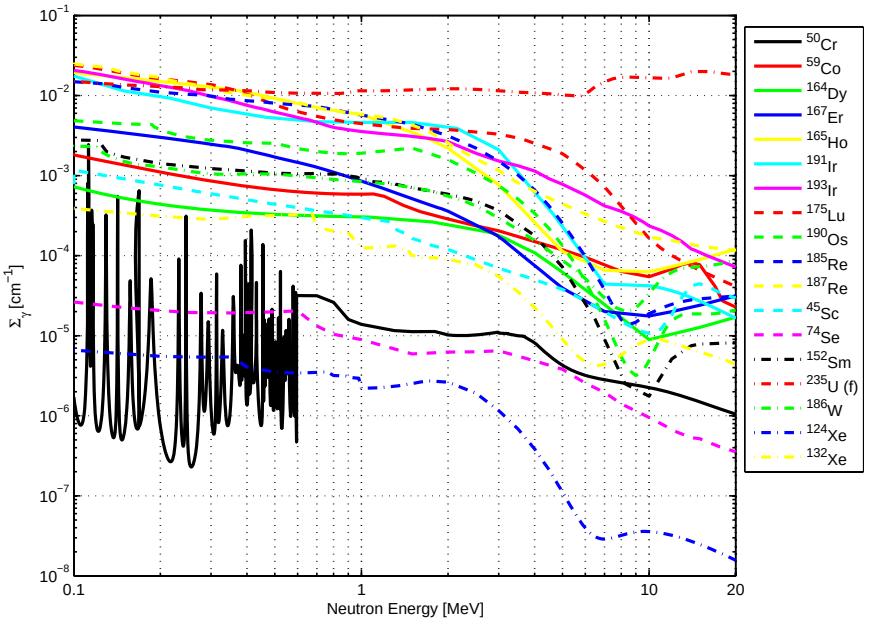

Figure 30. (n,γ) macroscopic cross section of the parent nuclides with σ_γ>10 b in the fast energy range using natural elemental composition, ^{235}U fission reaction used 20% abundance

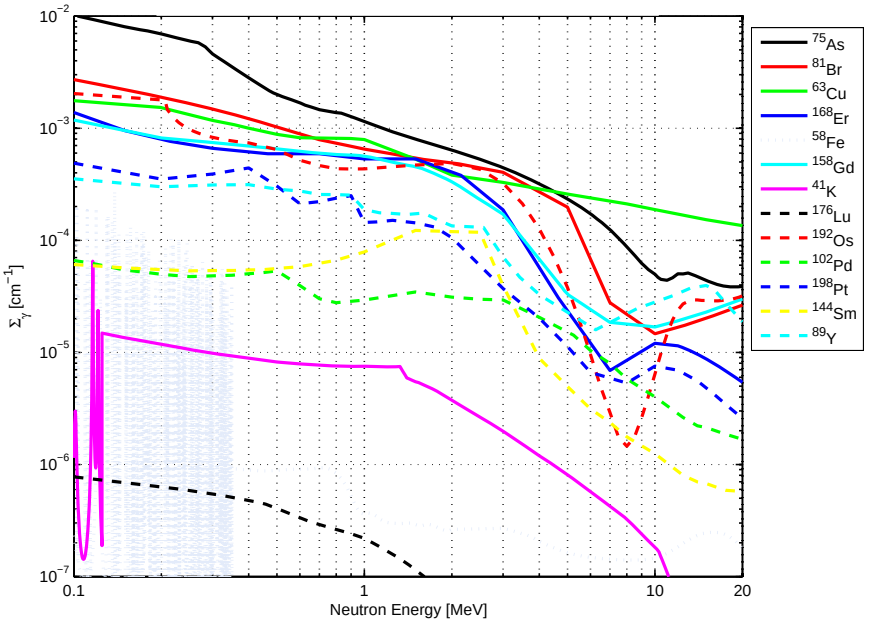

Figure 31. (n,γ) macroscopic cross section of the parent nuclides with $\sigma_{\gamma} \in$ [1-10] b in the fast energy range using natural elemental composition, the capture cross section of ^{176}Lu is multiplied by the ^{177m}Lu production yield (about 0.001)

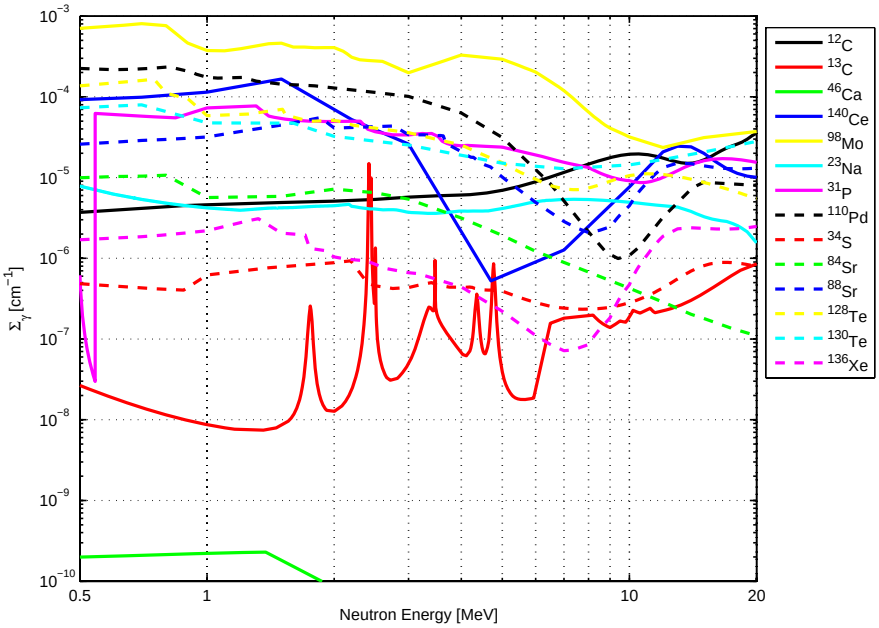

Figure 32. (n,γ) macroscopic cross section of the parent isotopes with σ_{γ}<1 b in the fast energy range using natural elemental composition

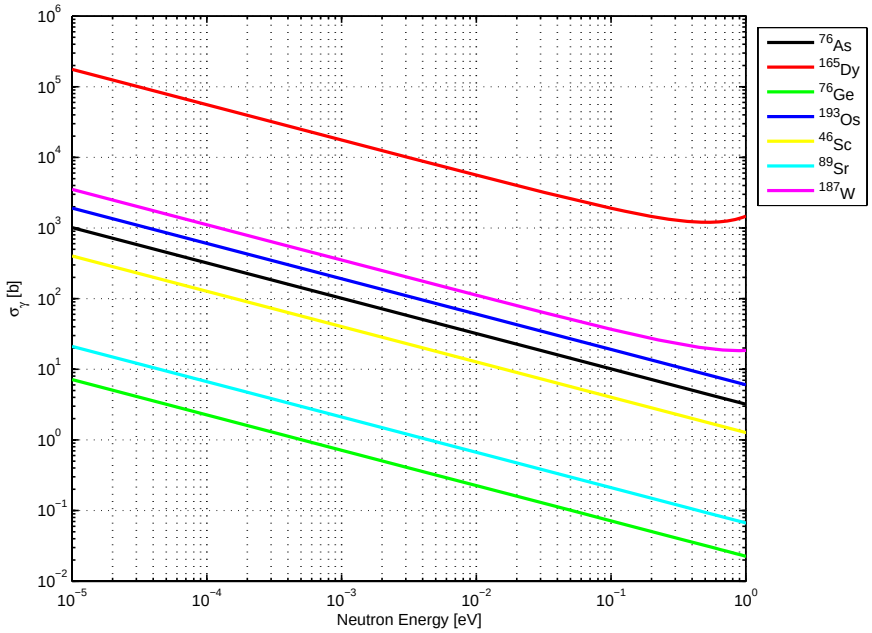

Figure 33. (n,γ) microscopic cross section of the radioactive parent isotopes in the thermal energy range

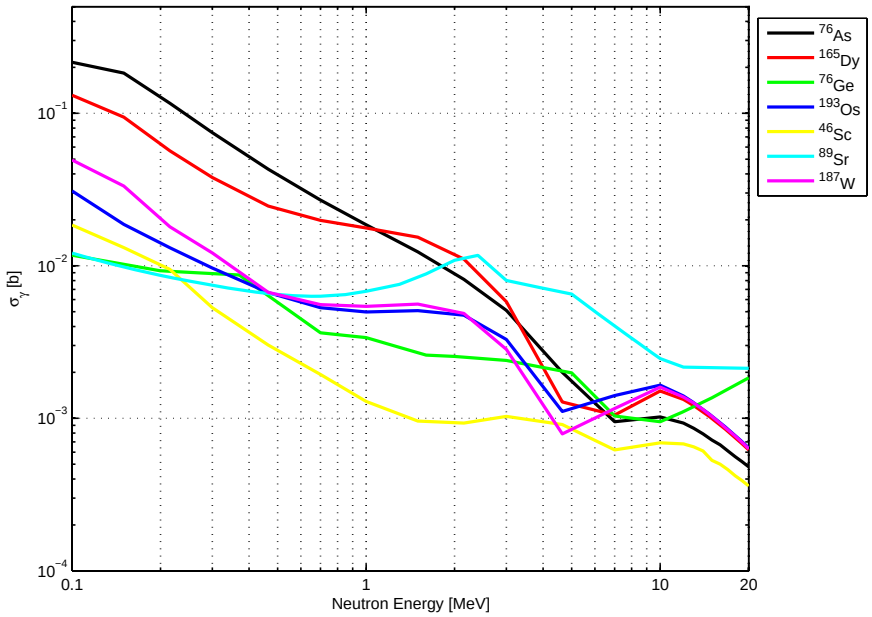

Figure 34. (n,γ) microscopic cross section of the parent isotopes that do not exist in nature

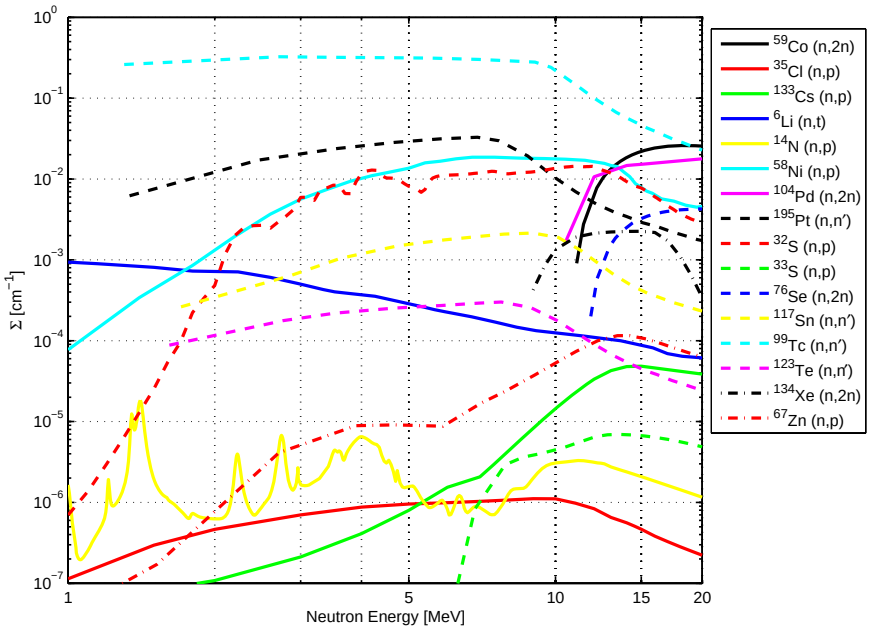

Figure 35. Macroscopic partial neutron cross section of the parent nuclides using natural elemental composition, cross section of ^{99}Tc is microscopic [b]

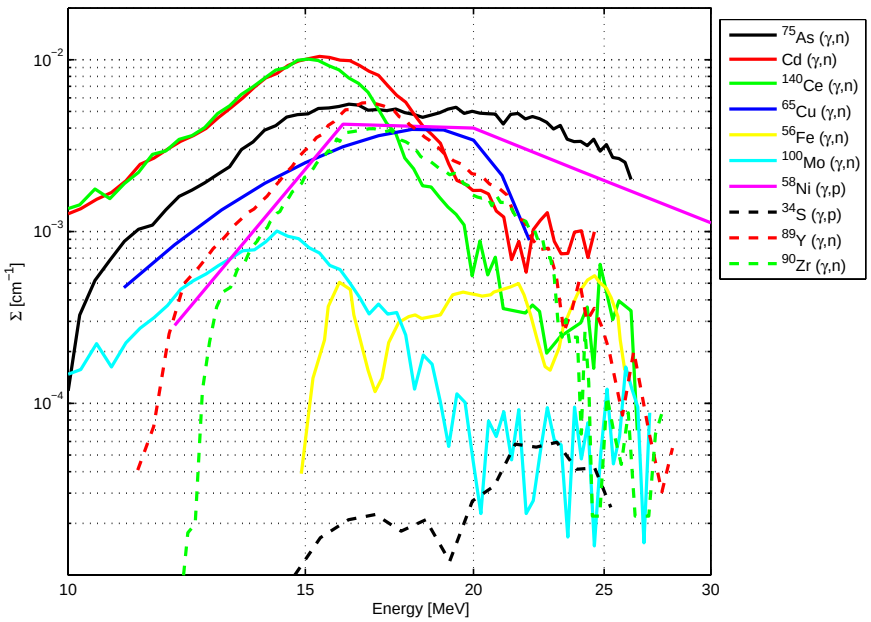

Figure 36. Macroscopic photonuclear cross section of the parent nuclides using natural elemental composition

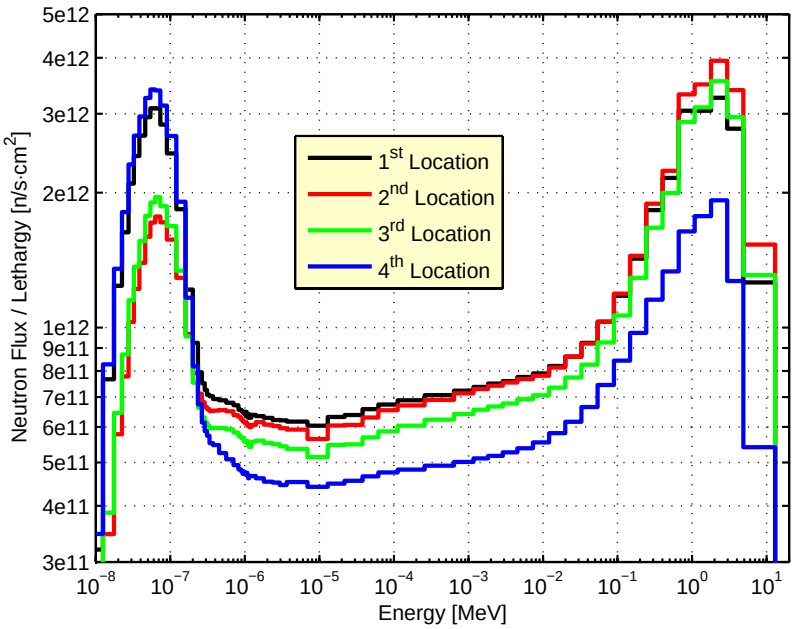

Figure 37. Neutron spectrum in the four locations

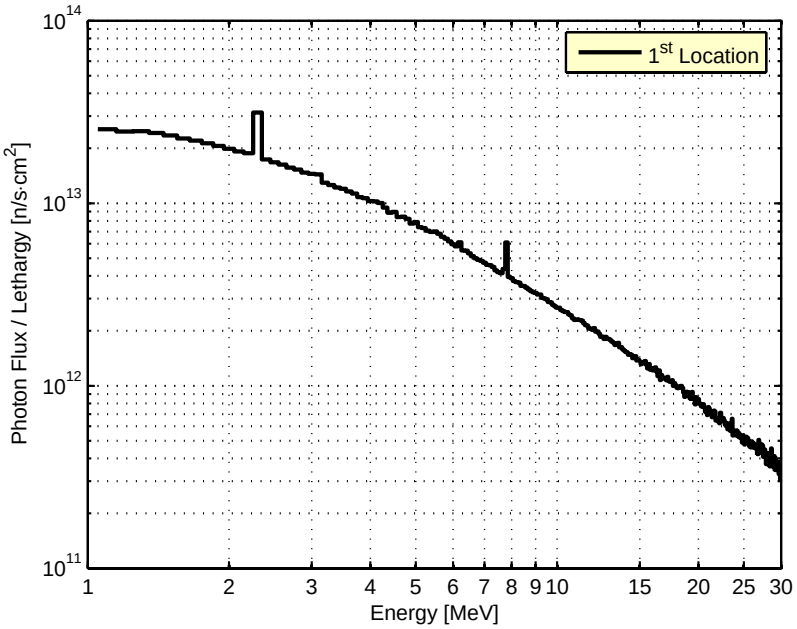

Figure 38. Photon spectrum in the first location

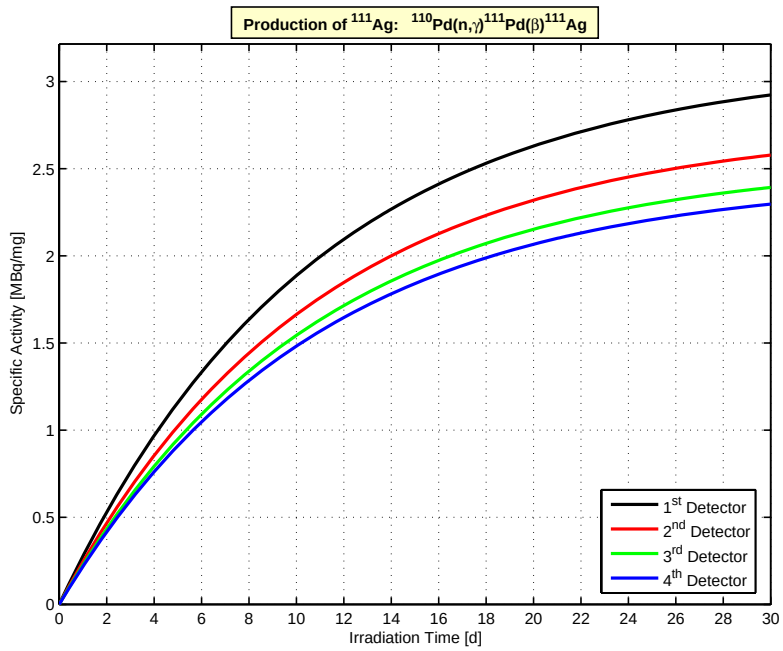

Figure 39. ^{111}Ag activity as a function of the irradiation time

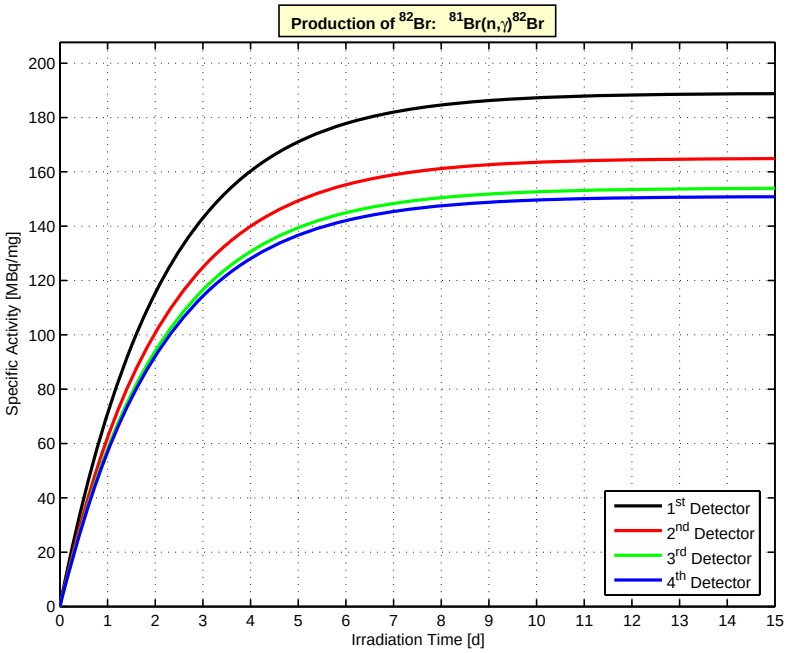

Figure 40. ^{82}Br activity as a function of the irradiation time

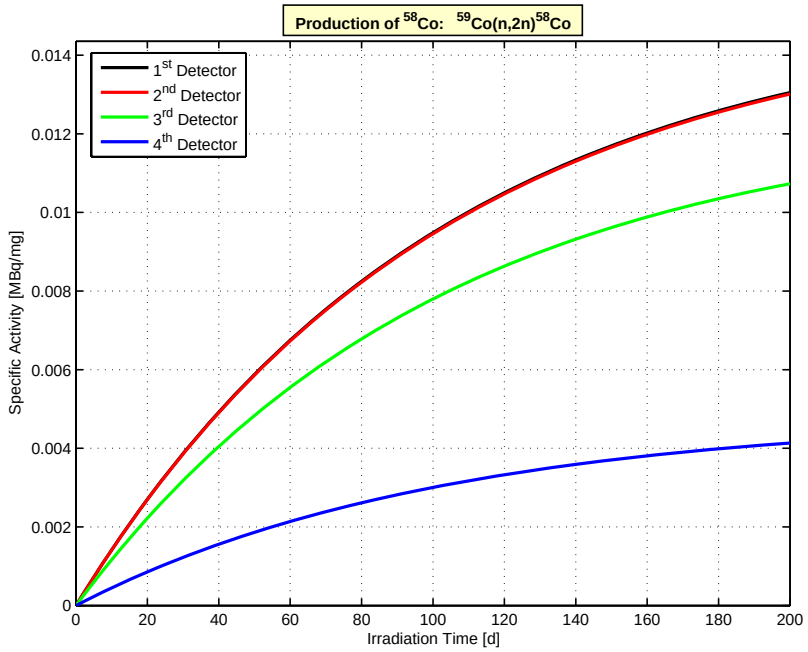

Figure 41. ^{58}Co activity as a function of the irradiation time

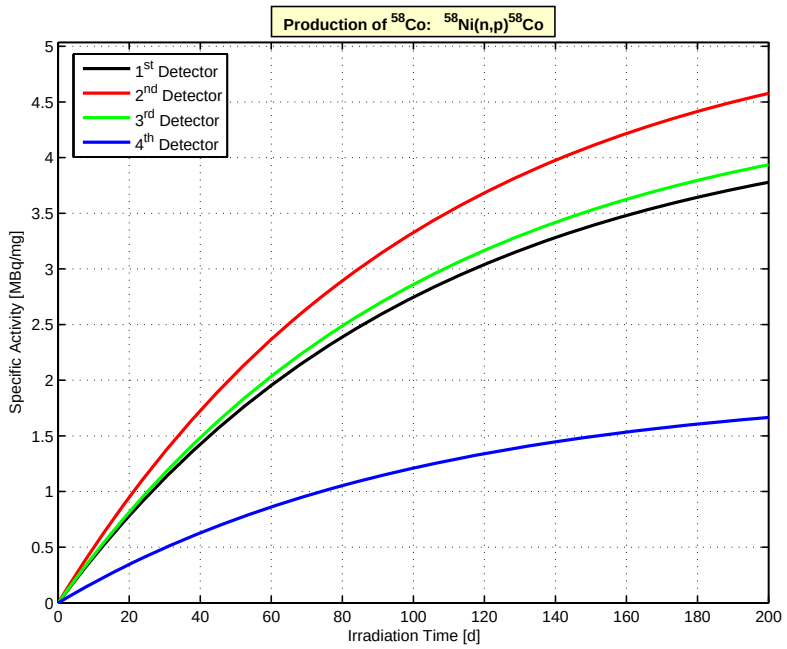

Figure 42. ^{58}Co activity as a function of the irradiation time

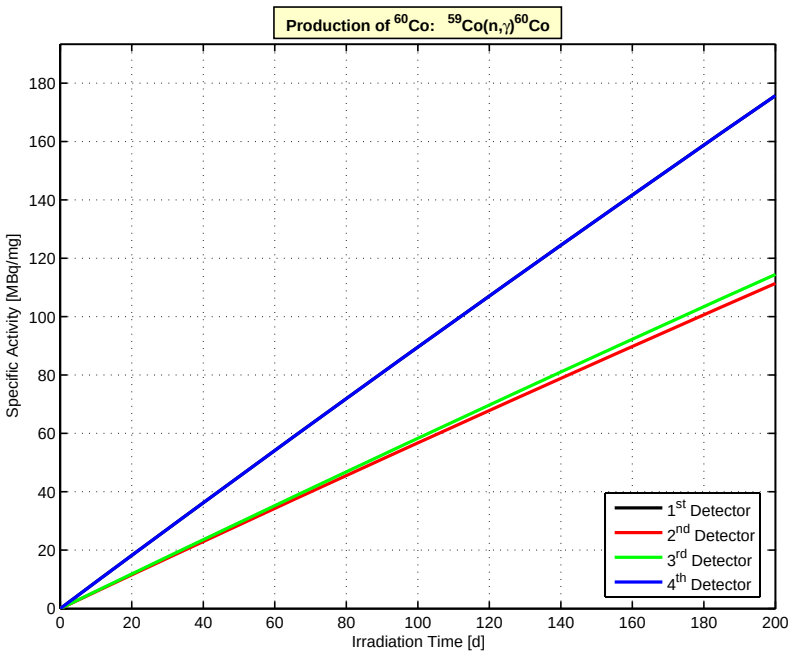

Figure 43. ^{60}Co activity as a function of the irradiation time

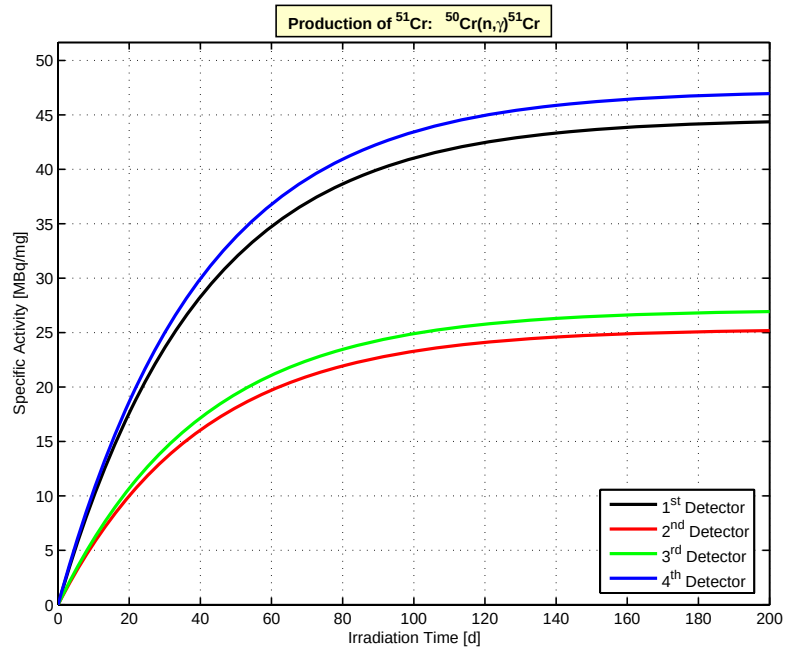

Figure 44. ^{51}Cr activity as a function of the irradiation time

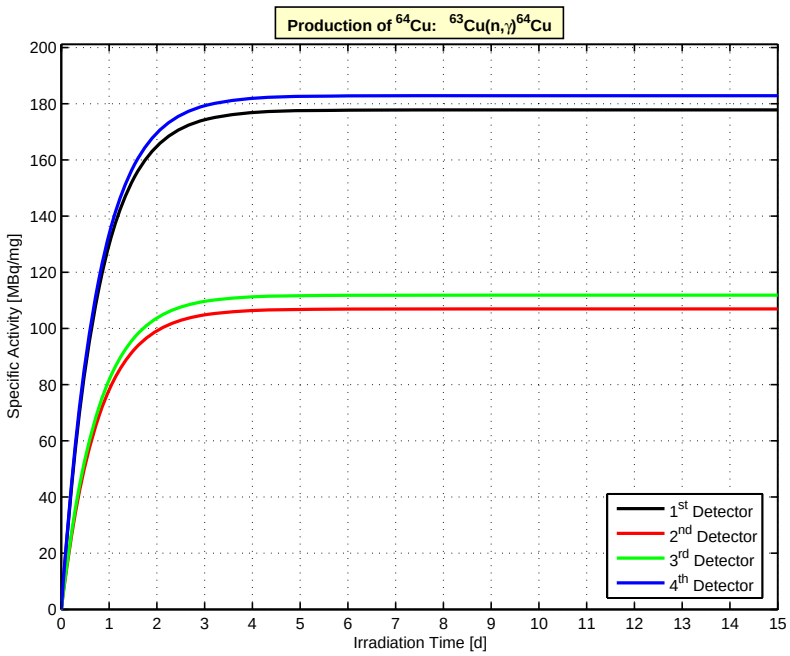

Figure 45. ^{64}Cu activity as a function of the irradiation time

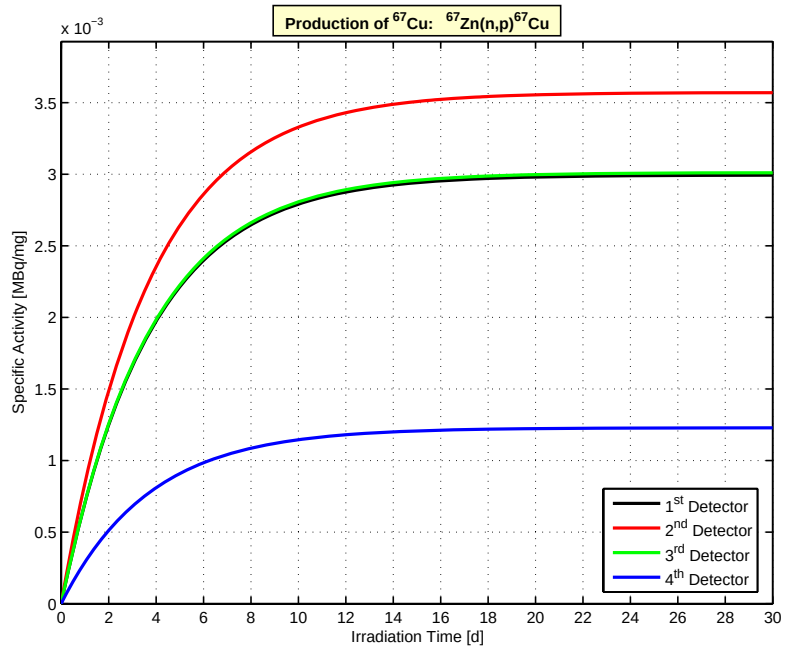

Figure 46. ^{67}Cu activity as a function of the irradiation time

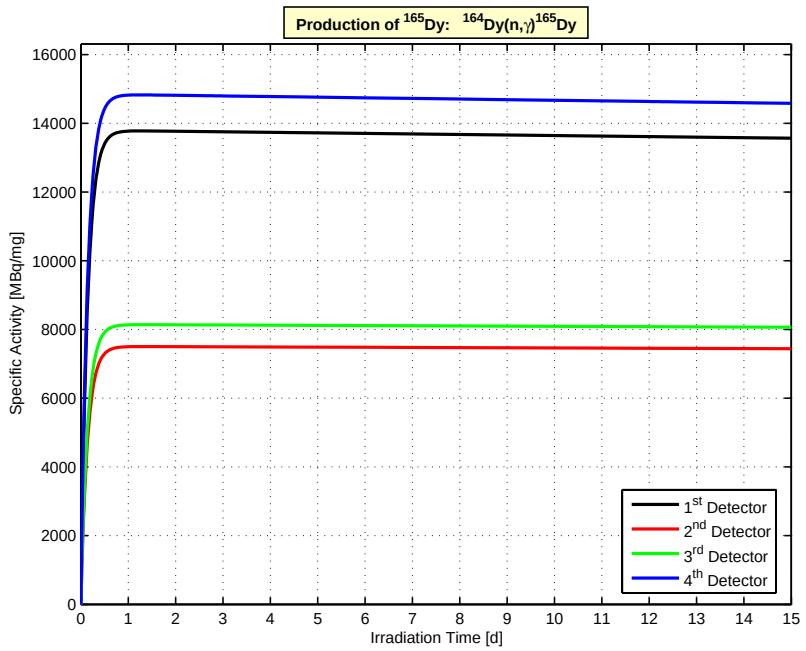

Figure 47. ^{165}Dy activity as a function of the irradiation time

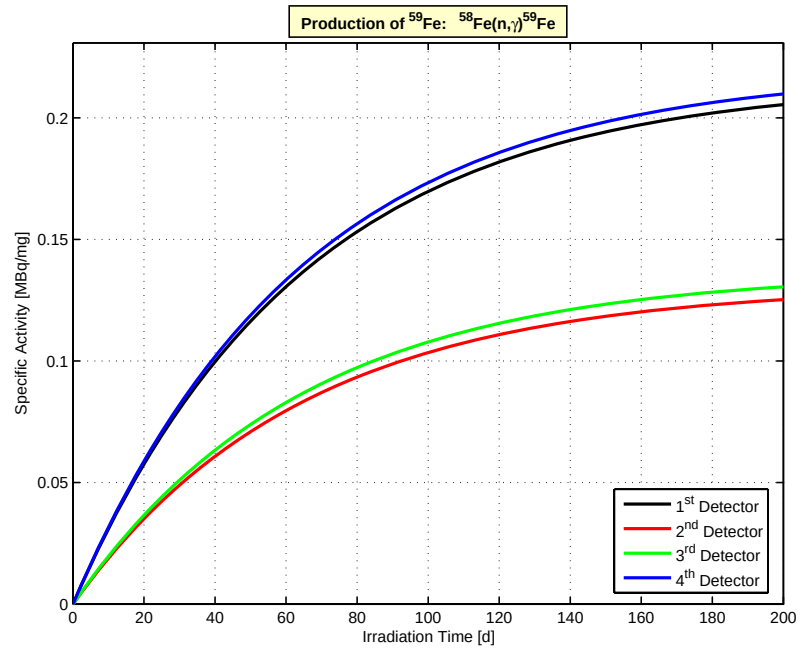

Figure 48. ^{59}Fe activity as a function of the irradiation time

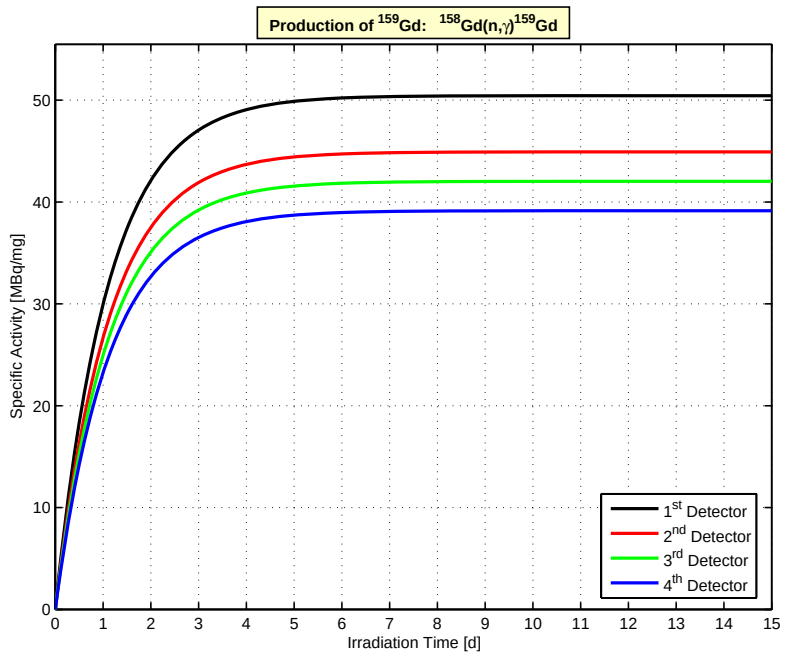

Figure 49. ^{159}Gd activity as a function of the irradiation time

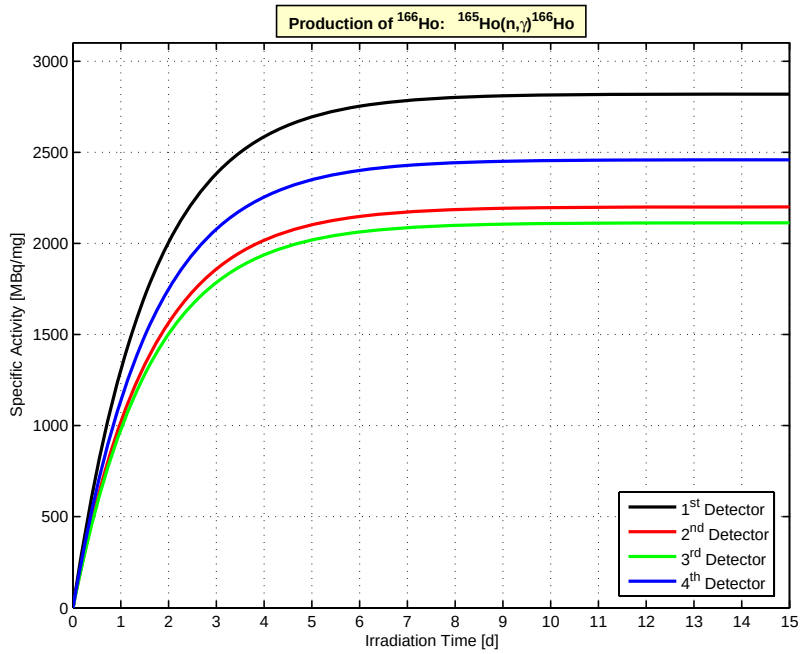

Figure 50. ^{166}Ho activity as a function of the irradiation time

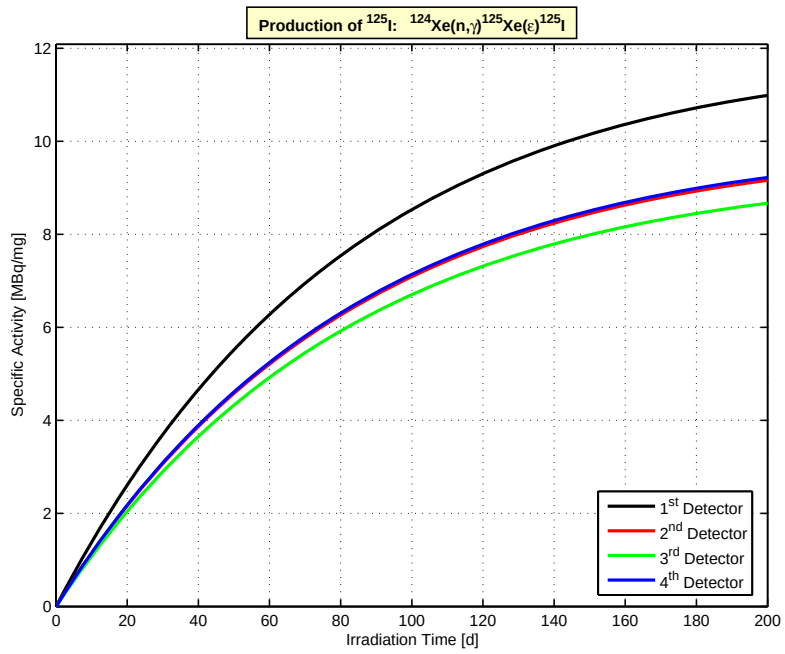

Figure 51. ^{125}I activity a as function of the irradiation time

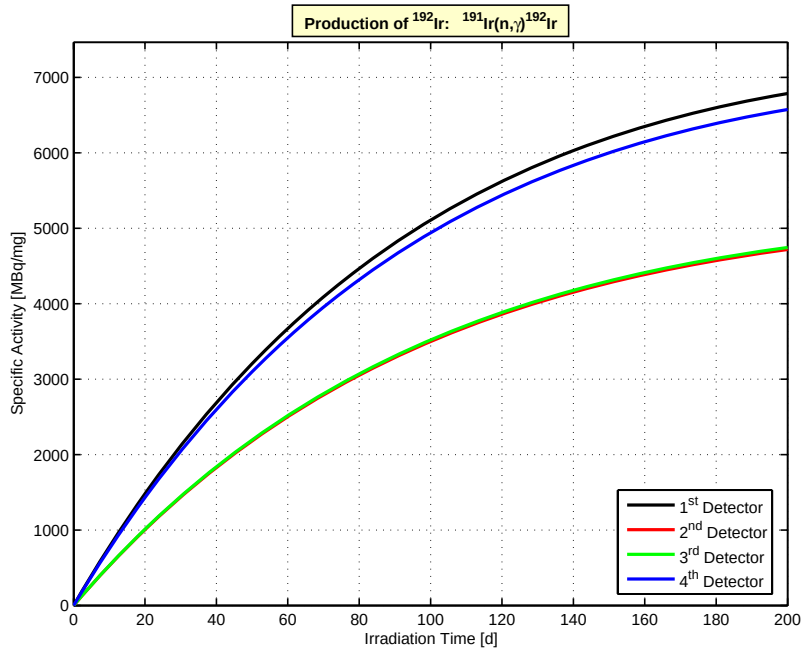

Figure 52. ^{192}Ir activity as a function of the irradiation time

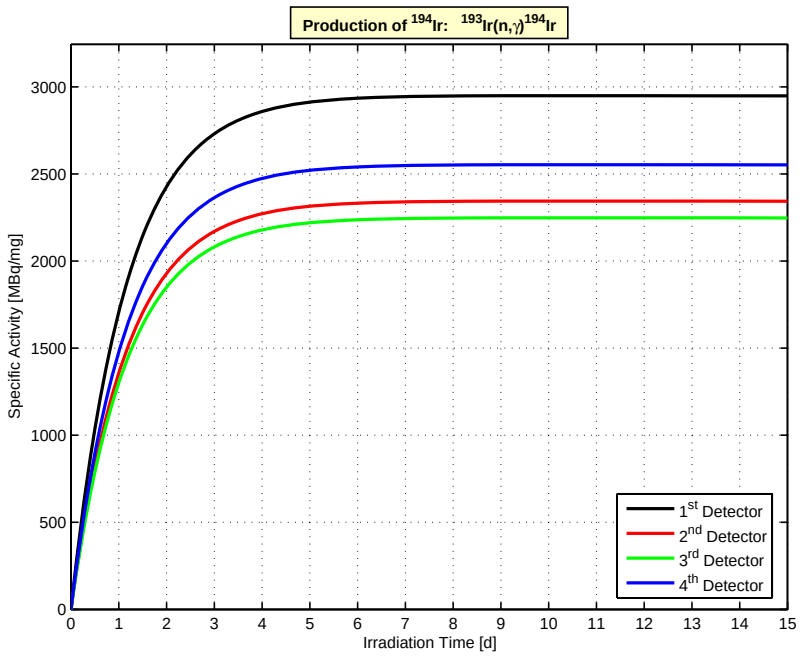

Figure 53. ^{194}Ir activity as a function of the irradiation time

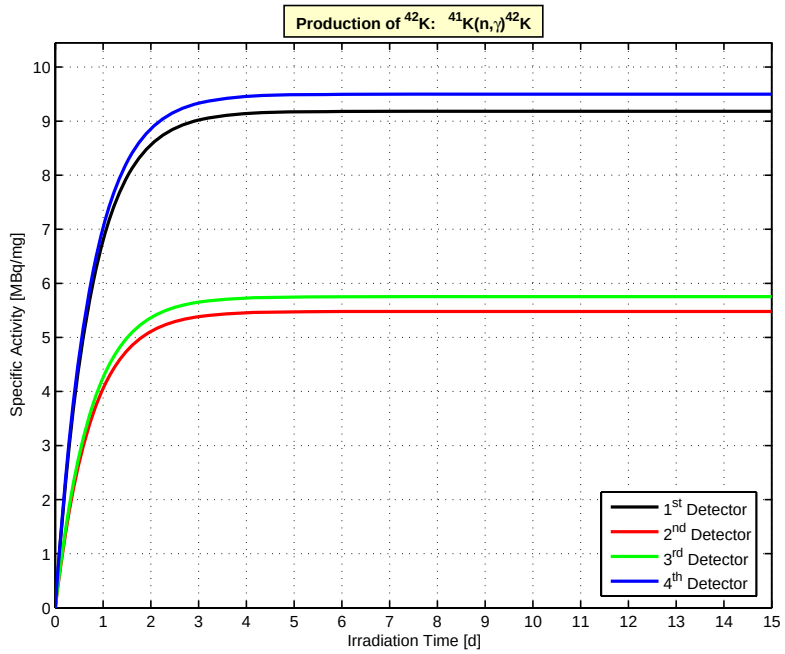

Figure 54. ^{42}K activity as a function of the irradiation time

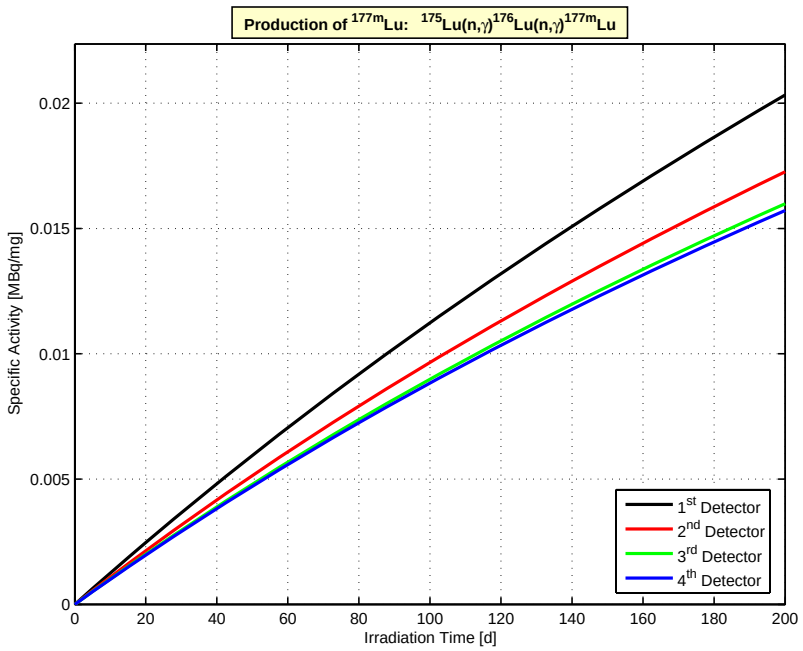

Figure 55. ^{177m}Lu activity as a function of the irradiation time

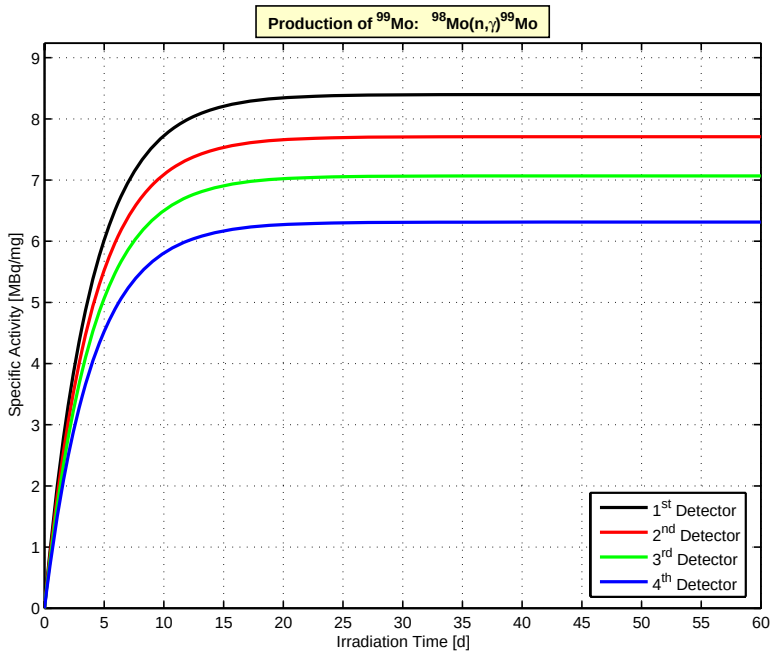

Figure 56. ^{99}Mo activity as a function of the irradiation time

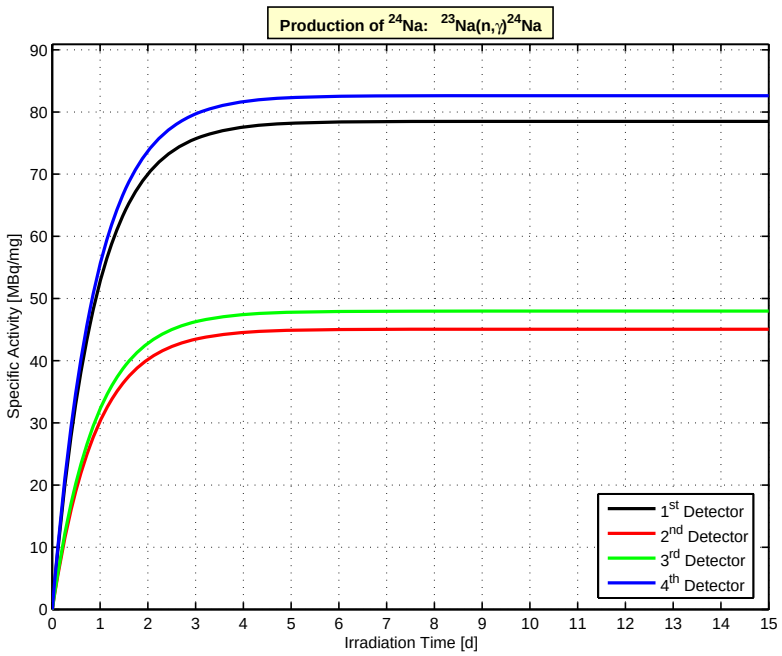

Figure 57. ^{24}Na activity as a function of the irradiation time

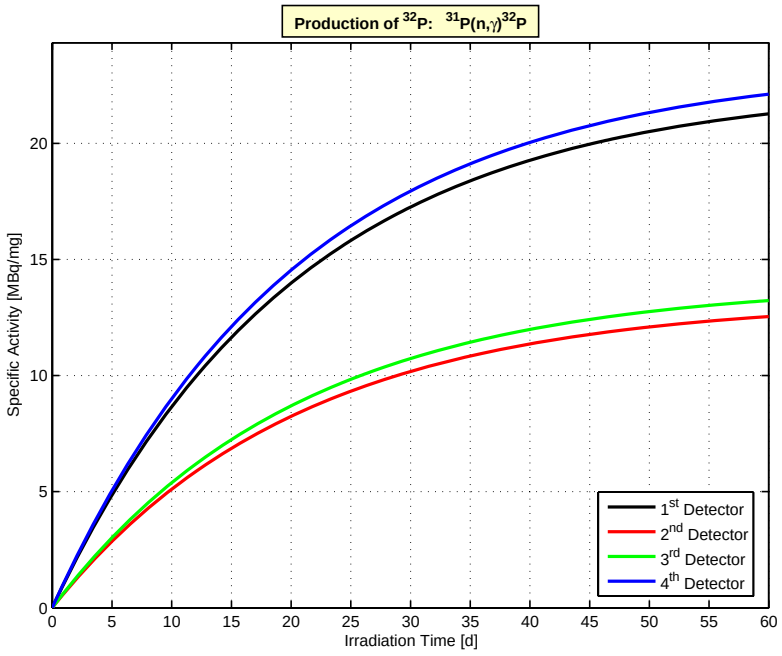

Figure 58. ^{32}P activity as a function of the irradiation time

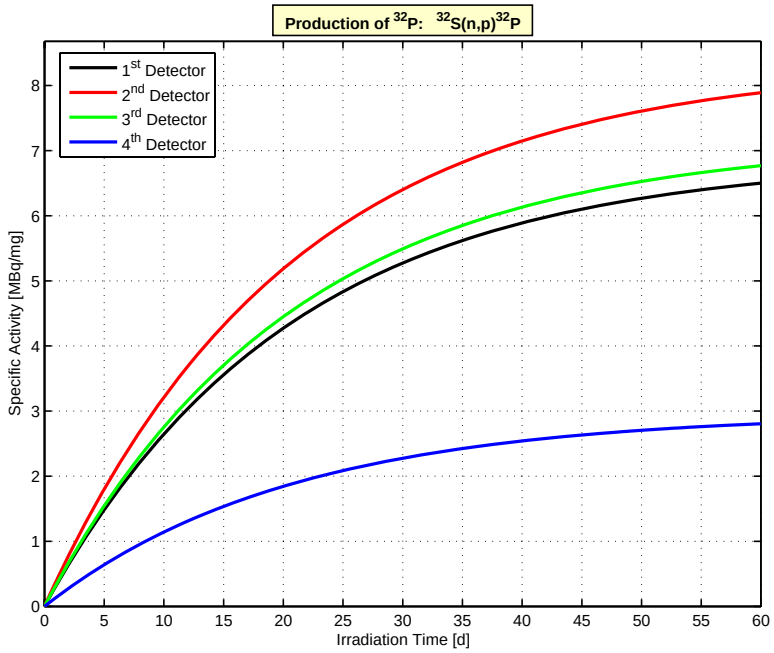

Figure 59. ^{32}P activity as a function of the irradiation time

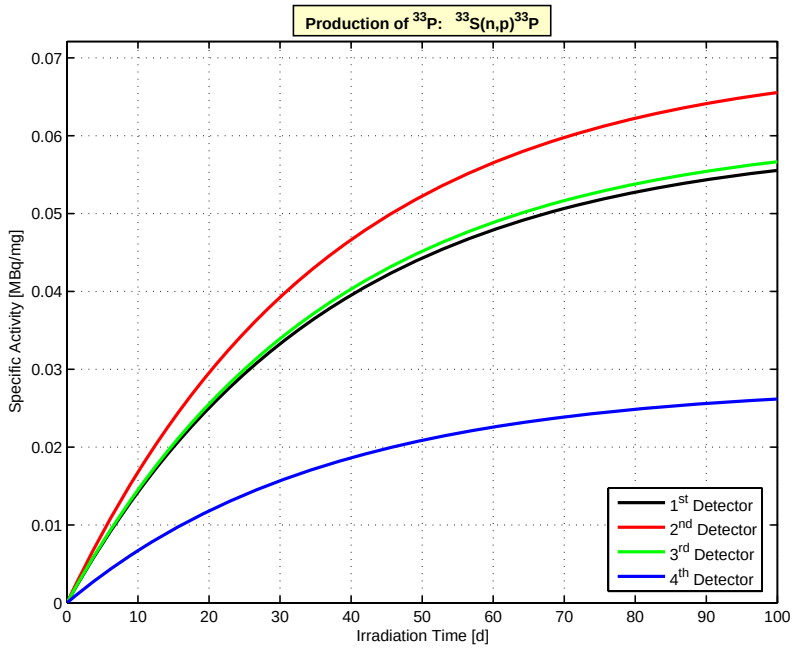

Figure 60. ^{33}P activity as a function of the irradiation time

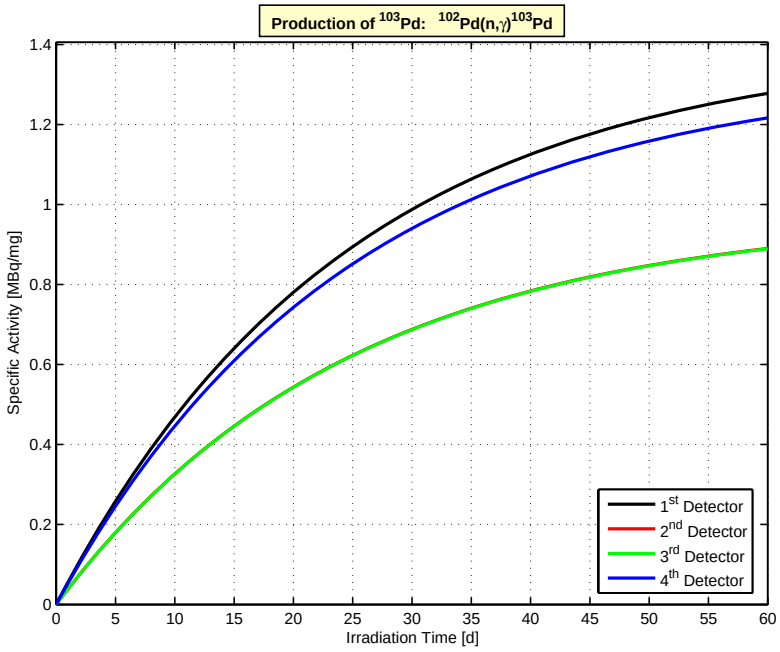

Figure 61. ^{103}Pd activity as a function of the irradiation time

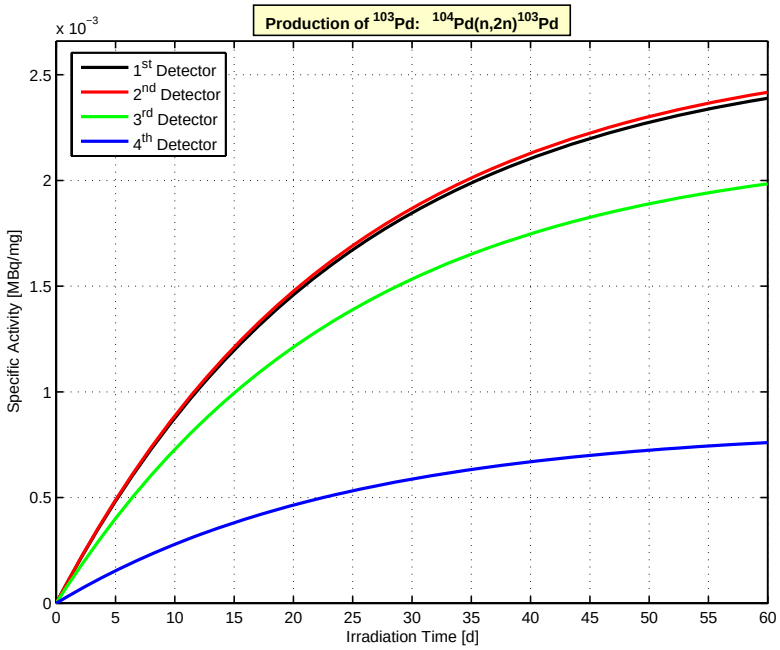

Figure 62. ^{103}Pd activity as a function of the irradiation time

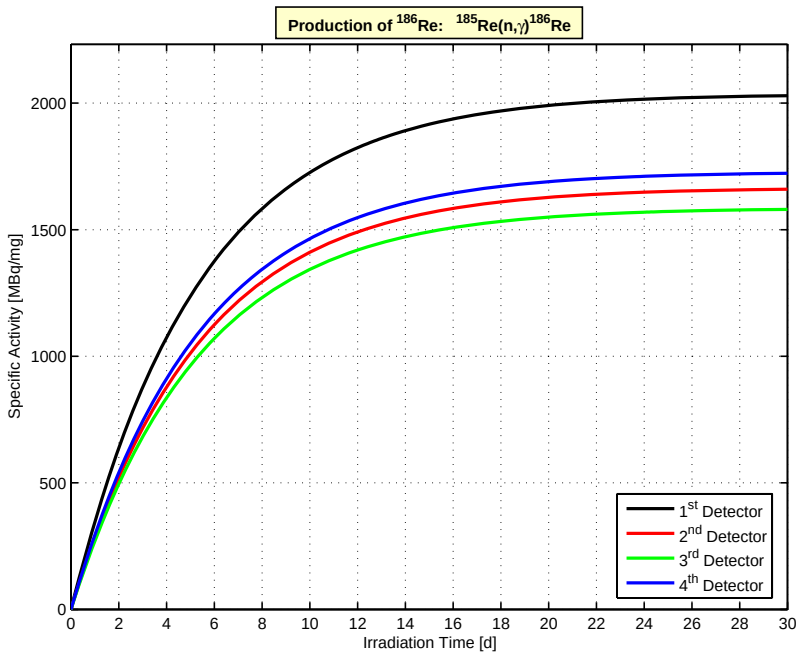

Figure 63. ^{186}Re activity as a function of the irradiation time

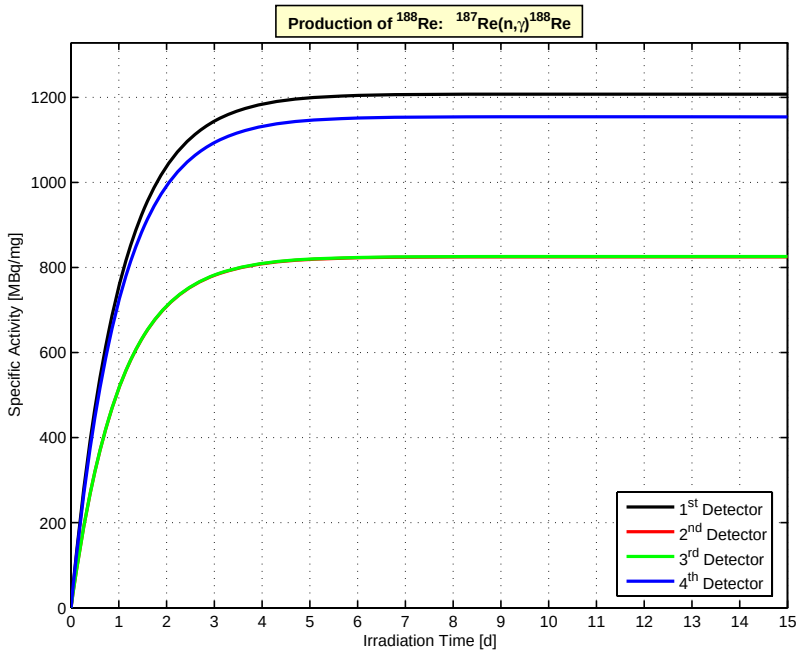

Figure 64. ^{188}Re activity as a function of the irradiation time

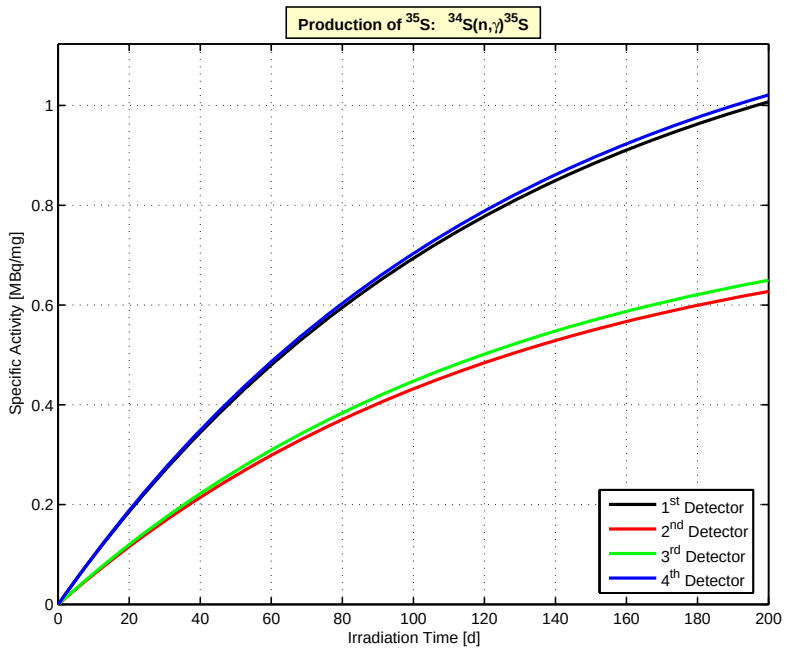

Figure 65. ^{35}S activity as a function of the irradiation time

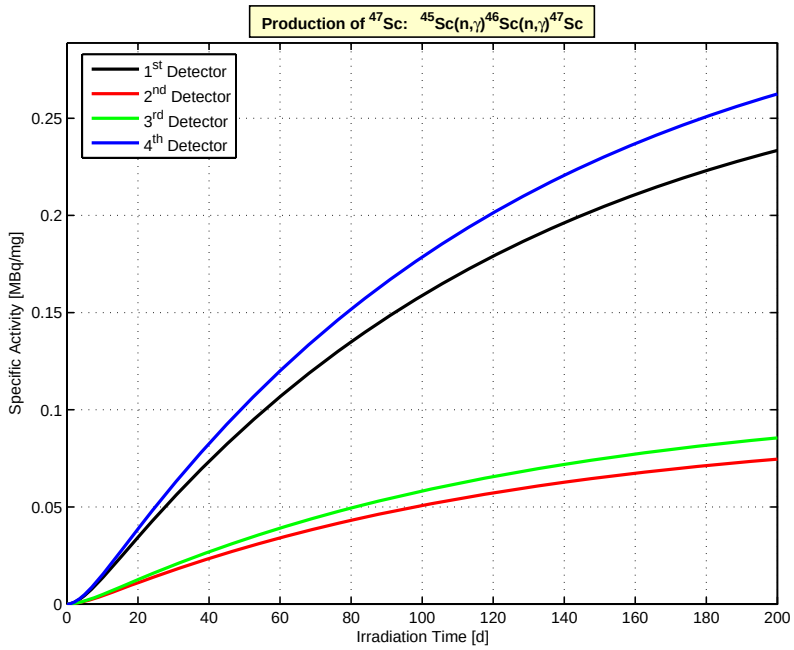

Figure 66. ^{47}Sc activity as a function of the irradiation time

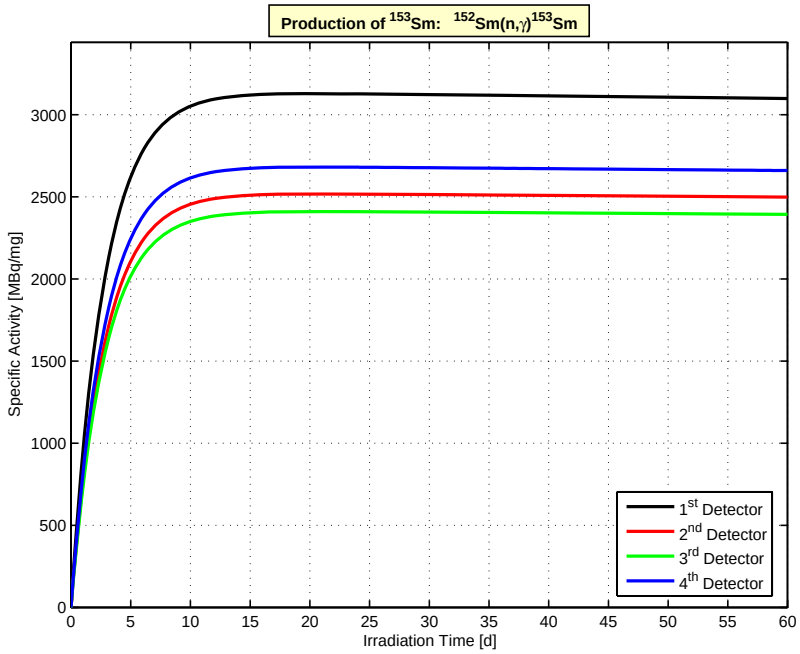

Figure 67. ^{153}Sm activity as a function of the irradiation time

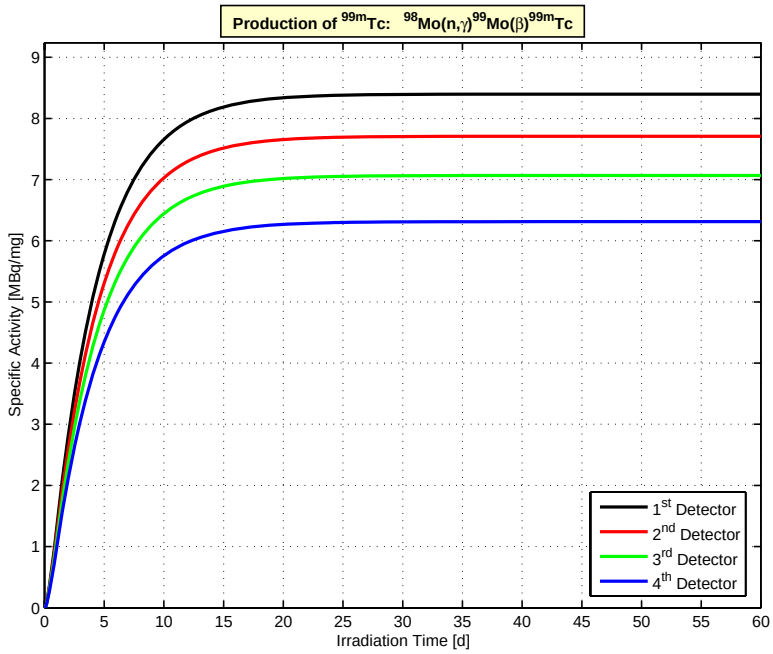

Figure 68. ^{99m}Tc activity as a function of the irradiation time

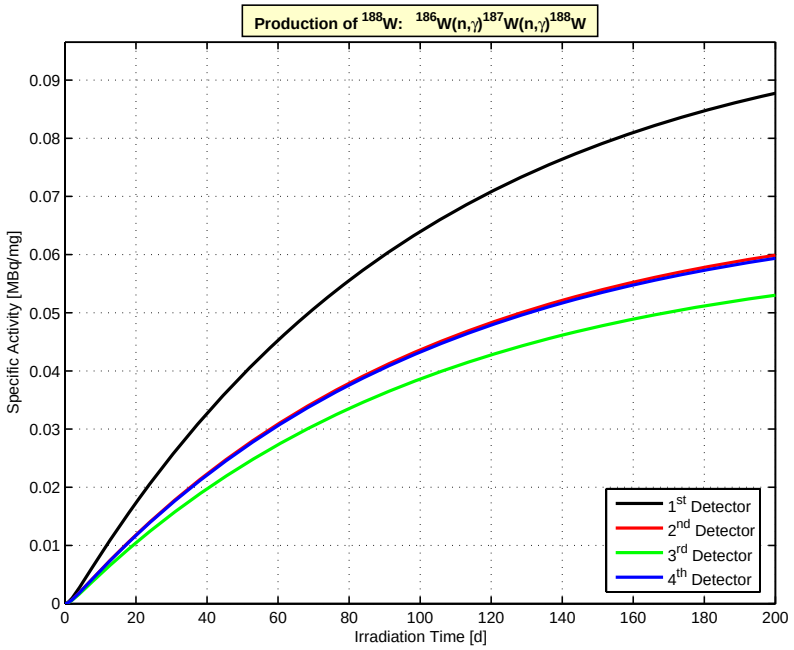

Figure 69. ^{188}W activity as a function of the irradiation time

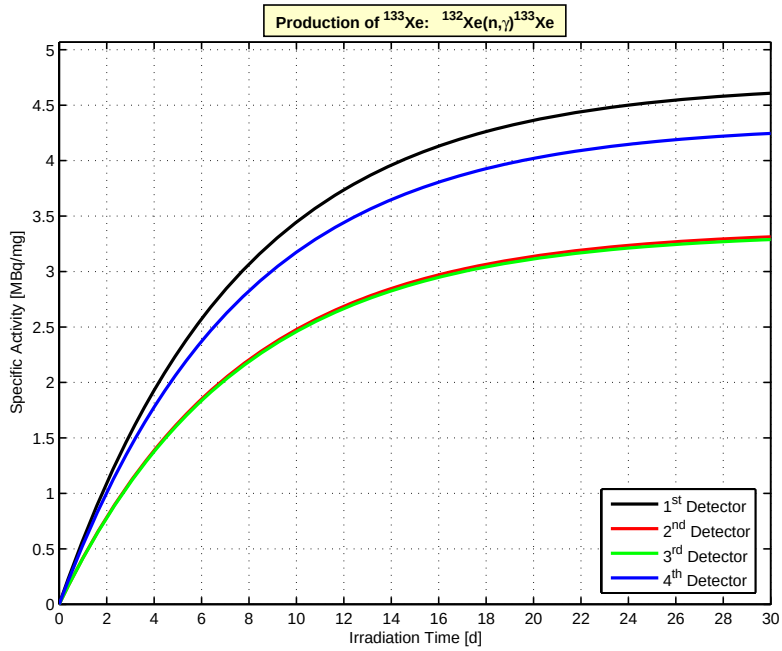

Figure 70. ^{133}Xe activity as a function of the irradiation time

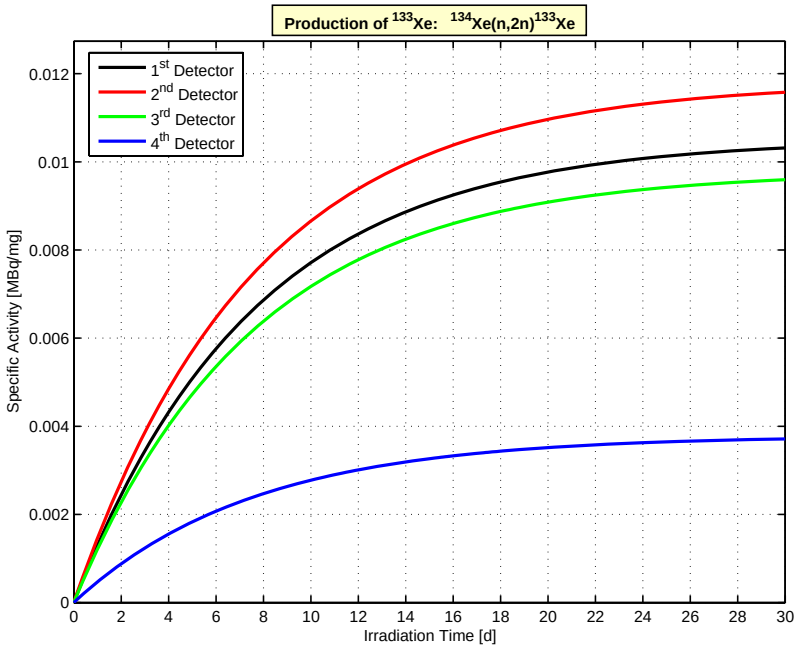

Figure 71. ^{133}Xe activity as a function of the irradiation time

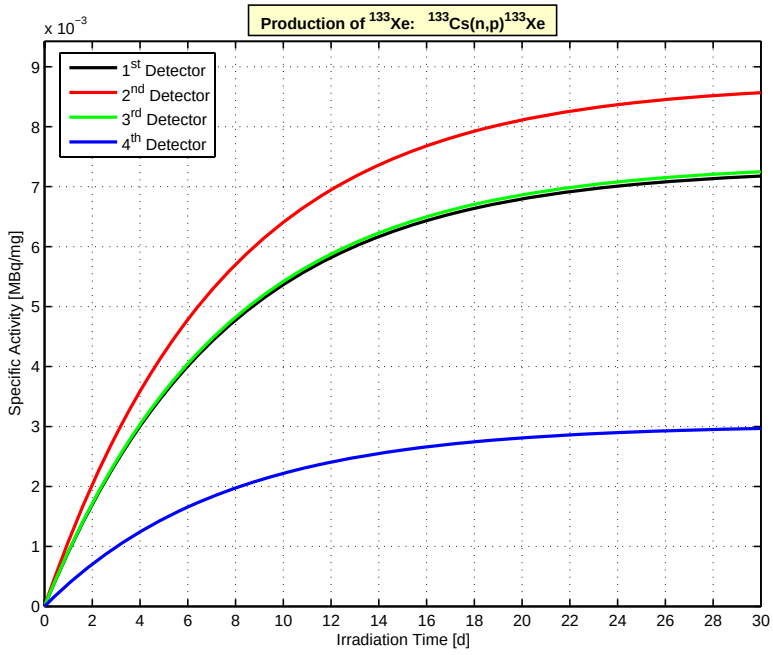

Figure 72. ^{133}Xe activity as a function of the irradiation time

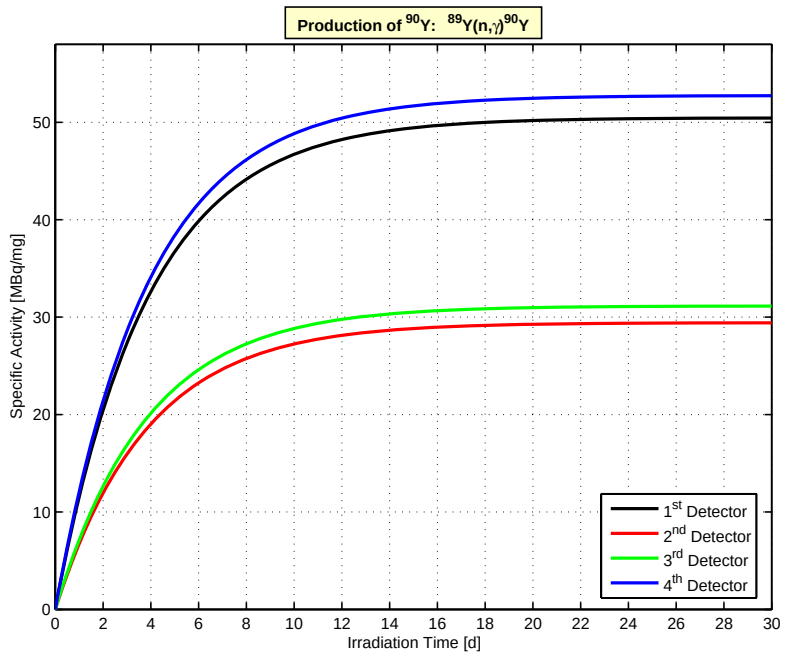

Figure 73. ^{90}Y activity as a function of the irradiation time

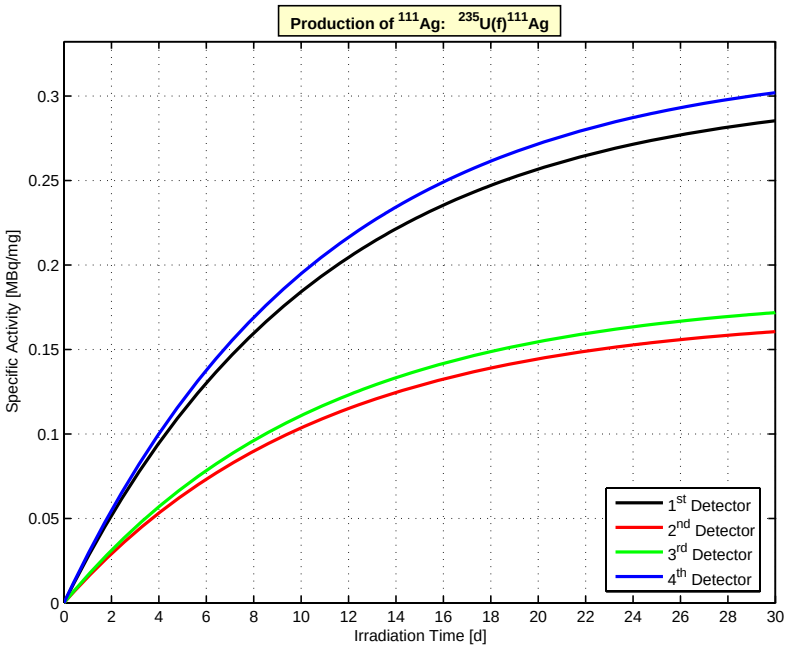

Figure 74. ^{111}Ag activity as a function of the irradiation time

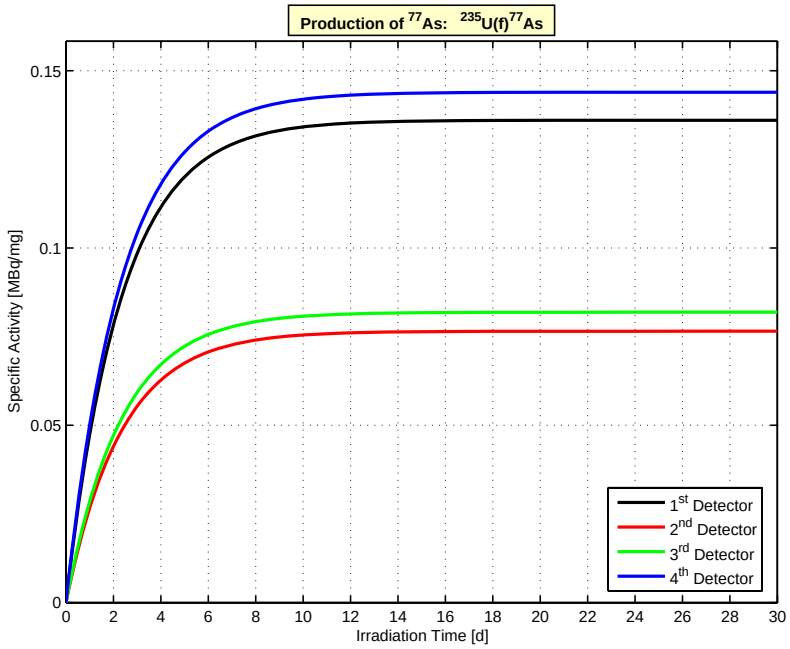

Figure 75. ^{77}As activity as a function of the irradiation time

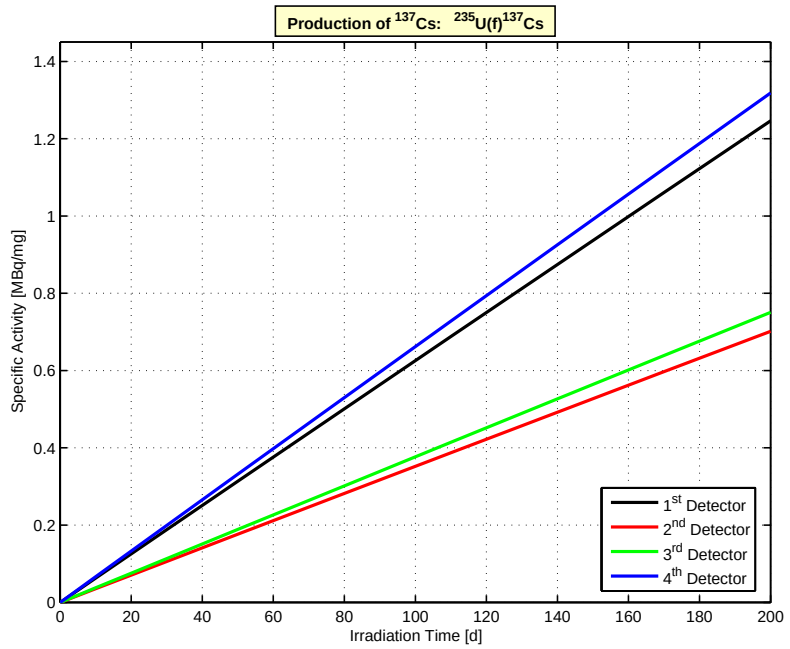

Figure 76. ^{137}Cs activity as a function of the irradiation time

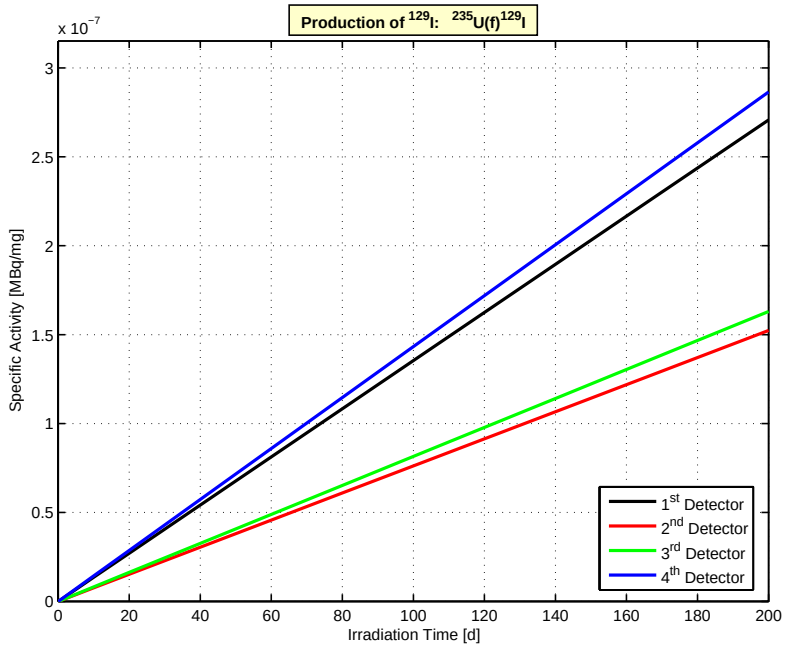

Figure 77. ^{129}I activity as a function of the irradiation time

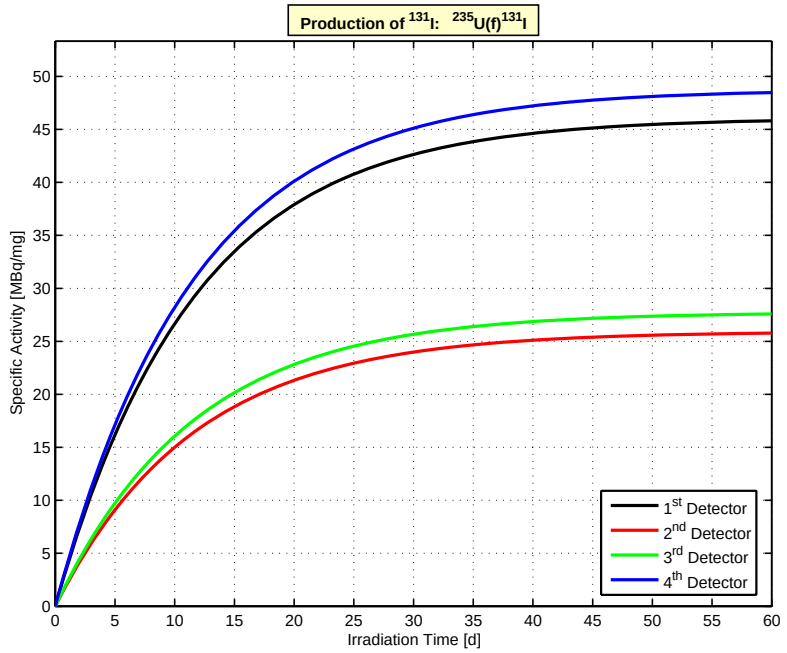

Figure 78. ^{131}I activity as a function of the irradiation time

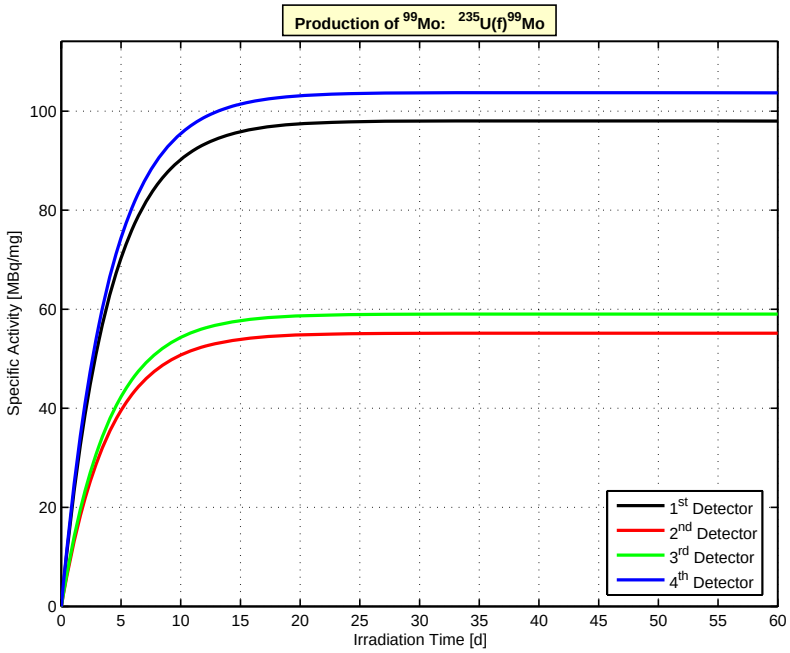

Figure 79. ^{99}Mo activity as a function of the irradiation time

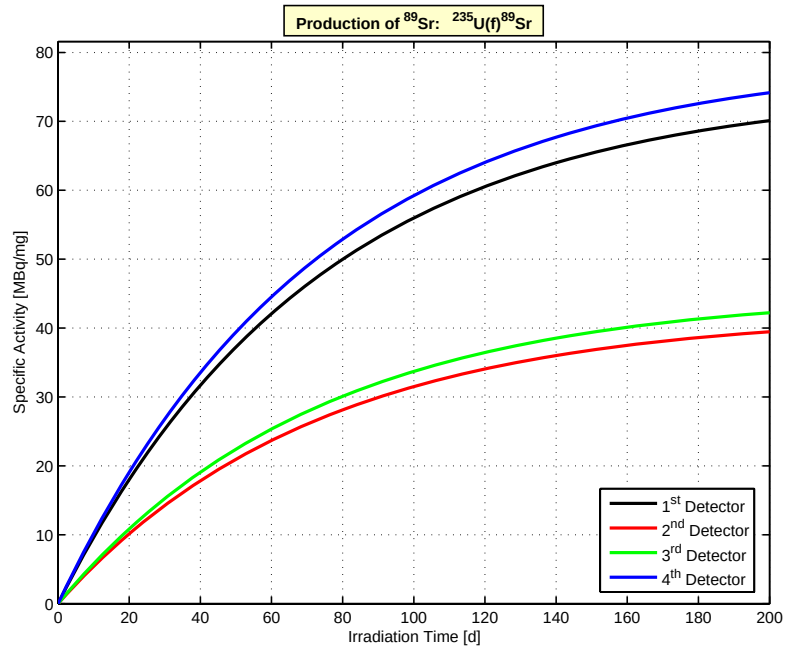

Figure 80. ^{89}Sr activity as a function of the irradiation time

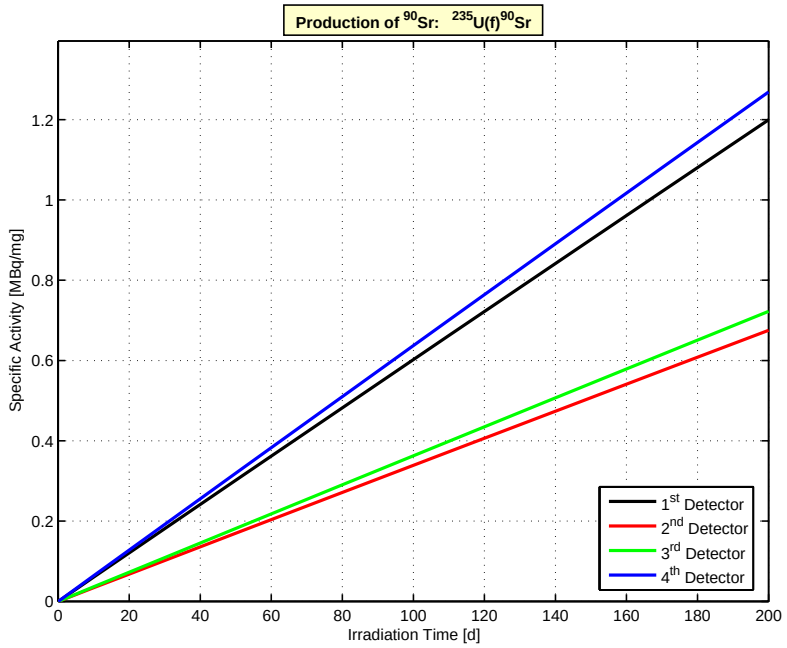

Figure 81. ^{90}Sr activity as a function of the irradiation time

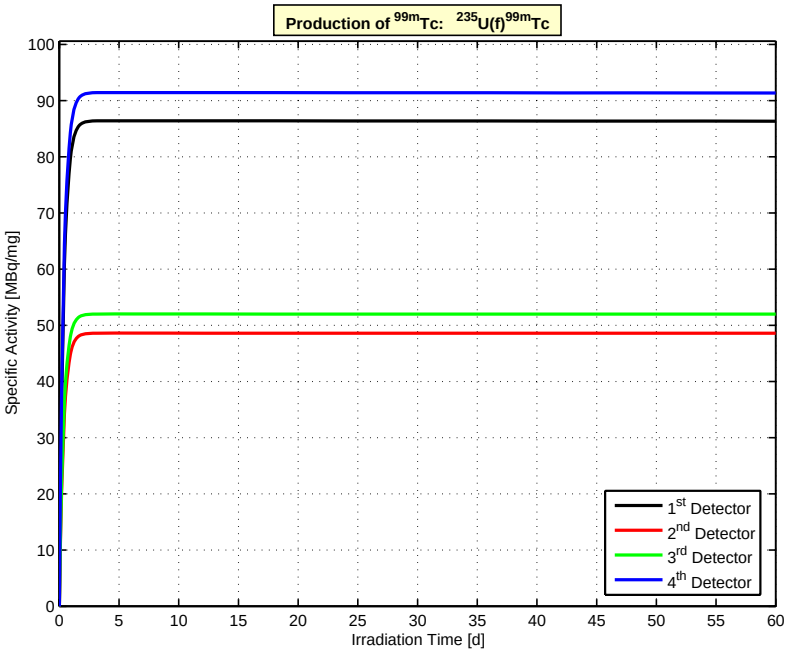

Figure 82. ^{99m}Tc activity as a function of the irradiation time

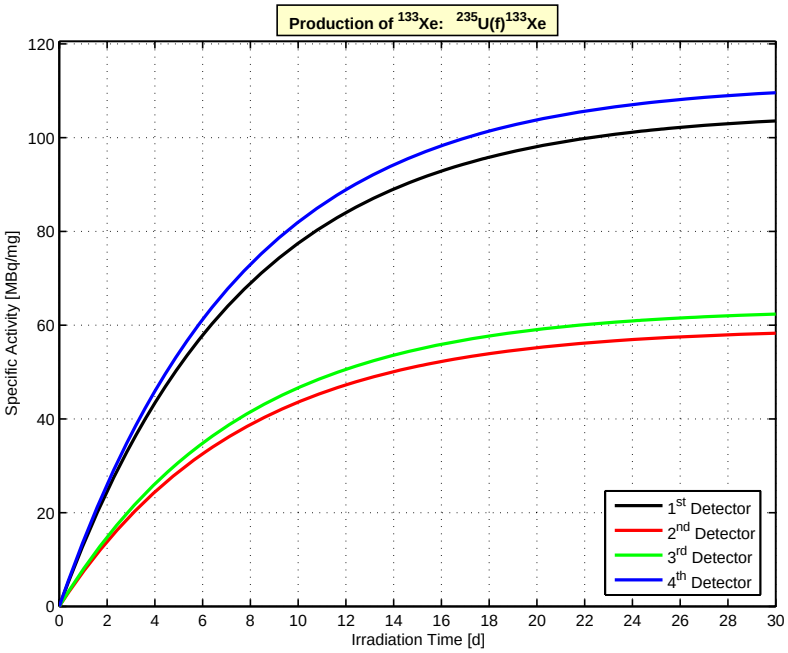

Figure 83. ^{133}Xe activity as a function of the irradiation time

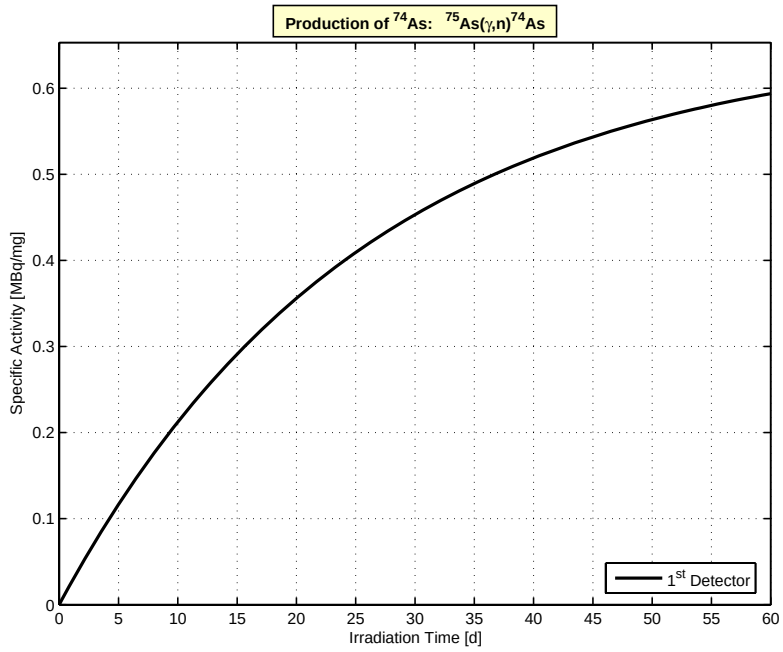

Figure 84. ^{74}As activity as a function of the irradiation time

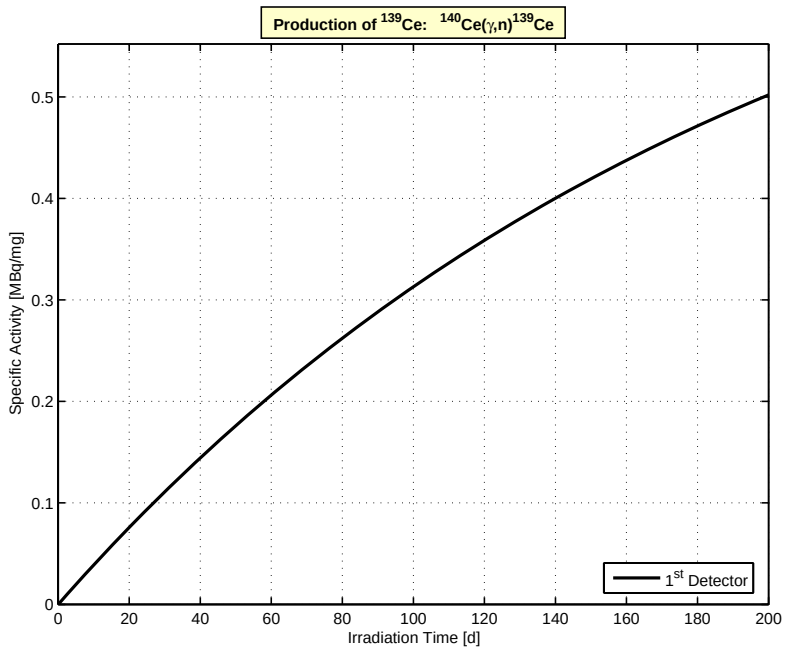

Figure 85. ^{139}Cs activity as a function of the irradiation time

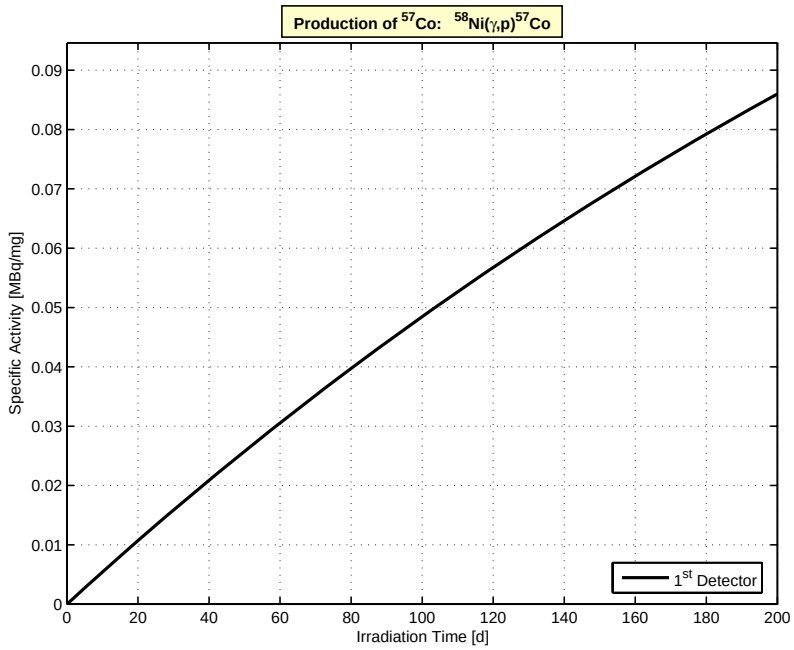

Figure 86. ^{57}Co activity as a function of the irradiation time

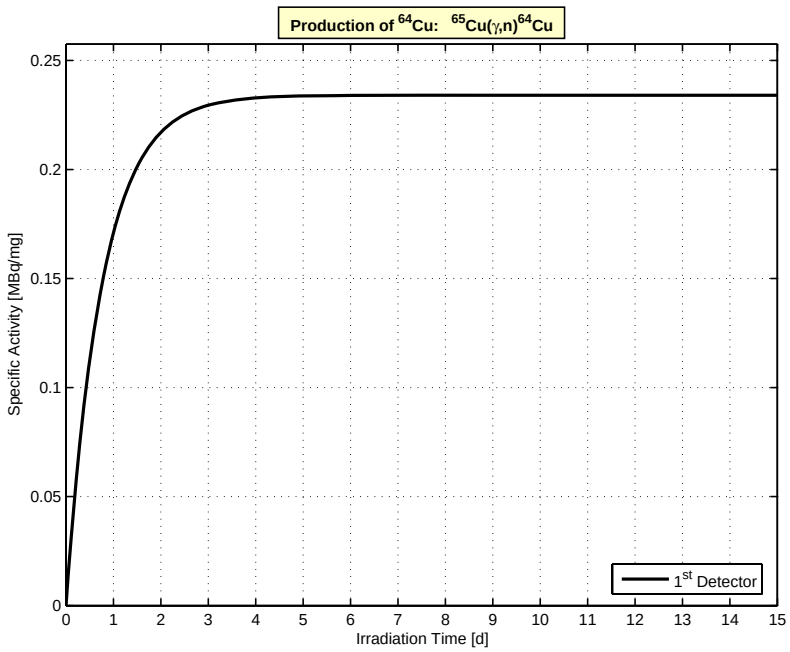

Figure 87. ^{64}Cu activity as a function of the irradiation time

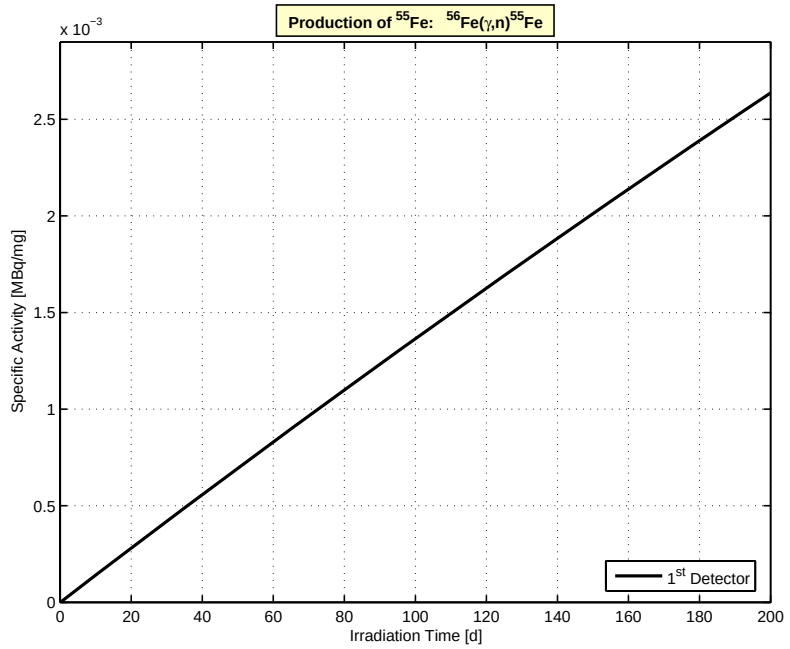

Figure 88. ^{55}Fe activity as a function of the irradiation time

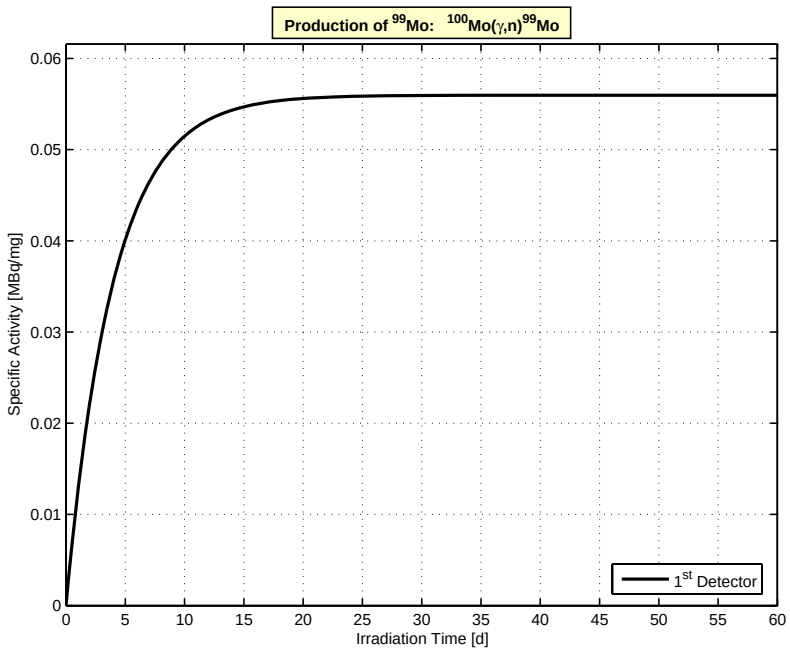

Figure 89. ^{99}Mo activity as a function of the irradiation time

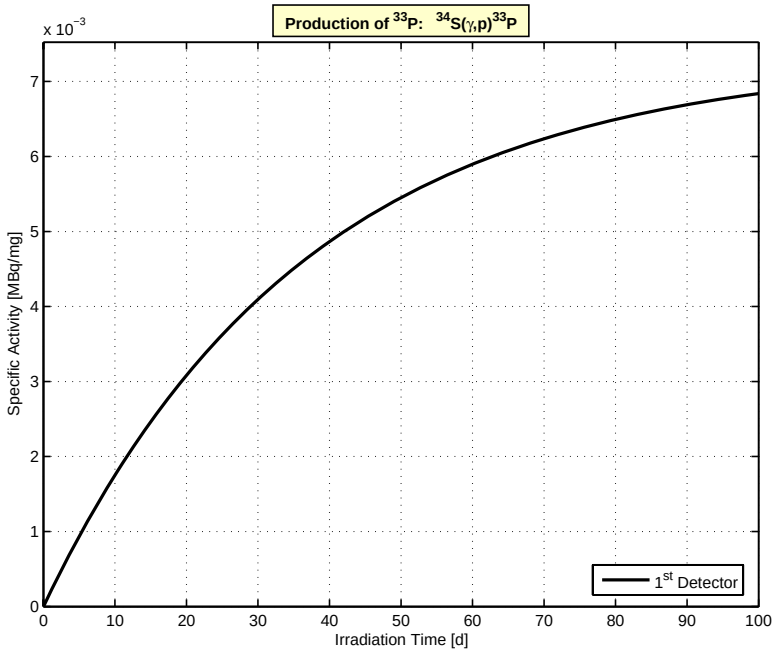

Figure 90. ^{33}P activity as a function of the irradiation time

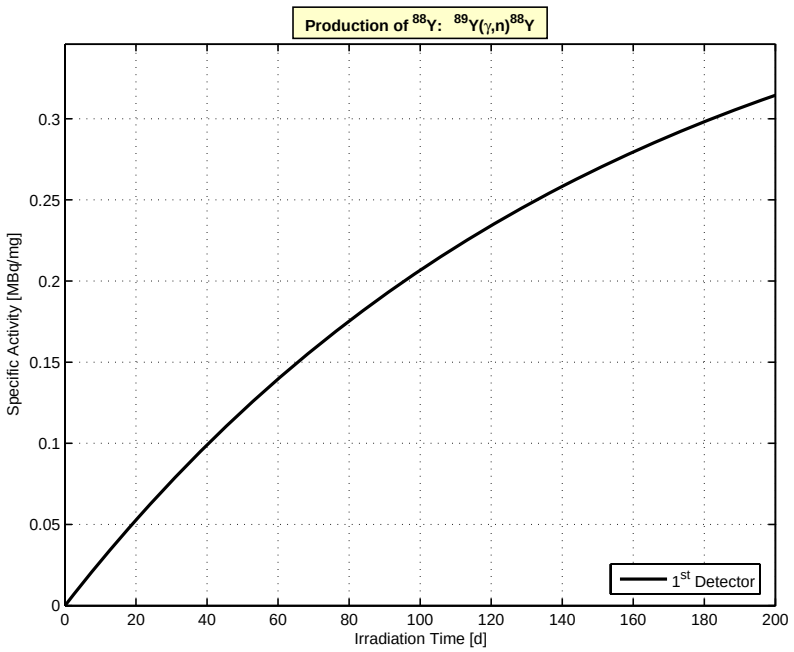

Figure 91. ^{88}Y activity as a function of the irradiation time

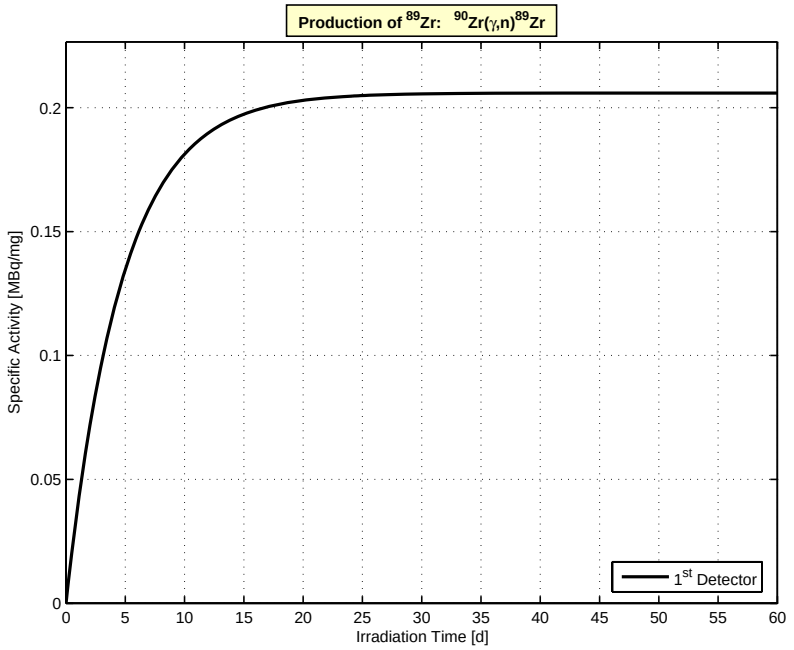

Figure 92. ^{89}Zr activity as a function of the irradiation time

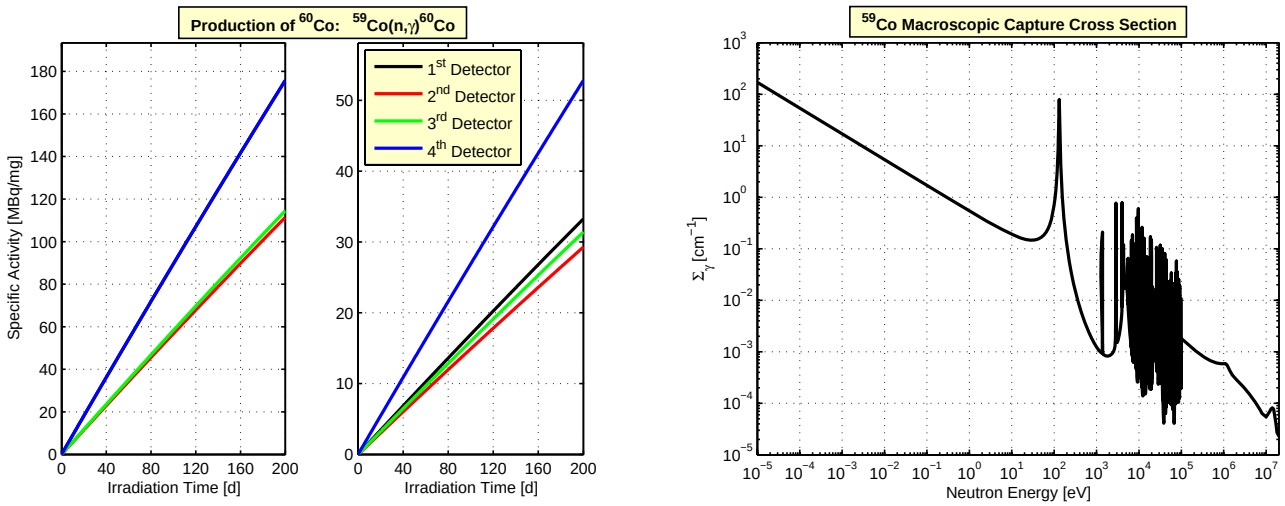

Figure 93. ^{60}Co activity as a function of the irradiation time without and with self shielding, left and right subplots, respectively; ^{59}Co macroscopic capture cross section; ^{60}Co represents 100% of the parent material

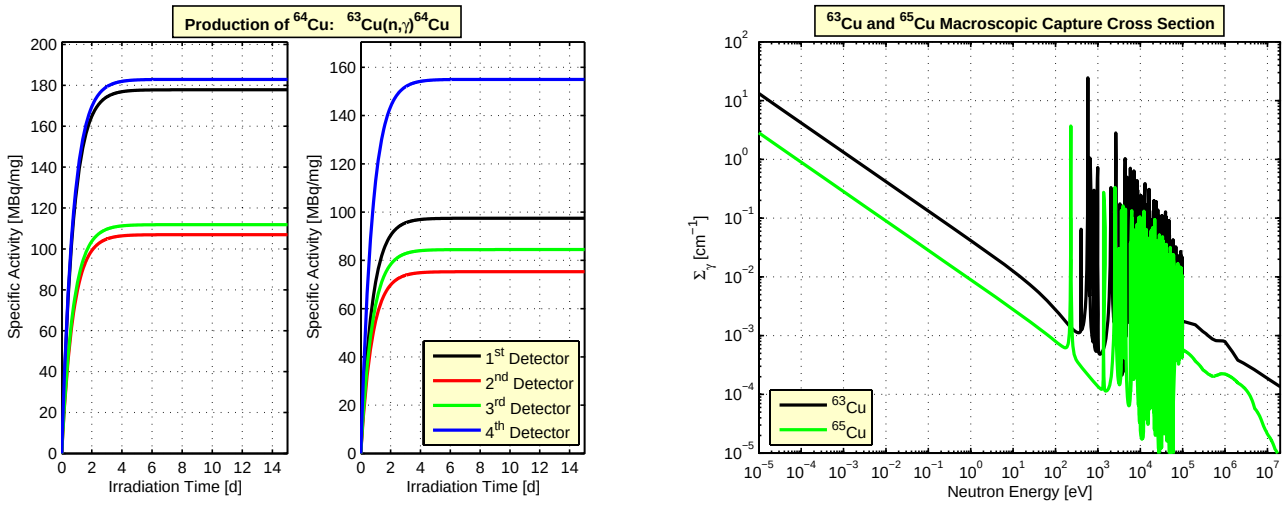

Figure 94. ^{64}Cu activity as a function of the irradiation time without and with self shielding, left and right subplots, respectively; ^{63}Cu macroscopic capture cross section; ^{63}Cu and ^{65}Cu represent 69.17 and 30.83% of the parent material, respectively

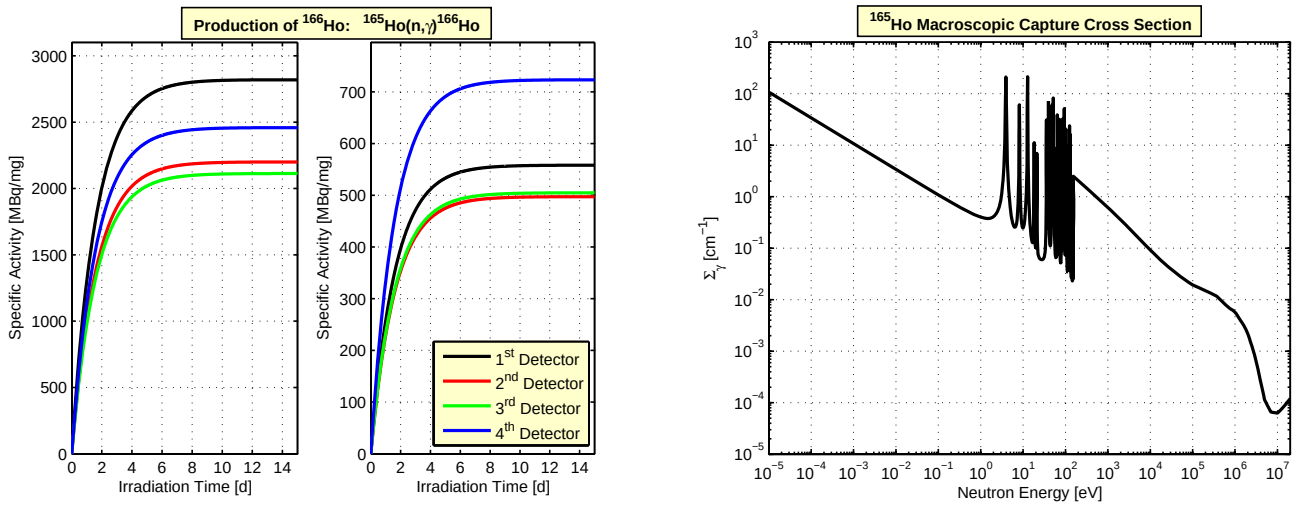

Figure 95. ^{166}Ho activity as a function of the irradiation time without and with self shielding, left and right subplots, respectively; ^{165}Ho macroscopic capture cross section; ^{165}Ho represents 100% of the parent material

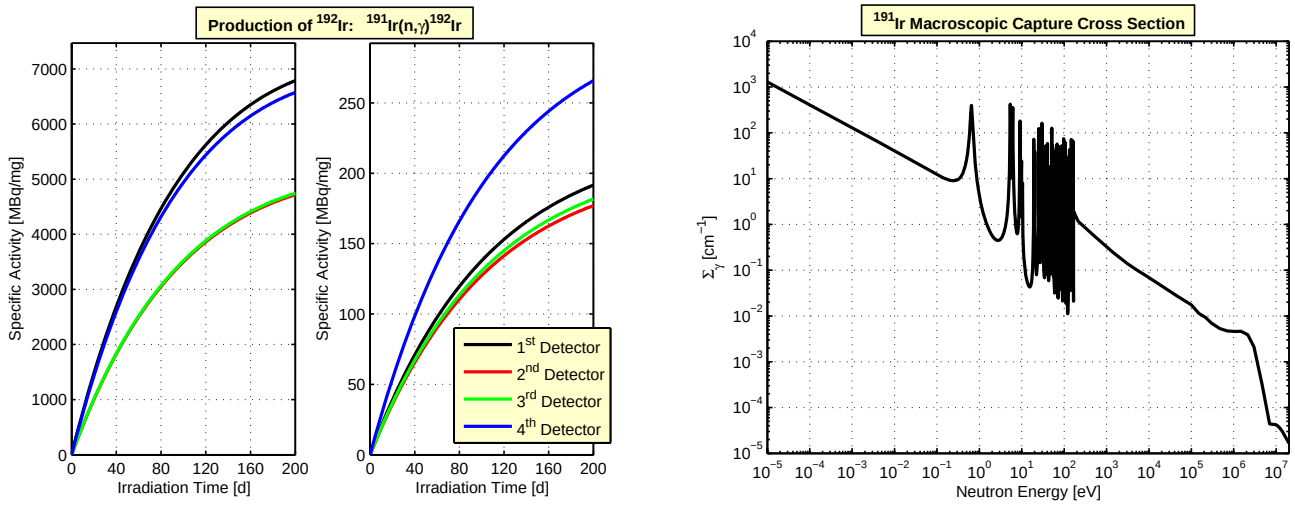

Figure 96. ^{192}Ir activity as a function of the irradiation time without and with self shielding, left and right subplots, respectively; ^{191}Ir macroscopic capture cross section; ^{191}Ir and ^{193}Ir represent 37.3 and 62.7% of the parent material, respectively

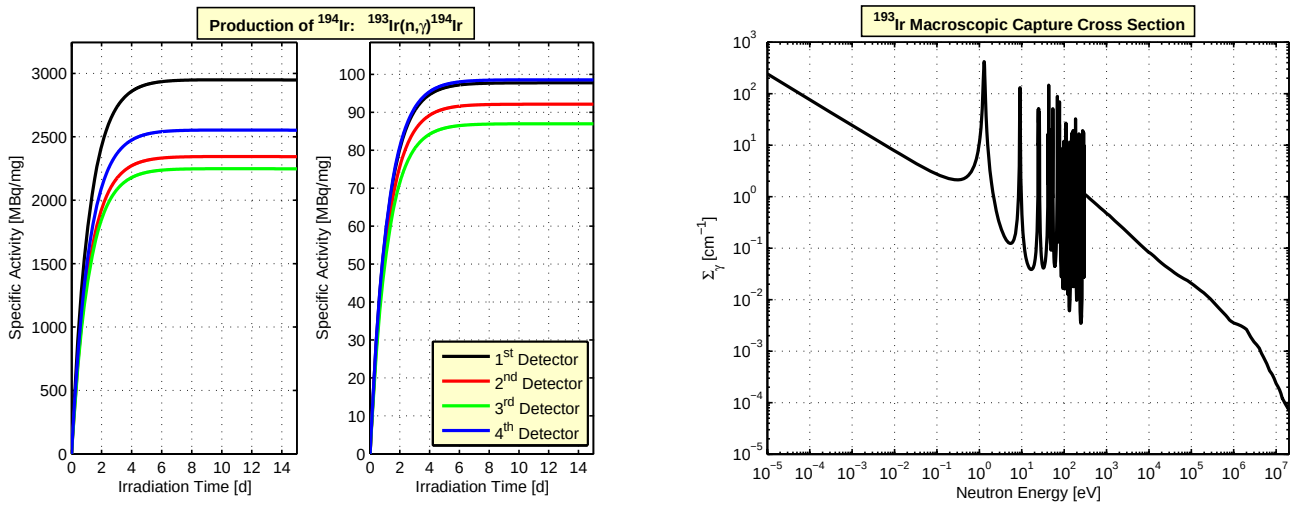

Figure 97. ^{194}Ir activity as a function of the irradiation time without and with self shielding, left and right subplots, respectively; ^{193}Ir macroscopic capture cross section; ^{191}Ir and ^{193}Ir represent 37.3 and 62.7% of the parent material, respectively

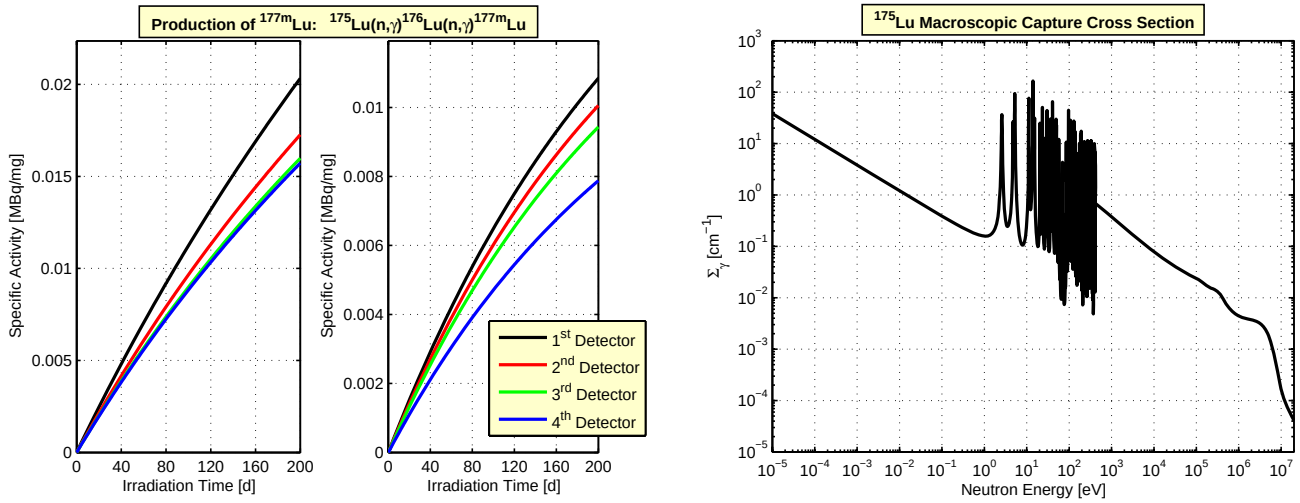

Figure 98. ^{177m}Lu activity as a function of the irradiation time without and with self shielding, left and right subplots, respectively; ^{175}Lu macroscopic capture cross section; ^{175}Lu represents 97.41% of the parent material

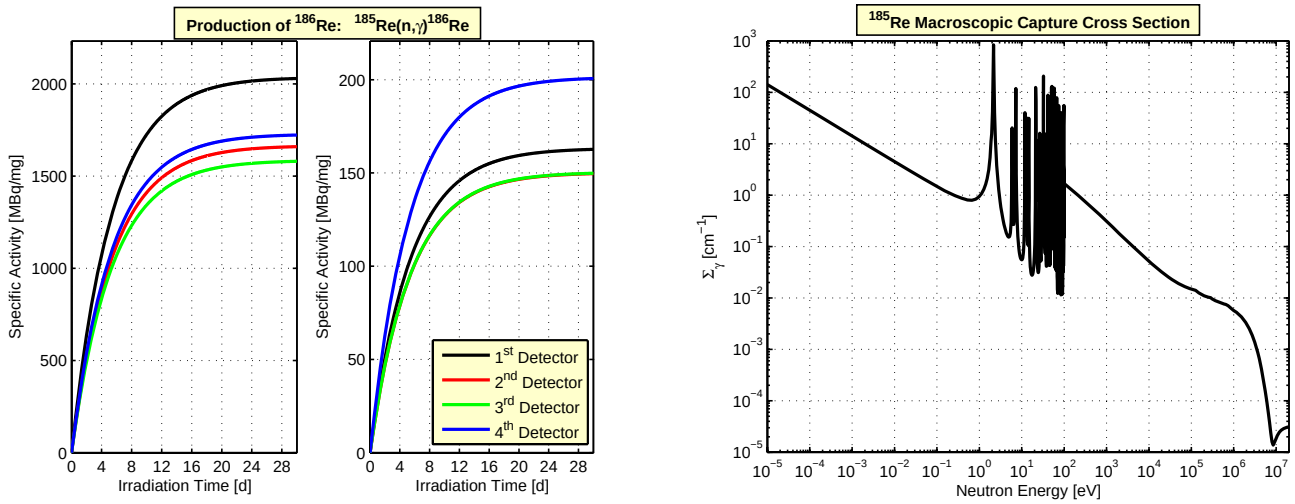

Figure 99. ^{186}Re activity as a function of the irradiation time without and with self shielding, left and right subplots, respectively; ^{185}Re macroscopic capture cross section; ^{185}Re and ^{187}Re represent 37.4 and 62.6% of the parent material, respectively

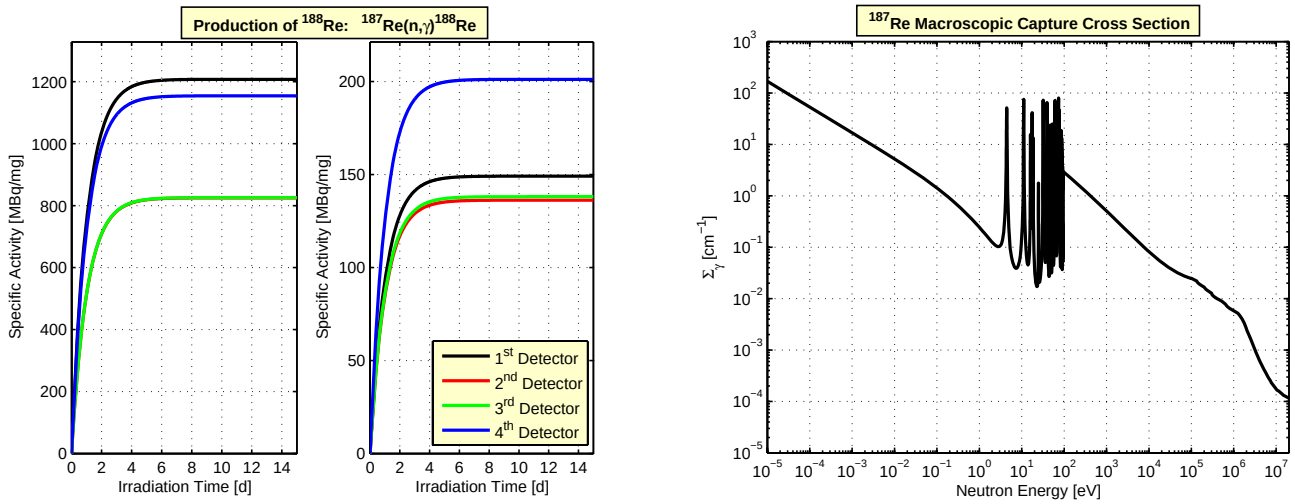

Figure 100. ^{188}Re activity as a function of the irradiation time without and with self shielding, left and right subplots, respectively; ^{187}Re macroscopic capture cross section; ^{185}Re and ^{187}Re represent 37.4 and 62.6% of the parent material, respectively

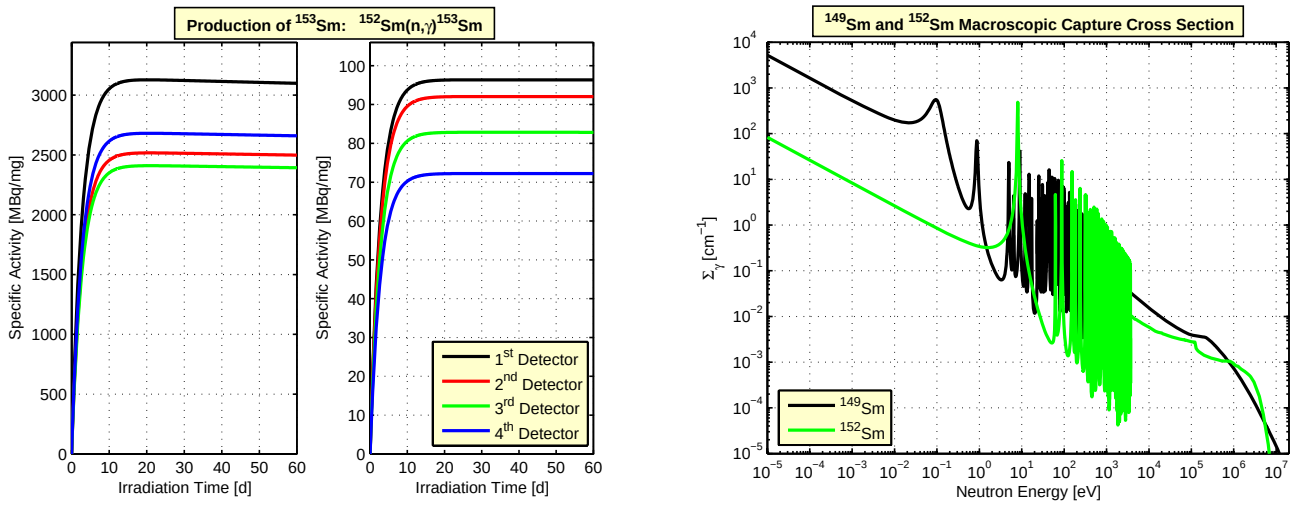

Figure 101. ^{153}Sm activity as a function of the irradiation time without and with self shielding, left and right subplots, respectively; ^{149}Sm and ^{152}Sm macroscopic capture cross section; ^{149}Sm and ^{152}Sm represent 21.4 and 42% of the parent material, respectively

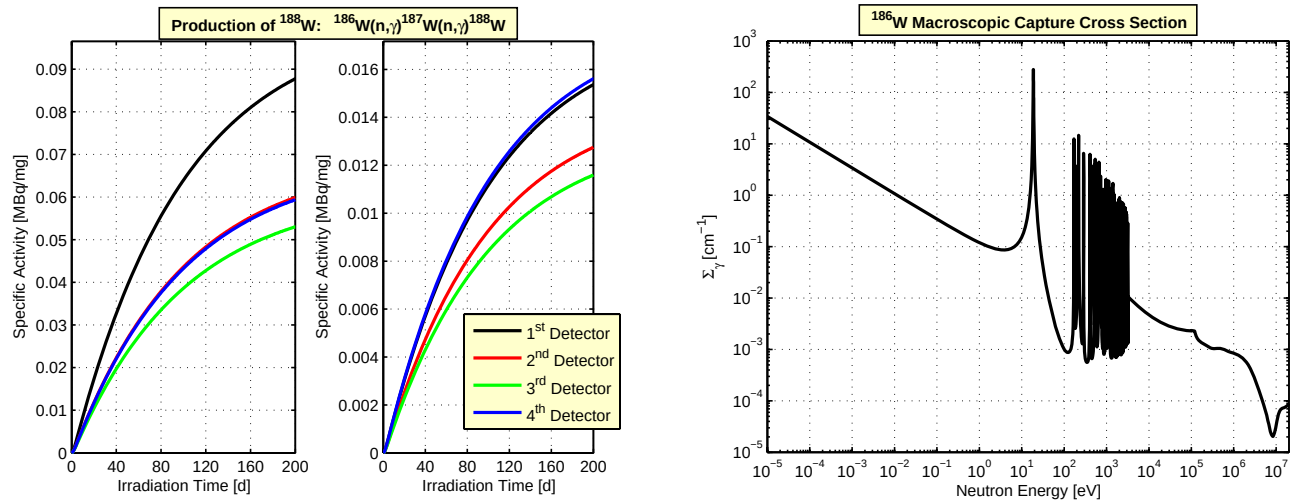

Figure 102. ^{188}W activity as a function of the irradiation time without and with self shielding, left and right subplots, respectively; ^{187}W macroscopic capture cross section; ^{186}W represents 28.6% of the parent material

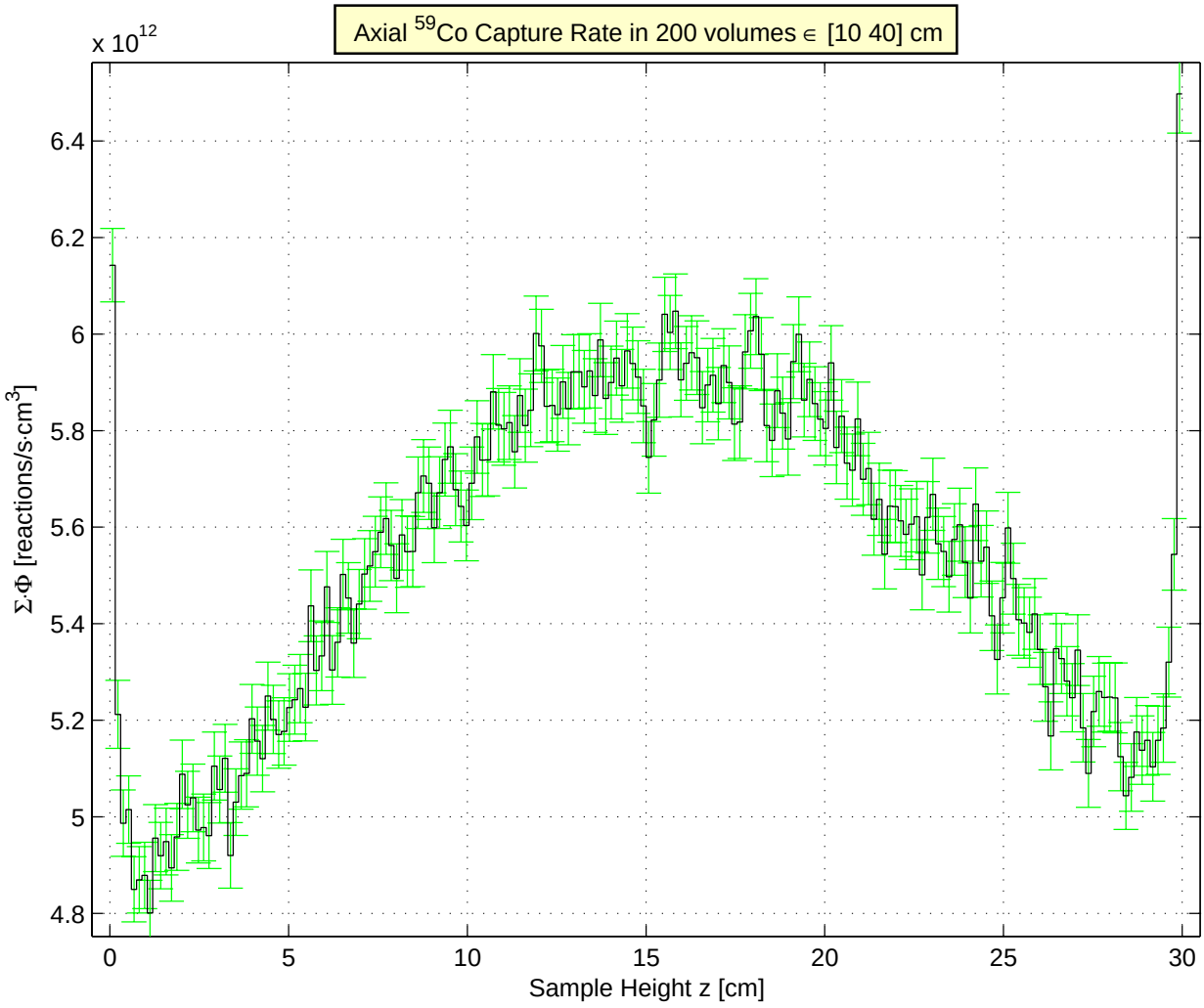

Figure 103. ^{59}Co capture rate as function of the sample height

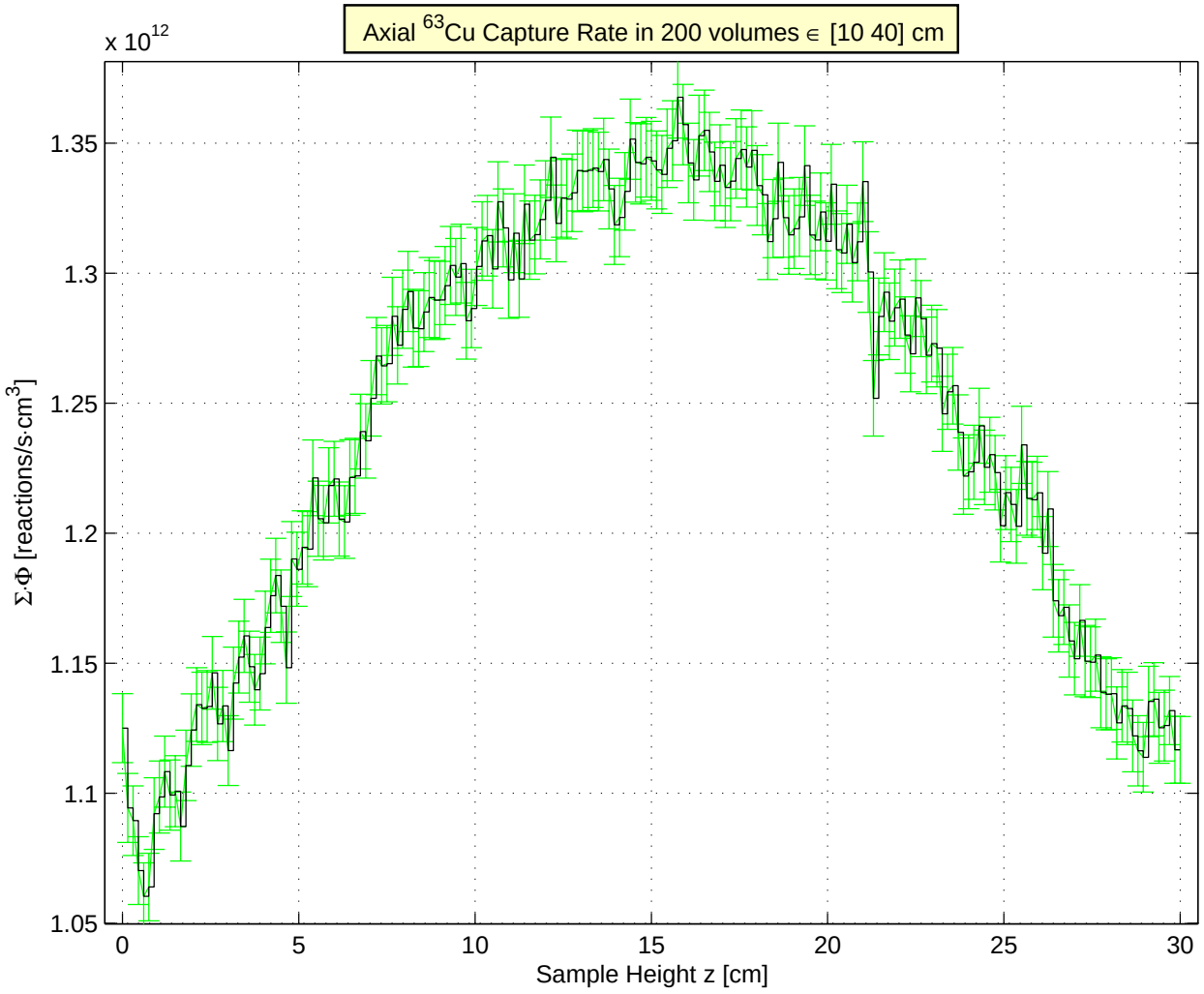

Figure 104. ^{63}Cu capture rate as a function of the sample height

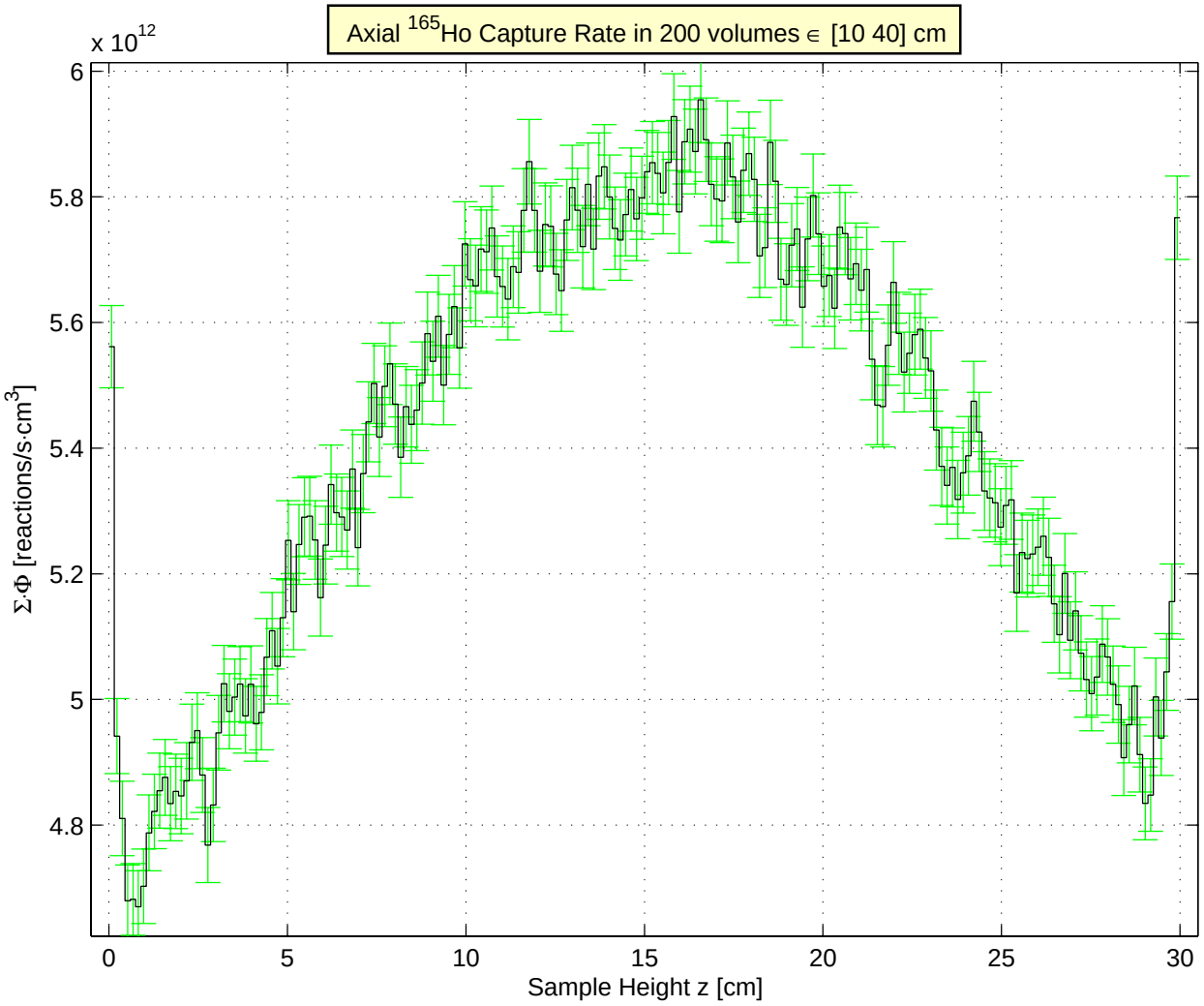

Figure 105. ^{165}Ho capture rate as a function of the sample height

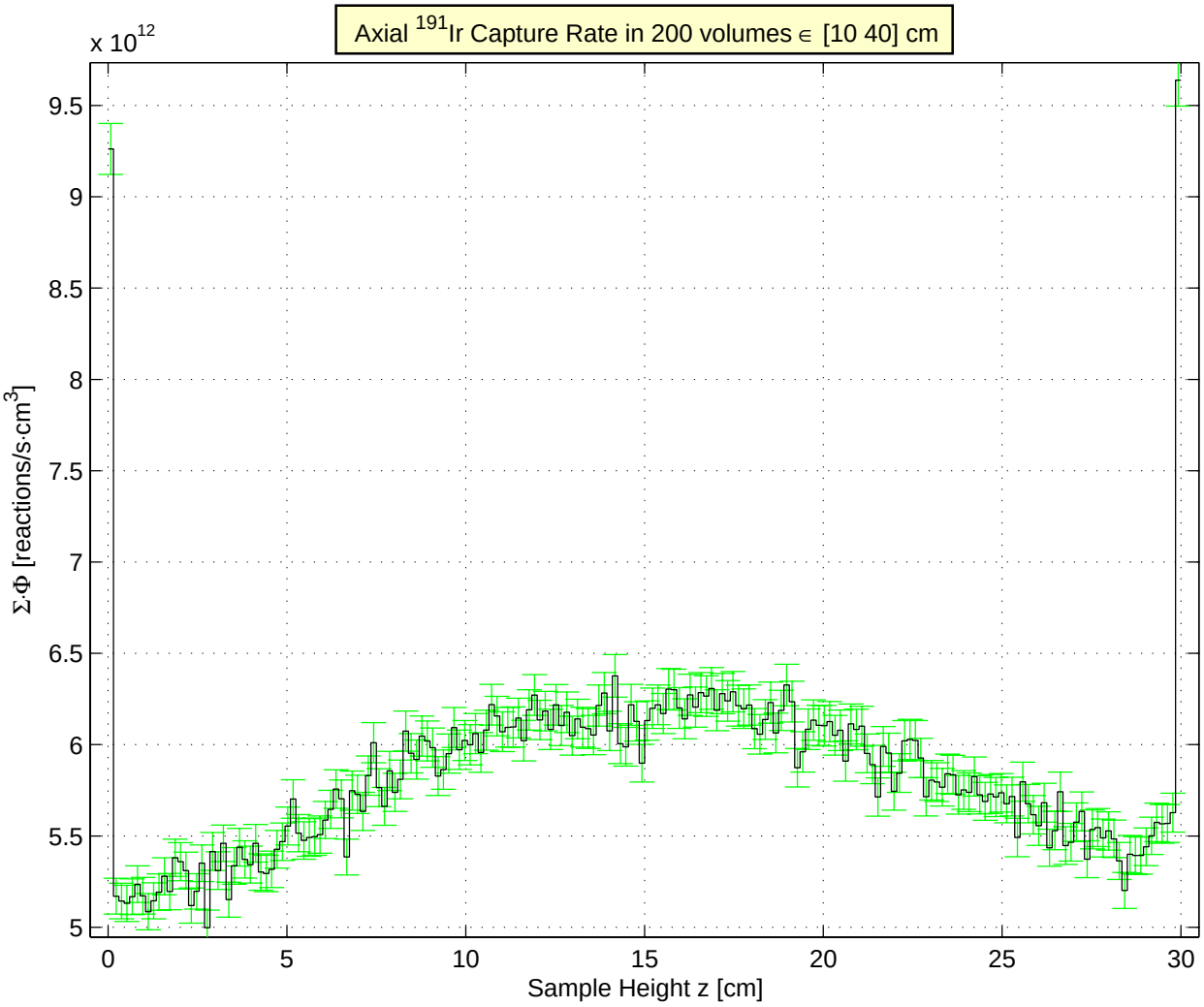

Figure 106. ^{191}Ir capture rate as a function of the sample height

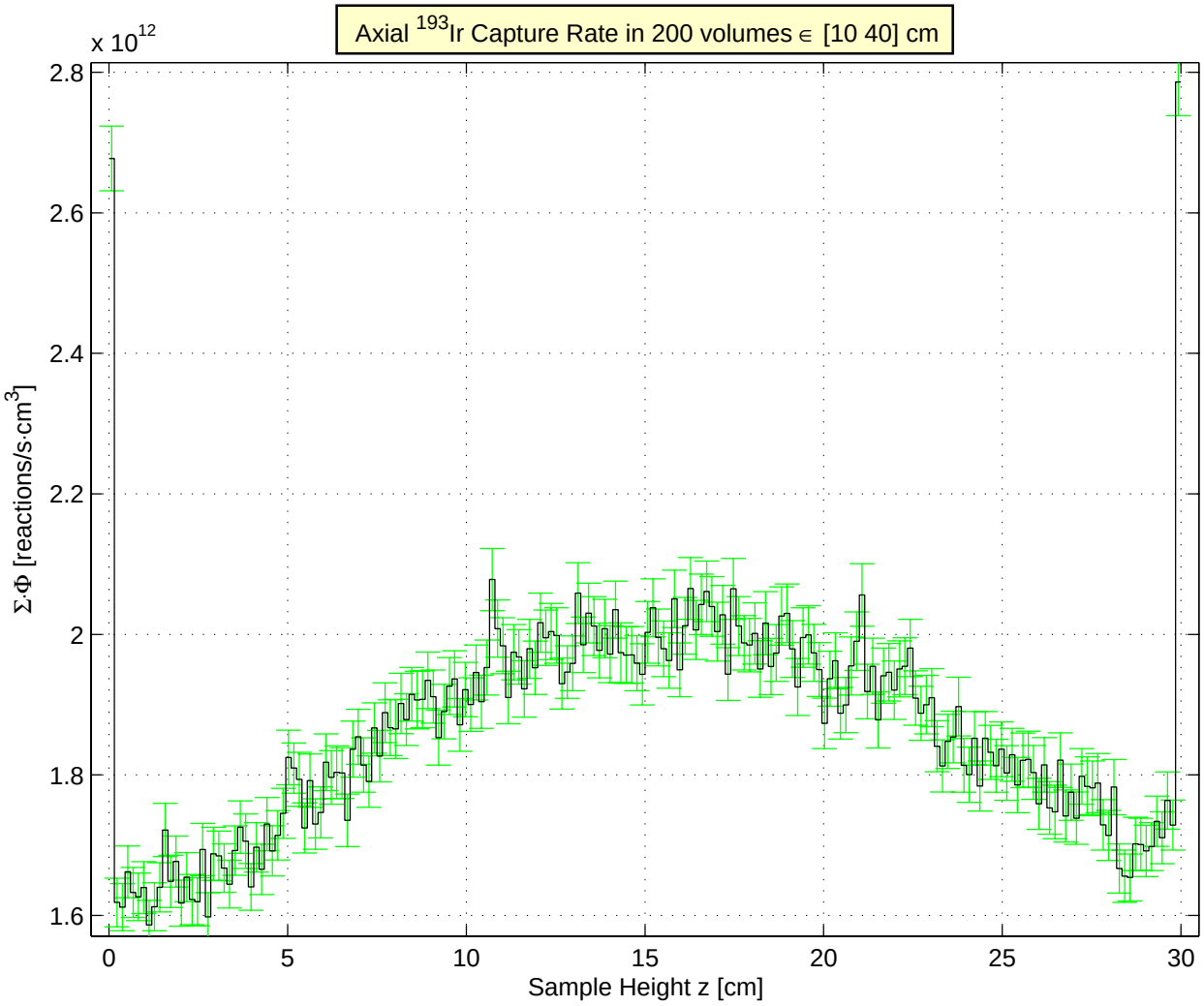

Figure 107. ^{193}Ir capture rate as a function of the sample height

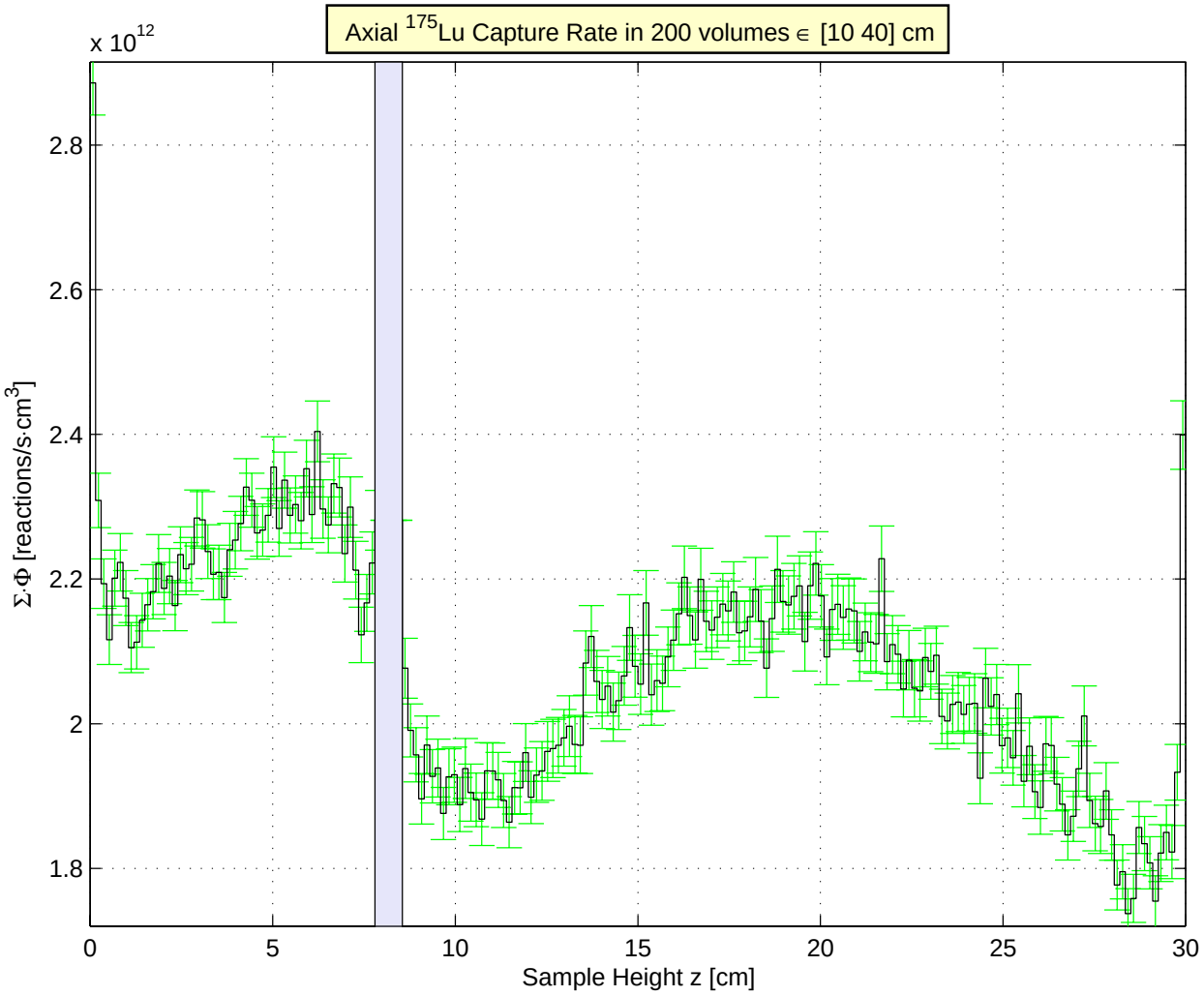

Figure 108. ^{175}Lu capture rate as a function of the sample height

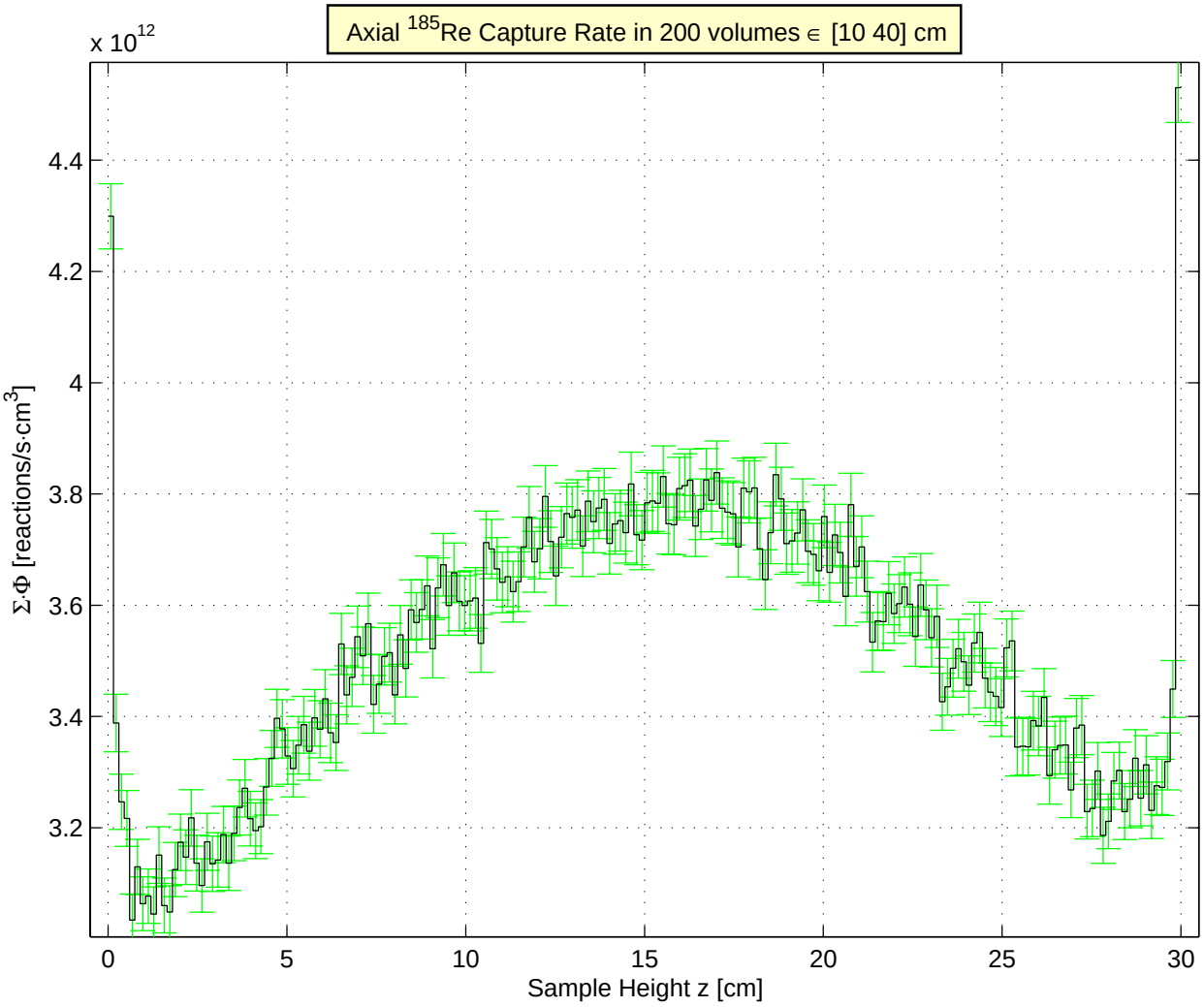

Figure 109. ^{185}Re capture rate as a function of the sample height

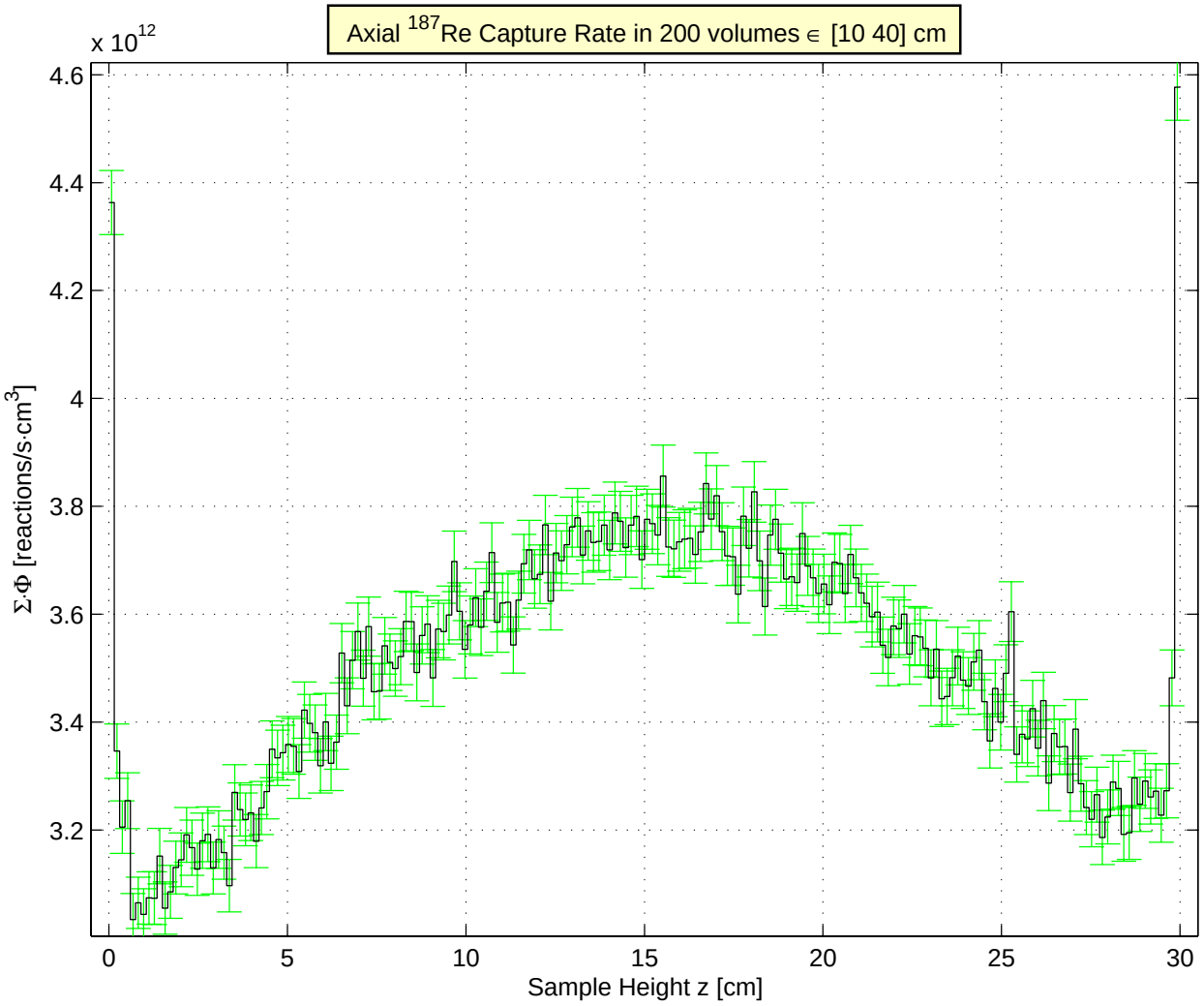

Figure 110. ^{187}Re capture rate as a function of the sample height

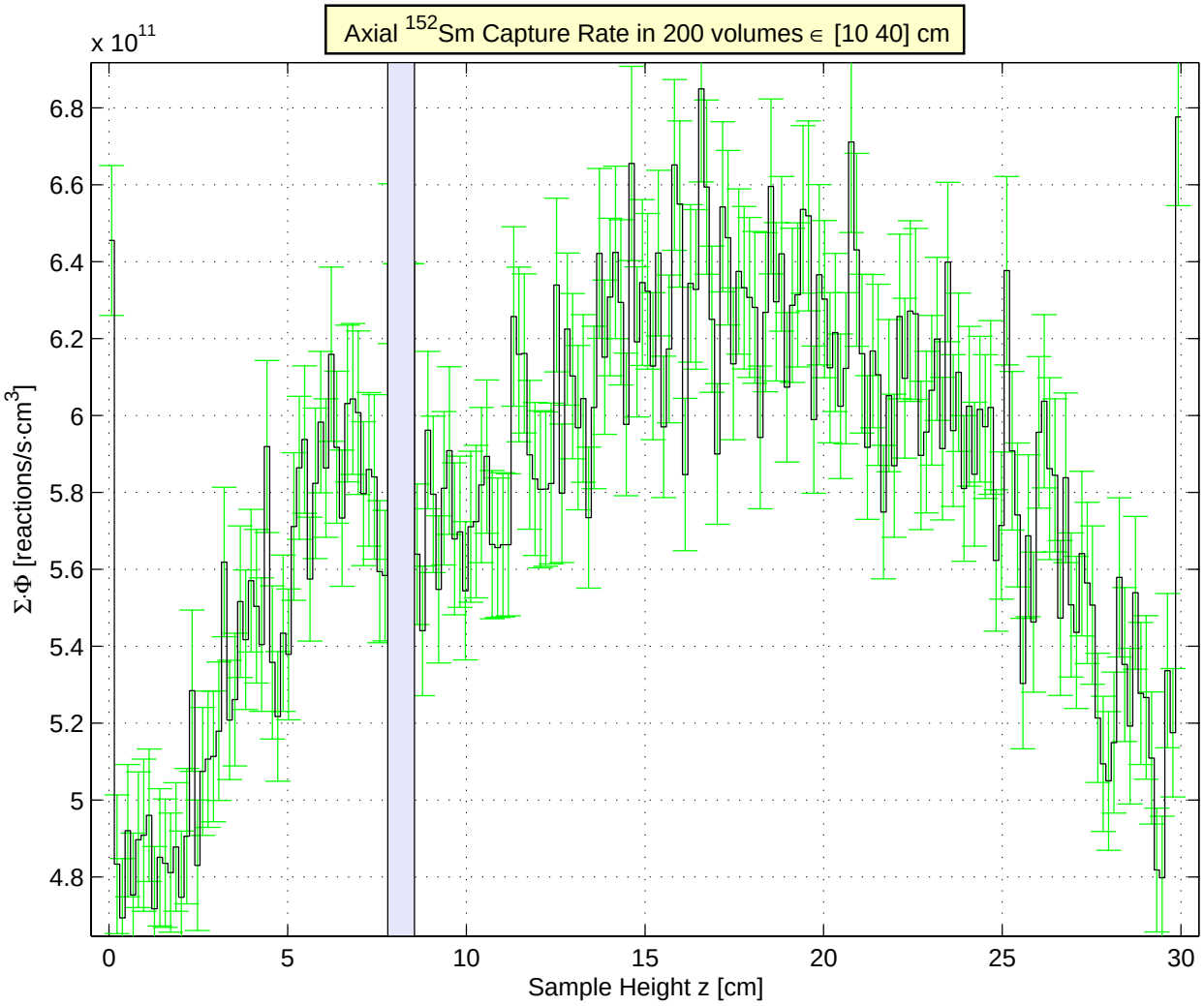

Figure 111. ^{152}Sm capture rate as a function of the sample height

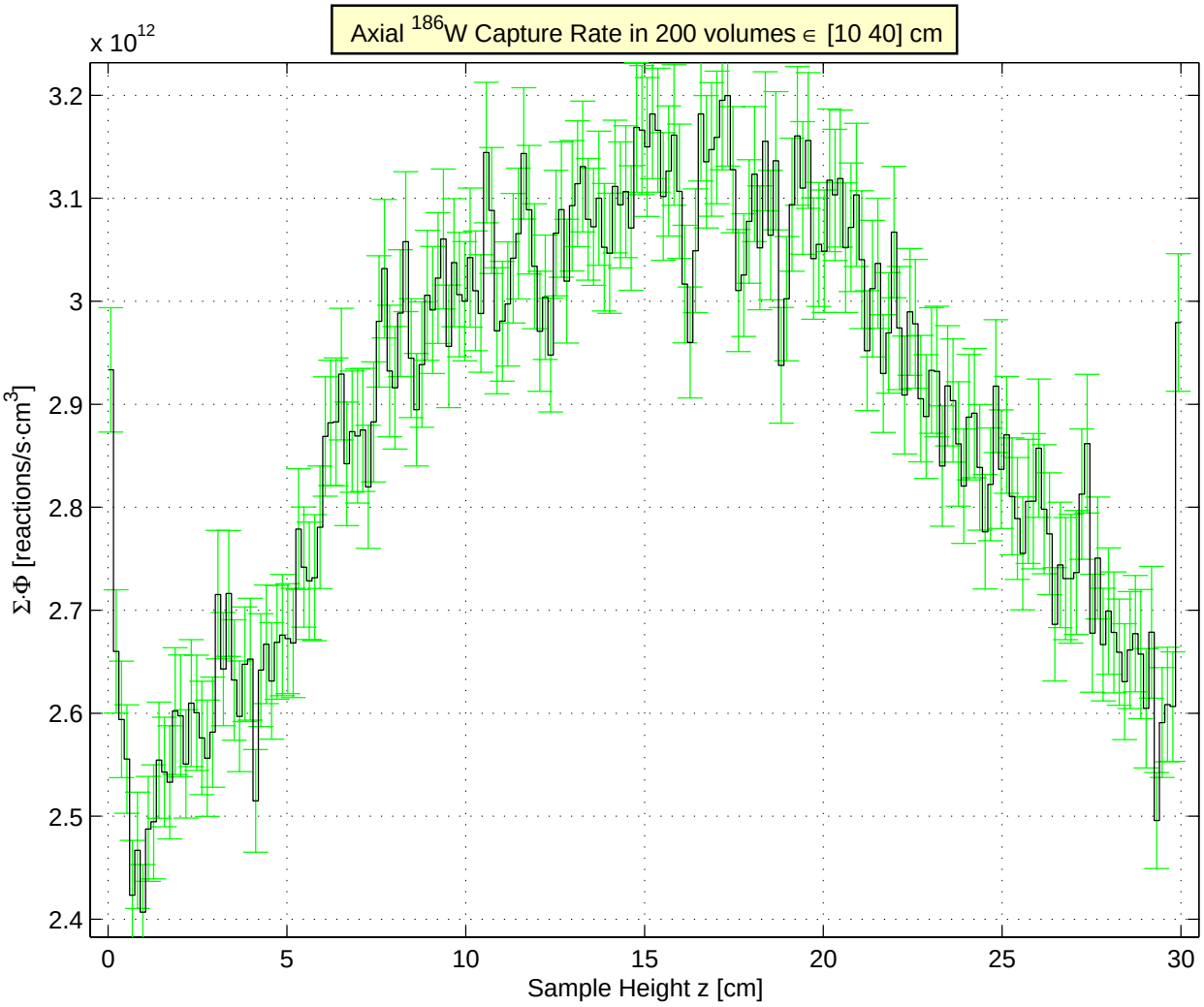

Figure 112. ^{186}W capture rate as a function of the sample height

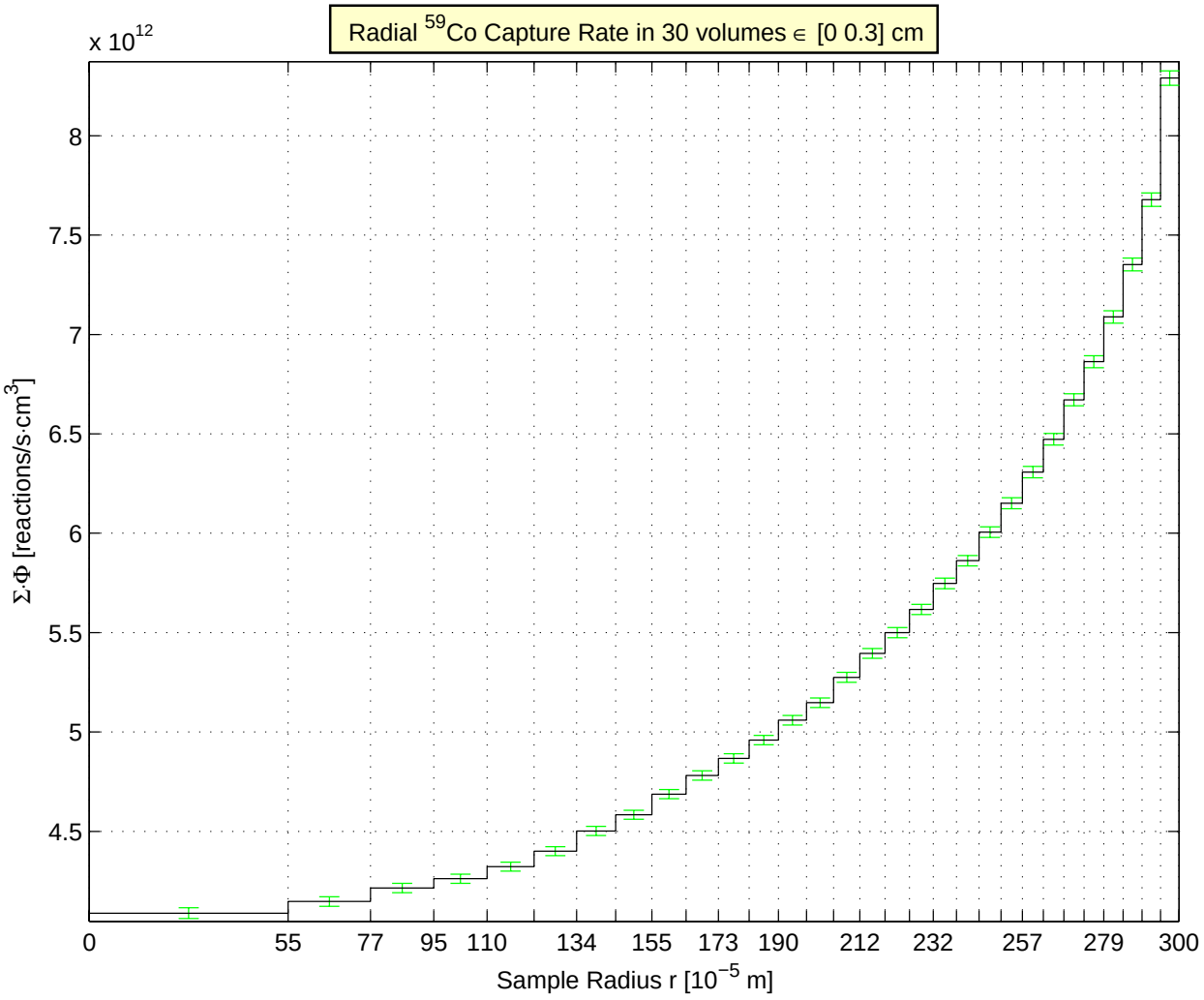

Figure 113. ^{59}Co capture rate as a function of the sample radius

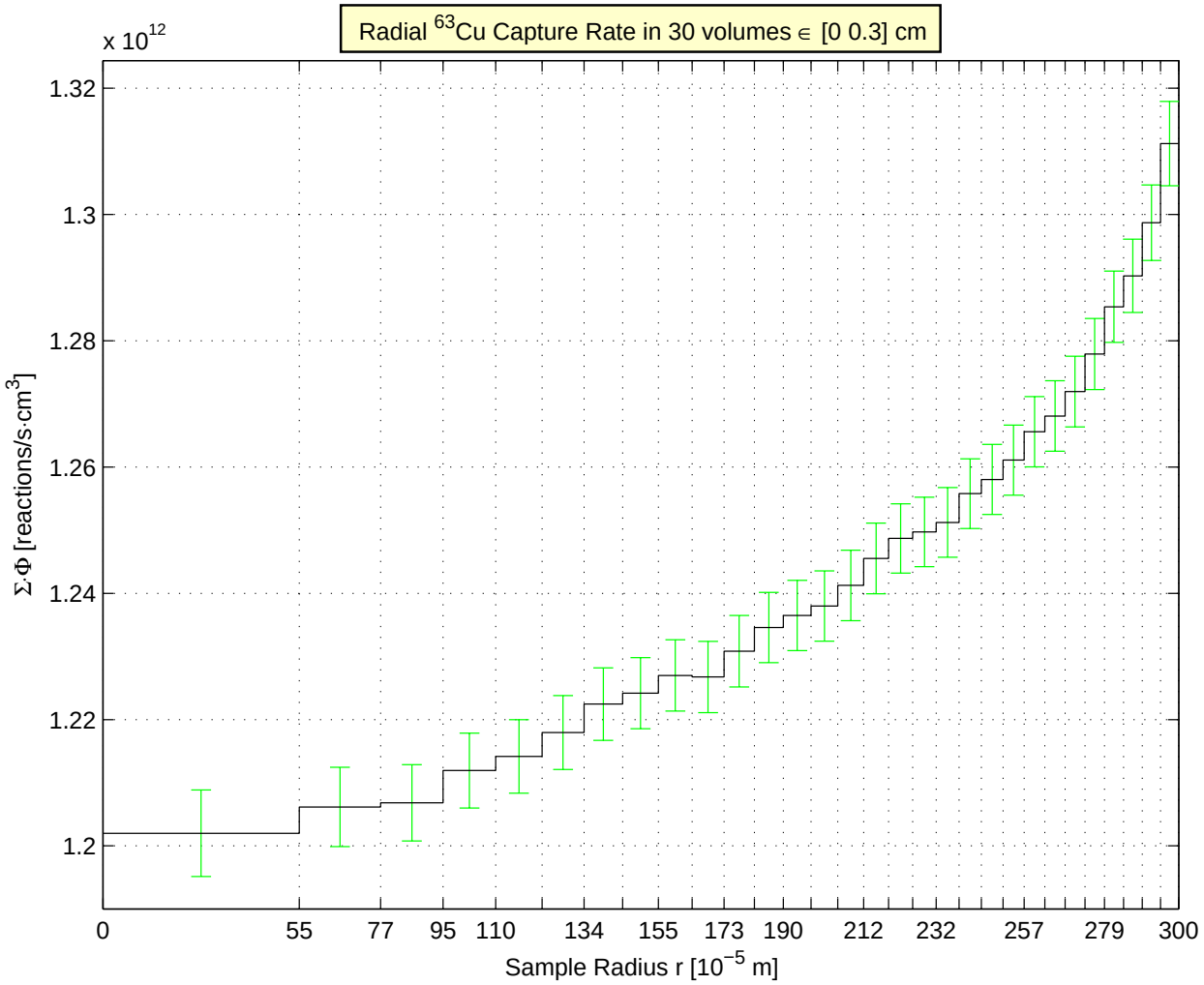

Figure 114. ^{63}Cu capture rate as a function of the sample radius

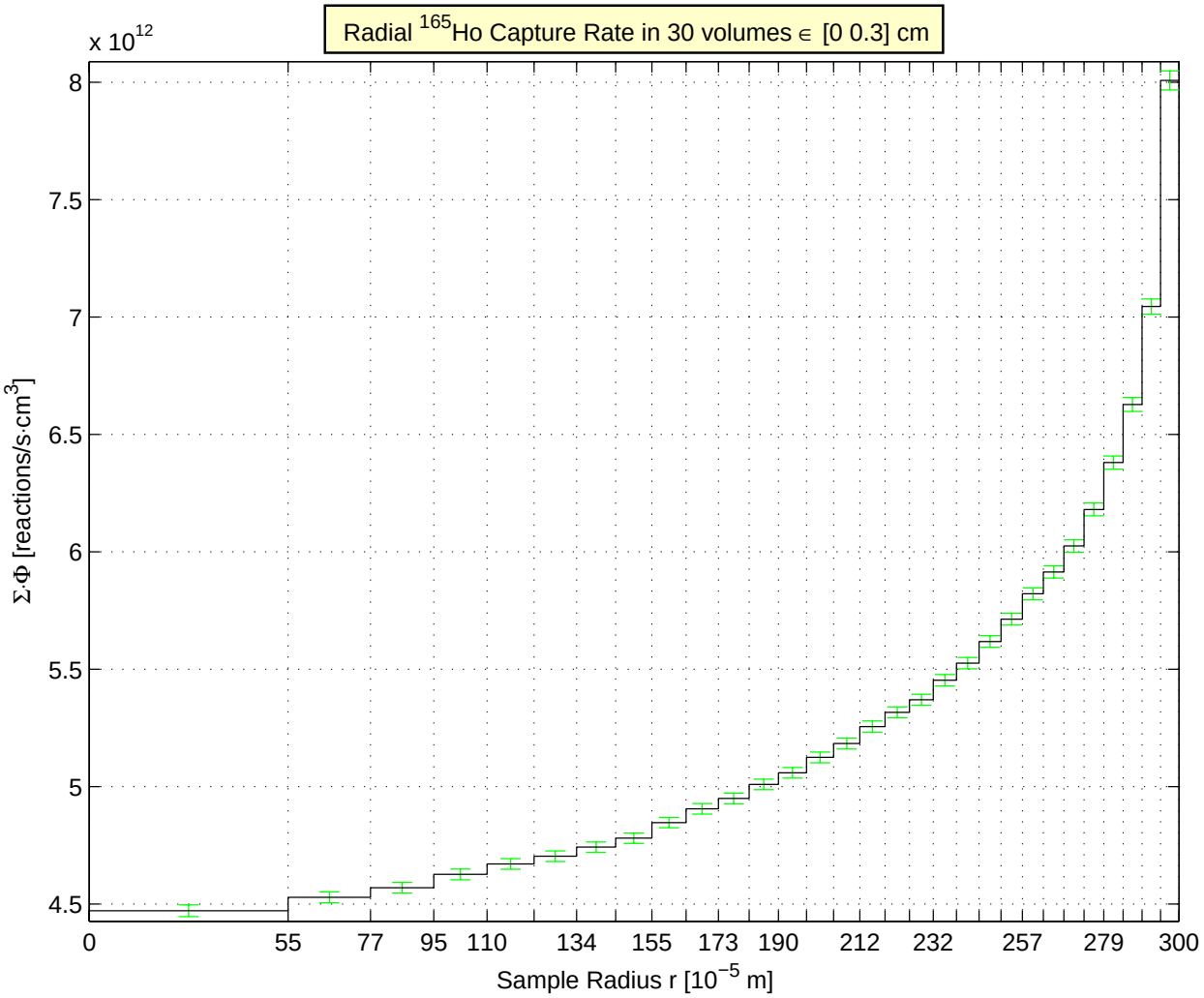

Figure 115. ^{165}Ho capture rate as a function of the sample radius

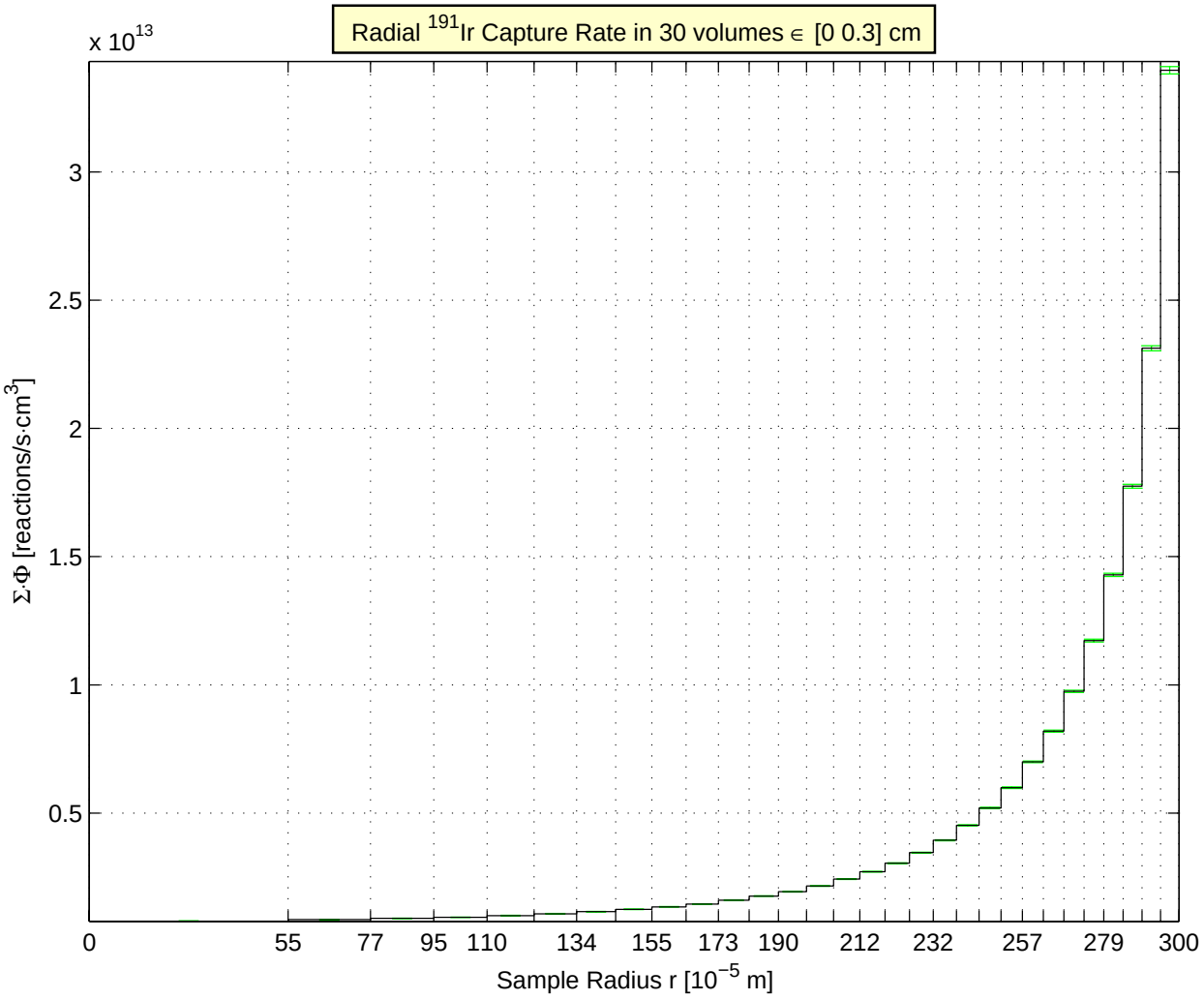

Figure 116. ^{191}Ir capture rate as a function of the sample radius

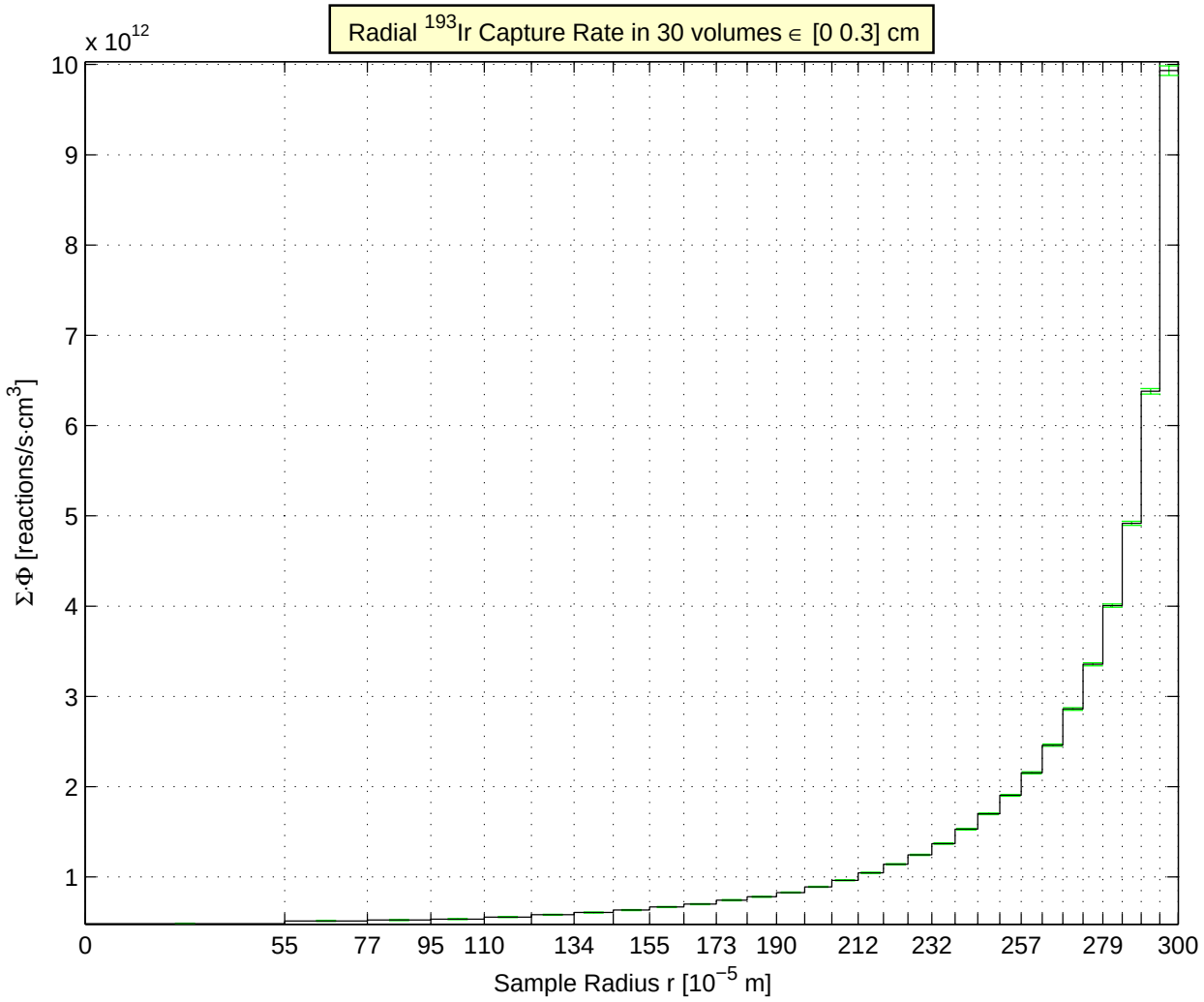

Figure 117. ^{193}Ir capture rate as a function of the sample radius

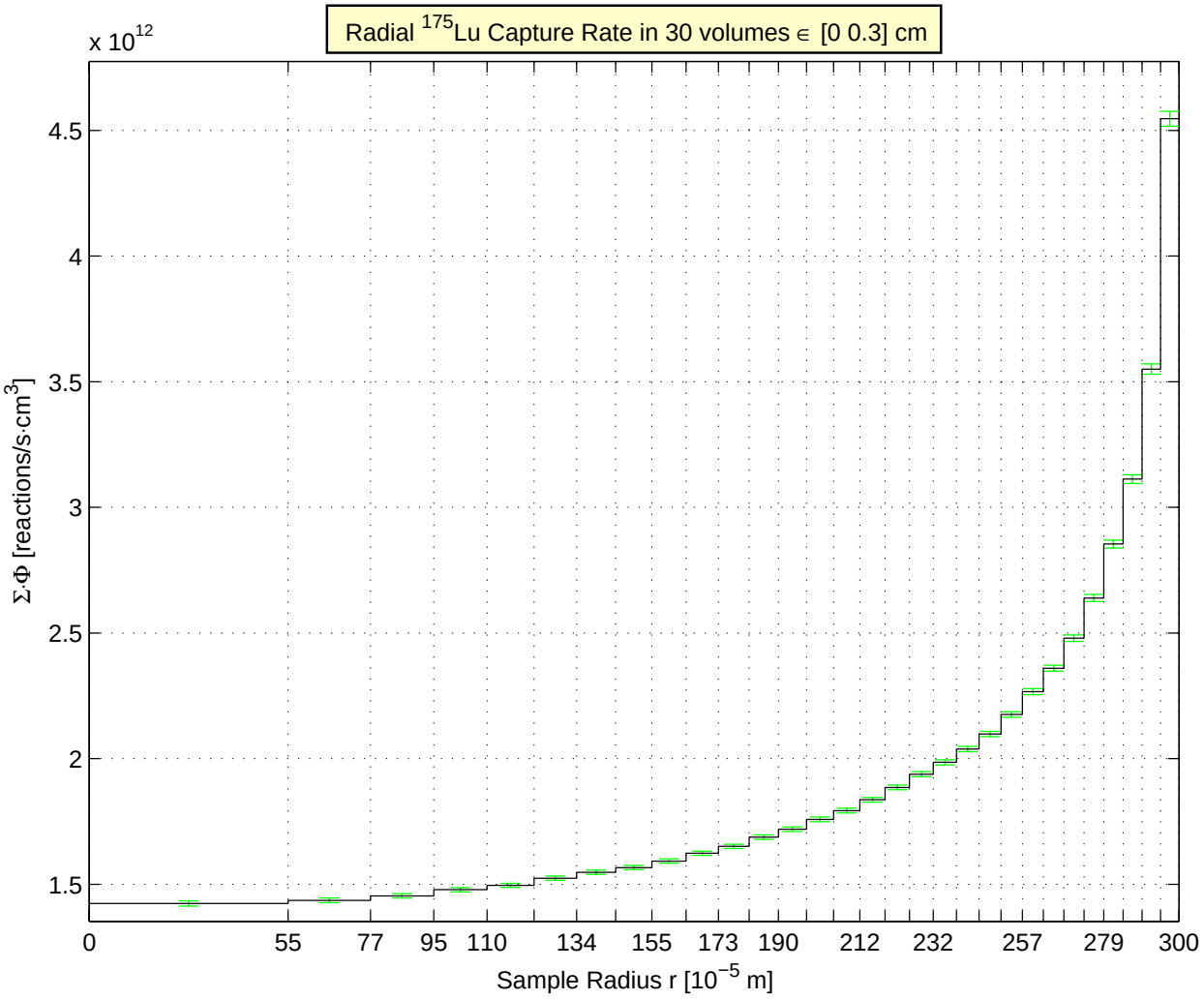

Figure 118. ^{175}Lu capture rate as a function of the sample radius

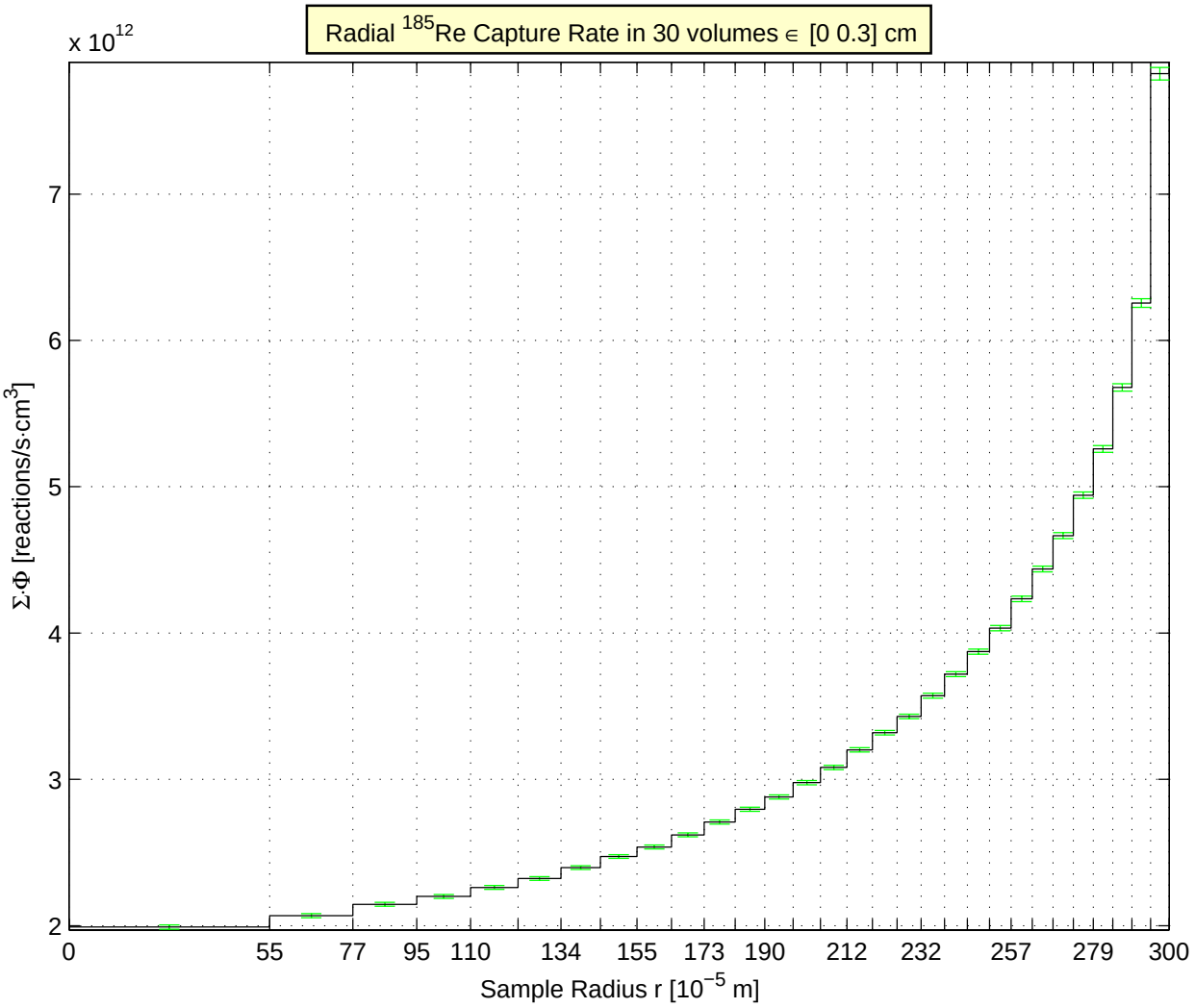

Figure 119. ^{185}Re capture rate as a function of the sample radius

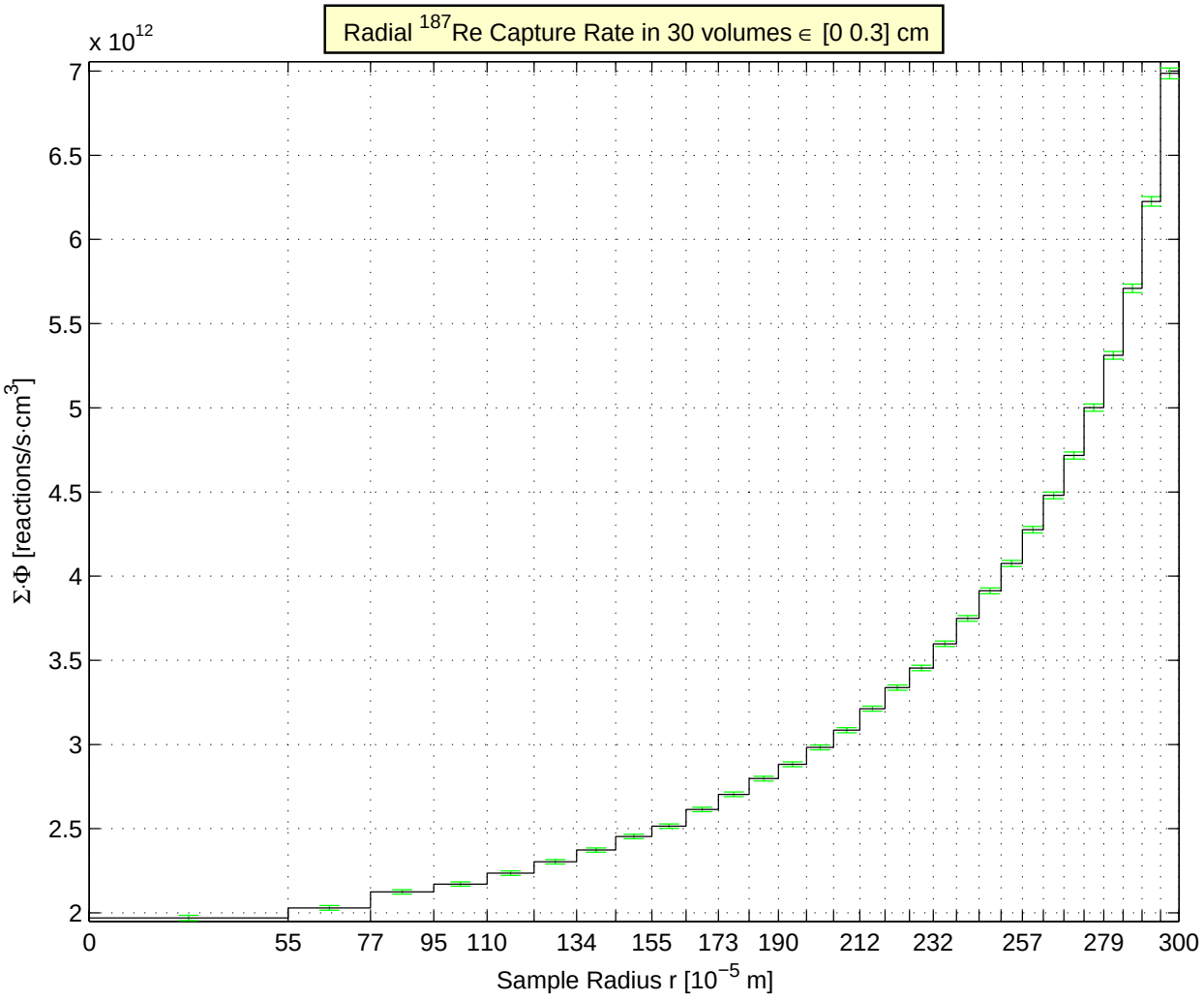

Figure 120. ^{187}Re capture rate as a function of the sample radius

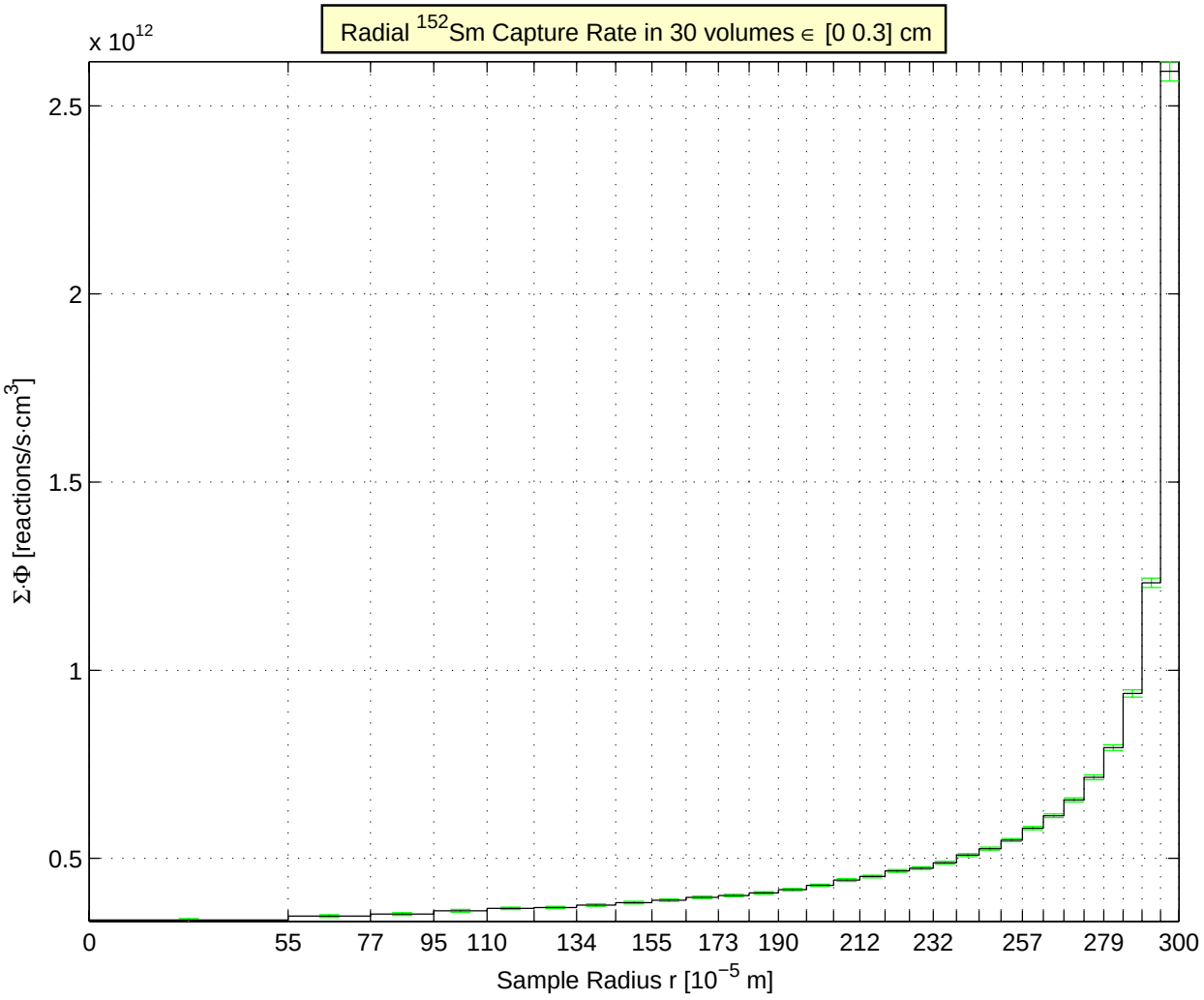

Figure 121. ^{152}Sm capture rate as a function of the sample radius

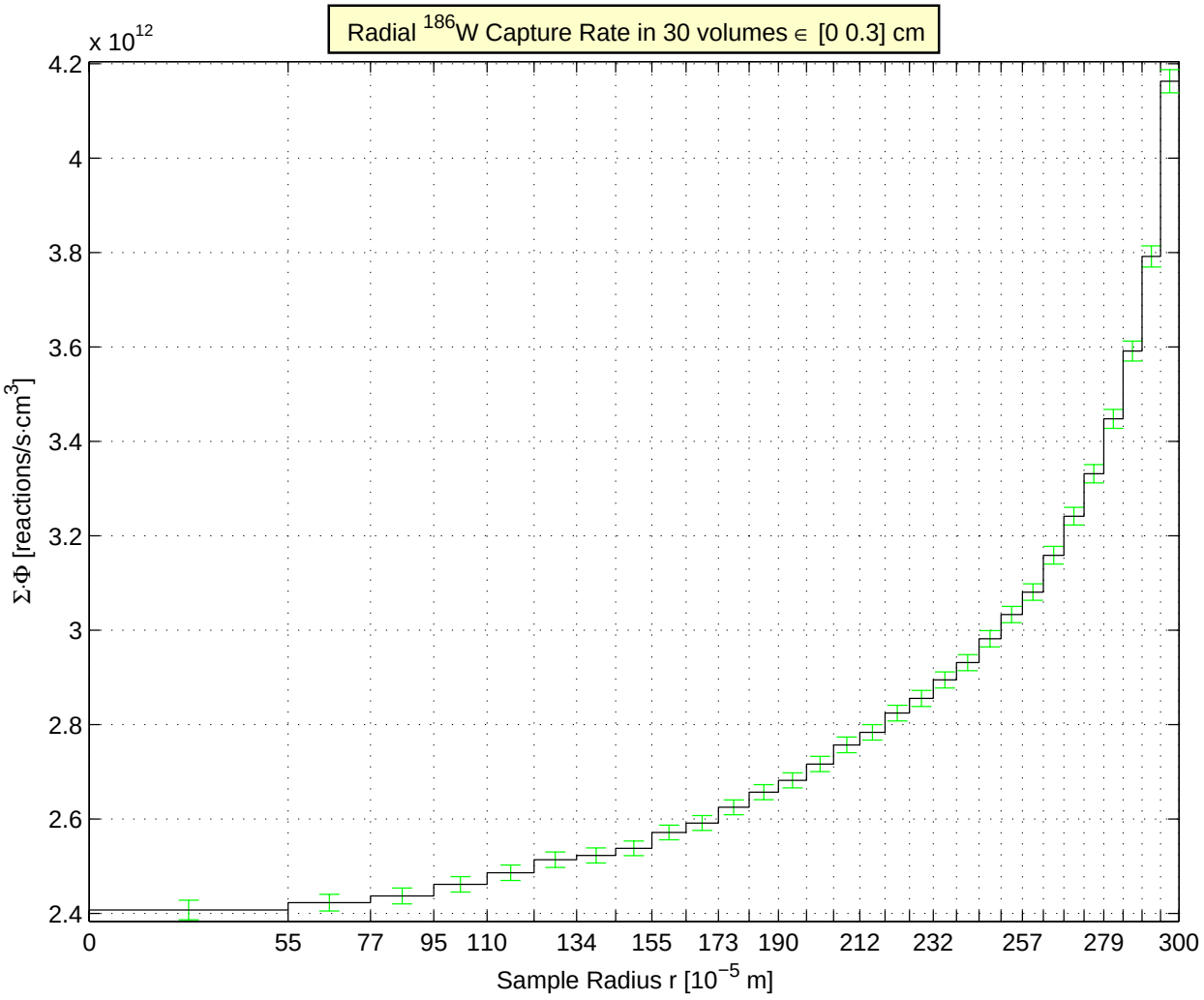

Figure 122. ^{186}W capture rate as a function of the sample radius

Nuclear Engineering Division
Argonne National Laboratory
9700 South Cass Avenue, Bldg. 208
Argonne, IL 60439-4842

www.anl.gov

UChicago ▶ Argonne LLC

A U.S. Department of Energy laboratory
managed by UChicago Argonne, LLC